

Aalto University  
School of Science  
Degree Programme in Engineering Physics

Ilari Rissanen

# Viscoelasticity and contact aging in a minimalistic friction model

Master's Thesis  
Espoo, May 26, 2015

Supervisor: Prof. Mikko Alava  
Advisor: D.Sc. (Tech.) Lasse Laurson

<b>Author:</b>	Ilari Rissanen	
<b>Title:</b>	Viscoelasticity and contact aging in a minimalistic friction model	
<b>Date:</b>	May 26, 2015	<b>Pages:</b> 111
<b>Major:</b>	Engineering physics	<b>Code:</b> F3005
<b>Supervisor:</b>	Prof. Mikko Alava	
<b>Advisor:</b>	D.Sc. (Tech.) Lasse Laurson	
<p>Dry friction (friction between solid surfaces in the absence of lubrication) is a complex phenomenon, involving effects from multiple time and length scales. The interplay of these effects in turn gives rise to interesting dynamical behaviour depending on the surface materials and various other parameters, such as the relative velocity of the surfaces.</p> <p>One of the intriguing properties of dry friction in the low-velocity regime is the emergence of so-called "stick-slip" motion. The name "stick-slip" originates from the observed jerky movement of rigid bodies on rough surfaces. This kind of motion has been linked with wear, and thus has been the subject of considerable scientific attention, especially in the field of nanotribology. However, factors related to stick-slip are plentiful, and many aspects still lack comprehensive explanation.</p> <p>Stick-slip motion is often characterized by power law distributed quantities. The critical exponents of these distributions divide stick-slip dynamics into different universality classes, meaning that systems with seemingly little in common can exhibit similar fundamental dynamics.</p> <p>In this thesis, a numerical simulation was conducted to investigate the properties of the stick-slip motion of a 1D elastic chain on a disordered substrate in the presence of viscoelastic effects and contact aging. The characteristic distributions and the critical exponents were determined from the avalanche statistics and compared to the experimental and computational values from existing research papers. Additionally, the onset of motion and the phenomena related to it were studied.</p> <p>It was observed that extending the model with viscoelasticity and contact aging both have both qualitative and quantitative consequences, introducing new kinds of avalanches and altering the critical exponents of the avalanche distributions. However, the results obtained with the extended model still differ from those found in laboratory experiments on dry friction. Possibilities for future improvements of the model are discussed at the end of this thesis.</p>		
<b>Keywords:</b>	friction, nanotribology, stick-slip phenomenon, numerical simulation, viscoelasticity, contact aging	
<b>Language:</b>	English	

<b>Tekijä:</b>	Ilari Rissanen		
<b>Työn nimi:</b>	Viskoelastisuus ja kontaktin ikääntyminen yksinkertaistetussa kitkamallissa		
<b>Päiväys:</b>	26. toukokuuta, 2015	<b>Sivumäärä:</b>	111
<b>Pääaine:</b>	Teknillinen fysiikka	<b>Koodi:</b>	F3005
<b>Valvoja:</b>	Prof. Mikko Alava		
<b>Ohjaaja:</b>	TkT Lasse Laurson		
<p>Voitelemattomien pintojen välinen kitka (kuiva kitka) on monimutkainen ilmiö, johon usean aika- ja pituuskaalan tapahtumat vaikuttavat. Näiden tapahtumien vuorovaikutus puolestaan saa aikaan dynamiikkaa, joka riippuu pintojen materiaaleista ja useista muista parametreista, kuten pintojen suhteellisesta nopeudesta toisiinsa nähden.</p> <p>Yksi kuivan kitkan mielenkiintoisista ominaisuuksista on niin sanotun ”stick-slip”-liikkeen syntyminen alhaisilla nopeuksilla. Stick-slip -liikkeen nimi juontaa juurensa kokeista, joissa jäykän kappaleen havaittiin liikkuvan nykivästi karhealla pinnalla. Tällainen liike on yhdistetty pintojen kulumiseen ja siksi sitä on tutkittu huomattavasti etenkin nanotribologiassa. Tästä huolimatta kaikkia stick-slip -liikkeeseen liittyvistä lukuisista ilmiöistä ei ole vielä kyetty täydellisesti selittämään.</p> <p>Yleinen Stick-slip -liikkeelle tunnusomainen piirre on potenssilakien mukaan jakautuneet suureet. Näiden potenssilakien kriittiset eksponentit jakavat stick-slip liikkeen erilaisiin universaalisuusluokkiin: systeemeihin, jotka voivat olla näennäisesti suurista eroista riippumatta fundamentaaliselältä dynamiikaltaan samanlaisia.</p> <p>Tässä työssä tutkittiin numeerisen simulaation avulla yksiulotteisen elastisen ketjun stick-slip liikettä epäjärjestyneen substraatin päällä, sekä kahden ilmiön, viskoelastisuuden ja kontaktin vanhenemisen, vaikutusta ko. liikkeeseen. Stick-slip-ilmiön kannalta keskeiset jakaumat ja niiden kriittiset eksponentit määritettiin vyörystatistiikasta ja niitä verrattiin olemassaoleviin kokeellisiin ja laskennallisiin arvoihin. Lisäksi tutkittiin liikkeen alkua ja siihen liittyviä ilmiöitä.</p> <p>Työssä havaittiin viskoelastisuuden ja kontaktin vanhenemisen muuttavan elastisen ketjun liikettä sekä kvantitatiivisesti että kvalitatiivisesti: uudentyypisiä vyöryjä havaittiin, ja vyöryjakaumien eksponentit muuttuivat. Muutoksista huolimatta simulaatioista saadut tulokset eroavat laboratoriokeiden tuloksista. Parannusehdotuksia malliin esitetään työn lopussa.</p>			
<b>Asiasanat:</b>	kitka, nanotribologia, stick-slip-ilmiö, numeerinen simulaatio, viskoelastisuus, kontaktin ikääntyminen		
<b>Kieli:</b>	englanti		

# Acknowledgements

Though a milestone in one's studies, a master's thesis is hardly an achievement of a single person. I owe a debt of gratitude to many people who have in one way or another helped me to get to where I am now. However, brevity is the soul of wit, so I'll be brief.

The greatest thanks go to my instructor, Lasse Laurson, for both excellent advice and having outstanding patience for my sometimes slow progress with the work. Writing was not always easy, going through revision after revision and coming up with constructive comments must have been even less so.

The simulations in this thesis required considerable amount of computing power. Thus I'd like to acknowledge the Triton computation cluster and the IT-personnel maintaining it. Without them, the time I spent working on this project would have to be measured in years instead of months.

For making these five years in (and out of) the university enjoyable, I'm grateful to my friends, especially the guys at `#e_e`. Let's keep goofing around.

Finally, I'd like to thank my family for their moral (and economic) support. It might have been due to my parents' encouragement that I chose this line of study. That, or perhaps the interest in natural sciences is hereditary. Either way, I haven't regretted the decision.

Espoo, May 26, 2015

Ilari Rissanen



# Contents

<b>Introduction</b>	<b>1</b>
<b>1 Experimental background</b>	<b>5</b>
1.1 Stick-slip motion studies . . . . .	6
1.2 Investigating the onset of motion . . . . .	8
<b>2 Minimalistic models for dry friction</b>	<b>10</b>
2.1 Tomlinson model . . . . .	11
2.2 Frenkel-Kontorova model . . . . .	12
2.3 Frenkel-Kontorova-Tomlinson model . . . . .	13
<b>3 Avalanche statistics</b>	<b>16</b>
3.1 Correlation length, interface roughness and avalanche distributions . . . . .	16
3.2 Scaling relations . . . . .	21
<b>4 Implementation of the FKT model</b>	<b>23</b>
4.1 Simulation basics . . . . .	23
4.2 The timescale issue . . . . .	25
4.3 Control parameters . . . . .	27
<b>5 Augmenting the FKT model</b>	<b>28</b>
5.1 Viscoelasticity . . . . .	28
5.2 Contact aging . . . . .	30
<b>6 Results</b>	<b>32</b>
6.1 The vanilla FKT model with a perpendicularly driven chain . . . . .	33
6.1.1 Onset of motion . . . . .	33
6.1.2 Avalanche statistics . . . . .	35
6.2 The vanilla model with parallel driving . . . . .	41

6.2.1	Kinks and the particle equilibrium distance . . . . .	43
6.2.2	Precursory avalanches . . . . .	47
6.2.3	Avalanche statistics . . . . .	48
6.3	Viscoelasticity . . . . .	55
6.3.1	Perpendicular chain: onset of motion . . . . .	55
6.3.2	Perpendicular chain: avalanche statistics . . . . .	57
6.3.3	Parallel chain: onset of motion . . . . .	60
6.3.4	Parallel chain: avalanche statistics . . . . .	61
6.4	Contact aging . . . . .	66
6.4.1	Perpendicular chain: onset of motion . . . . .	66
6.4.2	Perpendicular chain: avalanche statistics . . . . .	70
6.4.3	Parallel chain: onset of motion . . . . .	73
6.4.4	Parallel chain: avalanche statistics . . . . .	75
6.5	Simulations with both contact aging and viscoelasticity . . . . .	79
6.5.1	Perpendicular chain: onset of motion . . . . .	79
6.5.2	Perpendicular chain: avalanche statistics . . . . .	81
6.5.3	Parallel chain: onset of motion . . . . .	83
6.5.4	Parallel chain: avalanche statistics . . . . .	85
<b>7</b>	<b>Conclusions</b>	<b>89</b>
7.1	Future prospects . . . . .	92
<b>A</b>	<b>Driving and slip characterization</b>	<b>98</b>
<b>B</b>	<b>Finite-size effects</b>	<b>101</b>
B.0.1	Parallel driving . . . . .	102
B.0.2	Perpendicular driving . . . . .	109

# Introduction

There seems to be trend in physics that the more banal a phenomenon appears outward, the more complex its actual physical explanation. Such is also the case of probably the most mundane thing in existence: friction.

Friction is the force resisting motion between two bodies in contact. Being an omnipresent part of everyday life, it's usually not friction but its absence that is problematic, a fact any pedestrian walking on a frozen walkway can attest. In the modern times, however, attention has turned to the detrimental sides of friction: when it comes to machinery performing repetitive tasks (car engines, industrial robots etc.), friction causes heating and wear, degrading moving components and eventually leading to breaking down of said machinery. In 2000, it was estimated that in Germany alone the economic losses due to friction were between 30 and 40 billion euro [1]. Worldwide, the losses are likely to be immense. Hence it's no surprise that friction (and especially how mitigate or eliminate it) has been the subject of intense research since industrialization. In fact, friction has spawned an entire branch of science, tribology, around it.

Friction is often categorized according to the types of surfaces in contact. The category considered in this thesis is friction between two solid surfaces in the absence of lubrication, commonly referred to as *dry friction*.

The earliest attempts to find out the characteristics of dry friction were made by Guillaume Amontons and Charles-Augustin de Coulomb, who discovered the so-called phenomenological laws of friction: that the friction force is directly proportional to the applied load (Amontons' 1st law), that the force is independent of the area of contact (Amontons' 2nd law) and that kinetic friction is independent of sliding velocity (Coulomb's law). The most universally known friction model (Coulomb model), characterized by constant *static friction coefficient*  $\mu_s$  and *kinetic friction coefficient*  $\mu_k$ , is based on these laws. In the macroscopic level, this simple model is often good enough depiction of friction. Nonetheless, modern studies reaching down to nanometer length scales have revealed that the Coulomb model is severely lacking. Violations of the phenomenological laws have been demonstrated in

experiments (e.g. [2, 3]), and some counterintuitive results have been uncovered, such as the existence of negative coefficient of friction (friction decreases with larger normal load) [4].

It's evident that better explanation for dry friction is required. However, despite numerous experimental, computational and theoretical studies, dry friction has eluded a comprehensive description so far. One major difficulty in constructing a complete theory is that a multitude of factors in various time and length scales (schematically illustrated in Fig. 1) contribute to the total friction force. The current consensus seems to be that dry friction is intimately linked with adhesion between surfaces [5–7], a phenomenon which itself can extend from nanometer and -second scale [8] up to micrometers and hours [9].

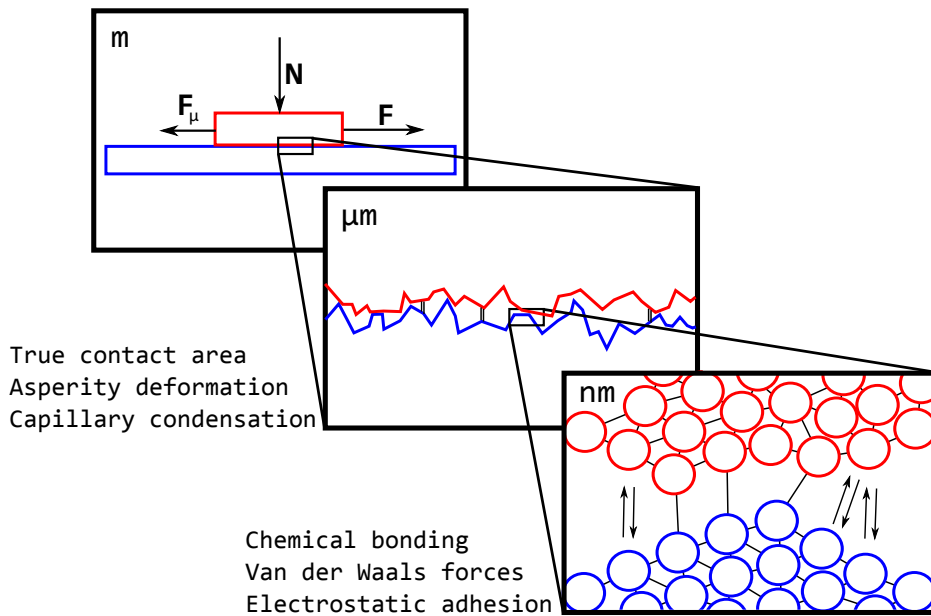


Figure 1: Even the classic "Pulling a block on a table" experiment becomes highly nontrivial when all relevant effects are considered (just a couple of them named in the picture).

A phenomenon found ubiquitous in many length scales of dry friction is so-called *stick-slip motion*: movement characterized by abrupt slips between long periods of stillness. In general, the term *stick-slip* refers to dynamics exhibiting a non-equilibrium phase transition between two states: the *pinned* state (stick) and the *unpinned* state (slip). In the pinned state, a system is stationary with respect to time due to some *pinning potential*, but can accumulate energy via external influences. When unpinned, the system rapidly

releases the accumulated energy, relaxing to another pinned state or slipping indefinitely (if the pinning potential vanishes or enough energy is constantly supplied to the system). These sudden relaxations are called *avalanches*, and the transition from pinned to unpinned state is named the *depinning transition*.

A system near the depinning transition displays qualities similar to other *critical phenomena* (such as second order thermodynamic phase transitions): various observables become power law distributed, depending only on the distance from criticality and a *critical exponent* corresponding to the observable in question. This kind of critical behaviour is interesting since stick-slip is not necessarily limited to friction; other phenomena following similar dynamics include earthquakes [10], Barkhausen noise in ferromagnetic substances [11] and crack propagation in brittle materials [12], to name a few examples. It would seem then that these processes might have in some way similar origins, and hence considerable effort has been made to uncover the underlying principles of general stick-slip motion.

Frictional stick-slip motion is encountered nearly everywhere, in both microscopic and macroscopic forms. The creaking of door hinges and the sound of a violin are caused by the microscopic stick-slip motion of the materials in contact [5]. A macroscopic example can be found by imagining a body being dragged along a surface by a spring pulled with a slow constant velocity. The movement alternates between stationary and sliding states causing visible stick-slip behaviour: the body is stationary (in the pinned state) until the pulling force exceeds some critical force (commonly called the *static friction force*), after which the body slips forward (an avalanche) and relaxes the force of the pulling spring. As the pulling force drops below the force required to keep the body in motion (the *dynamic friction force*), the body sticks in place until the force from the spring once again overcomes the static friction force. Depending on the parameters of the system and the environment (such as the average spacing of surface inhomogeneities), the stick-slip motion can be regular or chaotic [13].

This kind of macroscopic jerky movement is possible only when the dragging velocity and the spring constant of the pulling spring are sufficiently small; above certain (material dependent) velocity and spring constant, the macroscopic stick-slip behaviour ceases and the *smooth sliding* regime is achieved. This does not necessarily mean that sticking and slipping does not occur, since the microscopic relaxations of the asperities in contact and even the nano-level bond breaking and forming are types of stick-slip motion. However, these small-scale stick-slip events are asynchronous and they average out on larger timescales, leading to apparently steady motion [5]. An example of the time development of the friction force of a body (in this case,

a mica surface) pulled forward by a spring under different pulling velocities is shown in Fig. 2.

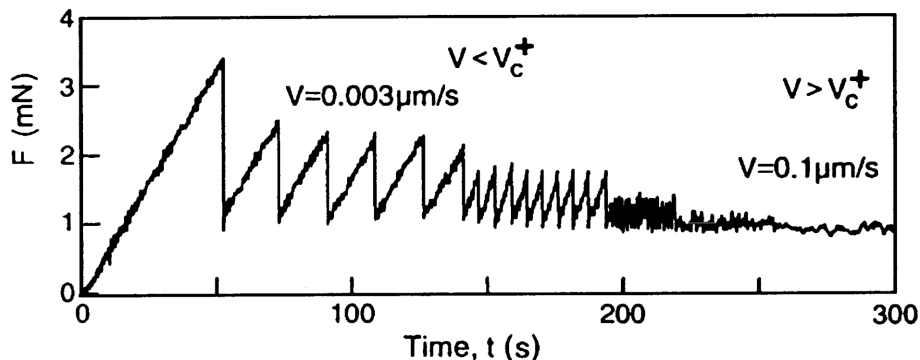


Figure 2: Friction force as a function of time in various dragging velocity regimes. Higher velocities tend to smooth out the stick-slip motion. In this experiment, the chaotic stick-slip motion regime appears near the smooth sliding regime. At small velocities, the motion is regular. [13]

Various models for simulating dry friction have been proposed over the years, ranging from phenomenological rate-and-state models to molecular dynamics simulations [14]. In this thesis, the stick-slip motion dynamics of a system incorporating two novel effects, *viscoelasticity* and *contact aging*, is studied with one of the so-called "minimalistic" models, the 1-dimensional Frenkel-Kontorova-Tomlinson (FKT) model. In the FKT model, a chain of particles is pulled by springs atop a potential surface representing a rigid substrate. This model was used because it's computationally (relatively) light and easy to implement, yet exhibits many phenomena found in dry friction. Additionally, extending the model with viscoelasticity and contact aging was straightforward.

The structure of the thesis is as follows. The first chapter discusses experiments that have been made to study dry friction and stick-slip motion in laboratory conditions. In the second chapter, the FKT model and its origins are presented. The third chapter introduces the quantities of interest that can be obtained from the model. In Chapters 4 and 5, the implementation of the model and the novel effects that were the primary subjects of examination of the work are presented, respectively. Chapter 6 deals with the numerical results obtained from the simulations and how they compare to values found in other literature. Finally, the conclusion of the study and possibilities for future research are discussed in Chapter 7. Observations not directly related to contact aging or viscoelasticity but nevertheless deemed interesting are included in Appendices A and B.

# Chapter 1

## Experimental background

Laboratory experiments have greatly advanced the knowledge of dry friction, especially in the twentieth century. Theoretical understanding has progressed from the phenomenological level to incorporating effects from smaller scales such as chemical adhesion. Though an adhesive theory of friction was proposed as early as 1734 by Desaguliers, it was long rejected due to an apparent contradiction with Amontons' 2nd law. In the 1950s, Tabor and Bowden performed seminal experiments with metal-metal surfaces and verified that adhesion indeed is a major component of friction [15]. Their micro-contact interface model lead to the introduction of the so-called *true area of contact*, which consists of the numerous small contact areas of the microscopic asperities of the surfaces, and is usually very small compared to the apparent surface area (approximately 0.1%). The concept of true contact area reconciled the adhesion-based friction of Desaguliers and the observed independence of the area of contact dictated by Amontons' 2nd law.

Modern experiments have uncovered various other facts about the nature of dry friction. In fact, even the term "dry friction" has turned out to be a bit misleading, since contaminants from the surrounding environment will always adhere to both surfaces, providing a small lubrication layer of sorts [16]. Experiments performed in high vacuum and with atomically smooth surfaces resembling truly dry friction have demonstrated phenomena deviating from the conventional concept of dry friction, such as cold-welding, where two smooth (typically metal) surfaces adhere to each other very strongly [17].

It has been realized that in the absence of contaminants and other environmental effects, the *commensurability* (ratio of lattice constants) of the materials in contact plays a large role in the observed friction behaviour. S. Aubry predicted in 1978 that sufficiently rigid, incommensurate (the ratio of lattice constants is an irrational number) lattices would display vanishing amounts of friction (*superlubricity*) [18]. This kind of elimination of friction

has been one of the primary motivations for dry friction research due to the considerable amount of potential applications. Superlubricity arising from incommensurability has recently been successfully demonstrated in experiments with graphene surfaces as large as  $1 \text{ cm} \times 1 \text{ cm}$  [19]. However, it is not yet known how (or whether it is possible at all) to achieve superlubricity in larger scales and closer to ambient pressure, temperature and humidity. It has been proposed that one of the limiting factors in superlubricity is the appearance of stick-slip motion caused by elasticity of materials when dealing with macroscopic surfaces [20].

## 1.1 Stick-slip motion studies

The first laboratory experiments concerning frictional stick-slip motion were macroscopic in nature. The experimental setups usually followed the Burrige-Knopoff model or a derivation thereof, in which a collection of blocks (or beads) are attached to each other and to a driving ceiling or block via springs. The blocks are slowly driven on top of a rough surface and their displacements recorded continuously, providing data on avalanches. Analysing experimental results, W. F. Brace and J. D. Byerlee proposed in 1966 that stick-slip is one of the mechanisms behind shallow earthquakes [21]. The claim was later confirmed in a series of experiments, and the results heightened the interest in laboratory stick-slip motion studies.

Later on, the smaller scale mechanisms of stick-slip motion, especially those found in dry friction, became a subject of research, and sophisticated experiments were carried out in hopes to understand dry friction on a more fundamental level. Fig. 3 depicts one experimental setup in which the asperities of a surface were emulated by metal beads embedded on a wooden block [22]. The block was then driven atop a similarly beaded surface. Other popular experimental setups include surface force apparatus and various pin-on-disc configurations [23, 24].

Contemporary studies have concentrated increasingly on the micro- and nanoscopic stick-slip motion, perhaps owing to advances in measurement technology. Experiments have been performed using atomically thin monolayers [25] and NaCl crystals [26], among other systems. The emergence of atomic force microscopes has made it possible to drag nanoscale chains or surfaces on top of substrates and measure the forces involved [20]. These kind of microscopic experiments within a well-controlled environment make it easier to study only few selected effects contributing to stick-slip motion.

The systems used in the described experiments are examples of *self-organized criticality* [27]: the system does not need to have parameters tuned



to specific values to achieve criticality, but instead is driven towards the critical point repeatedly. Thus the system oscillates around the critical point, alternating between the pinned and unpinned states. Utilizing these kind of experimental setups is a useful way of obtaining large data sets of avalanches, from which the characterizing aspects of the motion such as critical exponents can be determined. Many experiments demonstrate the power law distributions of the slip events, but regular stick-slip motion has also been found [28].

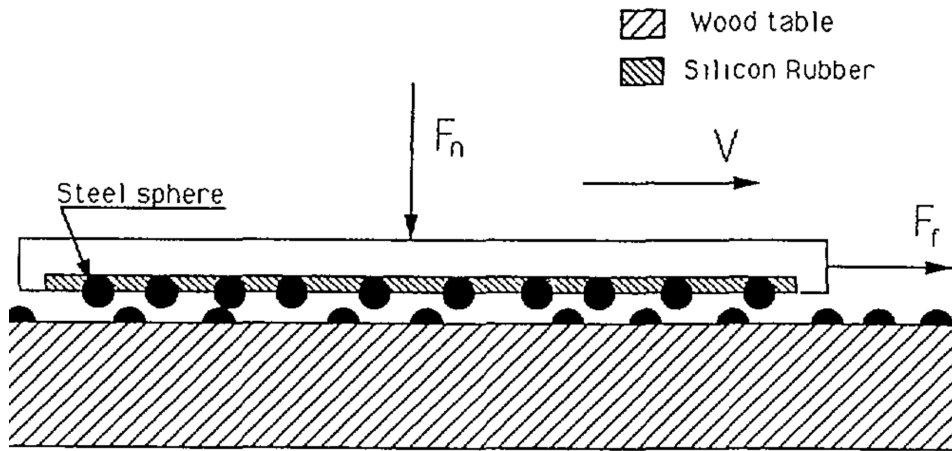


Figure 3: The experimental setup that was used to study stick-slip motion in Ref. [22].

One of the effects influencing stick-slip motion which is numerically investigated in this thesis, *contact aging* (the increase of static friction force with time), has also been studied in laboratory conditions. Experiments have shown that a multitude of effects can cause contact aging. The larger scale effects (for example moisture condensating between the surfaces and forming liquid bridges) can be studied with simple apparatuses, such as placing a block of material atop a plane and adjusting the inclination by a motor [9]. Recently, advanced experiments with atomic force microscopes have shown contact aging also in the nanolevel, likely resulting from individual atom bonding and bond breaking [29]. Despite the abundance of different origins of contact aging, a simple quasi-logarithmic time dependence for the increase in the static friction coefficient has consistently been found (more about this in Chapter 5).

## 1.2 Investigating the onset of motion

Only in relatively recent times has it become possible to experimentally investigate movement in small enough time and length scales to actually observe and record the processes leading to the depinning of surfaces and single avalanche events. Consequently, one of the emerging popular research topics is the transition from static to kinetic friction (the onset of frictional motion) and the mechanisms it entails.

Some recent experiments have had success in applying high-speed cameras and translucent blocks to perform real-time imaging of the true contact area [30, 31]. One such experimental setup is depicted in Fig. 4. With sufficiently high-speed and high-resolution cameras, this kind of setup can provide time and length resolutions up to a few micrometers and -seconds [31], which is enough to observe the behaviour of single asperities forming the true contact area. Such investigations of the surface deformation and depinning on a small scale are fascinating since they can provide information about how the single minuscule events contribute to the overall stick-slip motion, making way for novel theories that encompass micro- and nanolevel friction processes.

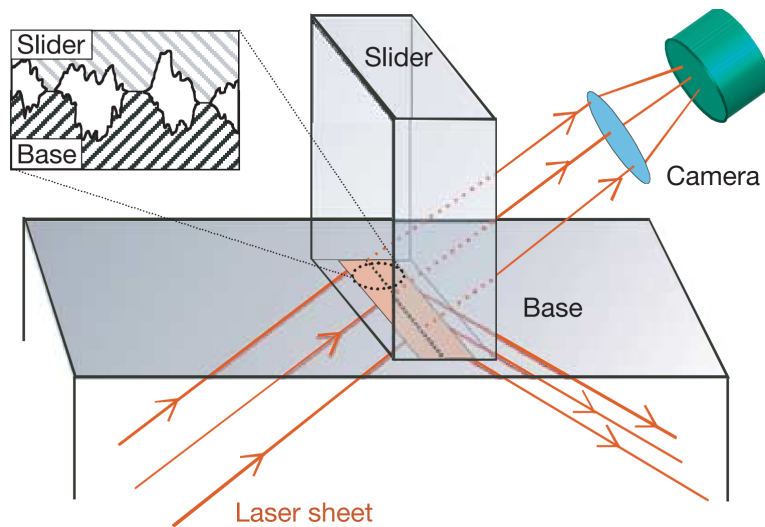


Figure 4: The experimental setup used in Ref. [31]: a translucent block (slider) is placed atop a translucent surface (base) and laser light is projected through the interface. The materials are such that the asperities in contact let the light through while in the base-air interface a total internal reflection happens. The light is captured via a camera, and the areas of contact are determined by the light intensity.

Indeed, modern experiments have yielded many interesting results, many of which are well presented in Ref. [32]. In addition to being able to verify the true contact area theory of Tabor and Bowden [33], renewal of the contact area during loading/unloading cycles and small avalanche events (*precursory events*) before actual movement of the sliding object have been observed. As an explanation for the contact renewal, Rubinstein *et al.* have proposed Poissonian expansion/contraction, in which the system expands/contracts in orthogonal directions as normal load is increased/decreased. The expansion and contraction also lead to contact aging and de-aging with time. The appearing of precursor events when increasing shear loading are shown to arise from a crack in the contact interface caused by the locally high shear stress in the trailing edge from which the load is applied.

A curious aspect of the onset of motion found in Ref. [31] is the crack-like process of contact rupture. It was observed that a slip starts with a front of contact area reduction (rupturing contacts) that propagates through the interface like a wave (Fig. 5), starting from the trailing edge where the block is pushed forward. The leading edge only moves after this wave has reached it. An unusual behaviour of the waves was also documented in the experiment: after reaching the Rayleigh velocity of the material, the waves split into two, one traveling with very high velocity and the other traveling very slowly. The slow-speed waves reduced the contact area significantly, whereas the fast waves had little effect on the area.

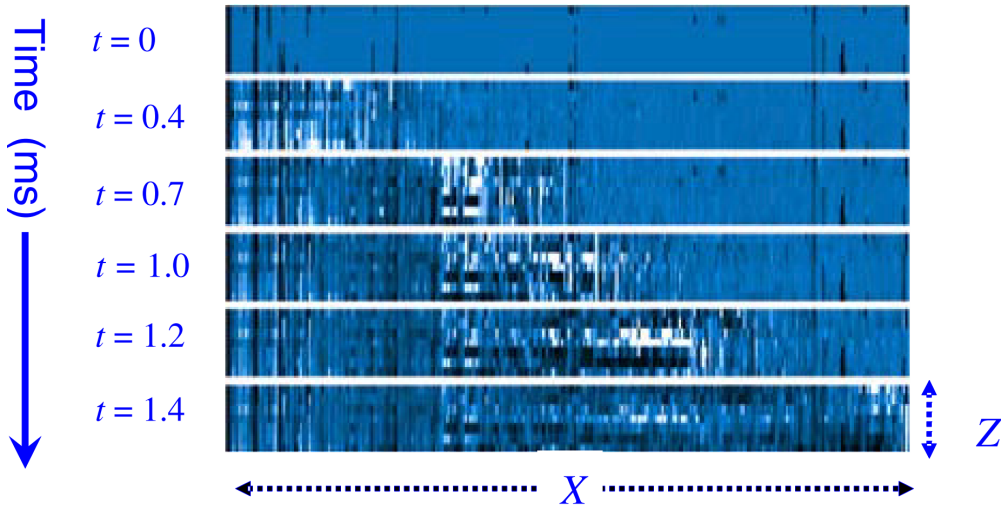


Figure 5: A time series depicting the increase (lighter shades) and decrease (darker shades) of contact area during the initiation of a slip event, displaying the wave-like propagation of the contact area (the block is pushed in the  $x$ -direction). [31]

## Chapter 2

# Minimalistic models for dry friction

Alongside laboratory experiments, computational models have been and still are popular instruments in qualitative and quantitative analysis of friction. Broadly speaking, there are two approaches to nano- and mesoscale modeling of friction: minimalistic models and molecular dynamics simulations [14], both of which have their own advantages and shortcomings. The minimalistic models tend to make various simplifications and assumptions about the system, typically providing a qualitative view of the frictional processes. Sometimes this leads to difficulties in explaining the behaviour of the model in physical terms. Molecular dynamics simulations, on the other hand, use accurately modeled atomic interactions as a starting point, aiming for a more quantitative analysis of friction. With modern computers, even relatively large systems of particles can be simulated with high precision. However, the computational complexity still limits molecular dynamics to very short time and length scales.

In this thesis, a combination of two well-known and popular minimalistic models, the Tomlinson model and the Frenkel-Kontorova model, is used to study the stick-slip behaviour of an elastic chain on a disordered substrate in the absence of lubrication. The elastic chain can be interpreted in multiple ways. It can represent a monolayer or the lowest atomic layer of a crystalline block being dragged on the substrate, the disorder representing atomic defects on the surface. On a larger scale, the individual particles of the chain could be thought to represent the asperities of the above surface, and the disorder of the potential would then mimic the microscale roughness of the substrate.

## 2.1 Tomlinson model

Tomlinson model (also known as Prandtl-Tomlinson model) is one of the simplest nanotribological models for dry friction. It was first suggested by L. Prandtl in 1928 to describe plastic deformations in crystals. More recently, it has been used in analyzing the behaviour of forces present in atomic force microscopes [34].

In the 1D Tomlinson model, a point mass (or multiple point masses, though in the absence of interparticle interaction there's little difference) is driven by an external force along a rigid substrate represented by a potential surface. The basic Tomlinson model is illustrated in Fig. 6. Neglecting the random force due to temperature, the particle obeys the equation of motion

$$m\ddot{x} = F_d + F_s(x) - \eta\dot{x}, \quad (2.1)$$

where  $x$  is the coordinate of the moving particle and  $m$  its mass,  $F_d$  is the driving force,  $F_s$  is the force due to interaction with the substrate and  $\eta$  is the damping coefficient. The potential surface is usually taken to be sinusoidal or some other periodic function. The driving is typically elastic, represented with a spring dragging the particle with velocity  $V$ , such that  $F_d(t) = k_0(x_0 + Vt - x)$ , where  $x_0$  is the starting location of the particle and  $k_0$  is the spring constant of the driving spring.

Despite the simplicity of the Tomlinson model, it captures many properties of friction at the nanoscale, such as the appearance of static friction and different kinds of movement regimes for under- and overdamped motion (superlubricity and stick-slip motion, respectively) [35].

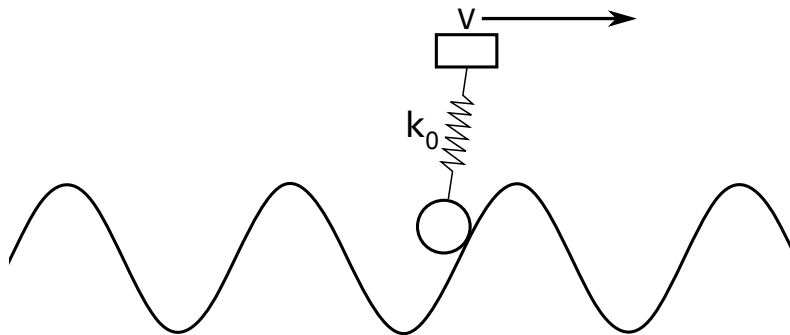


Figure 6: Depiction of the Tomlinson model with a single particle on a sinusoidal potential surface.

## 2.2 Frenkel-Kontorova model

Frenkel-Kontorova (FK) model is a general computational model that can be utilized in various different physical systems. It was first conceived in 1938 by Y. Frenkel and T. Kontorova, who used the model to study the dynamics of a crystal lattice near a dislocation core. Later on, the FK model has been applied to other nonlinear nonequilibrium phenomena, such as DNA dynamics, adsorbed atomic layers and friction [36]. In continuum, the Frenkel-Kontorova model with sinusoidal potential becomes the exactly integrable sine-Gordon equation. The sine-Gordon equation (and by extension, the Frenkel-Kontorova model) is attractive in friction studies because it exhibits elementary excitations also known to occur in the interaction between solid surfaces undergoing relative movement, most notably topological solitons (*kinks* and *antikinks*). [37]

The basic 1-dimensional Frenkel-Kontorova model consists of a chain of particles with nearest neighbor interactions atop a substrate-induced potential. In contrast to the Tomlinson model, the FK model has the interparticle interaction as the main contributor to the dynamics instead of driving. Thus there are two competing mechanics: the interparticle interaction and the interaction with the potential surface, leading to different kinds of relaxation depending on the strength ratio of these interactions (Fig. 7).

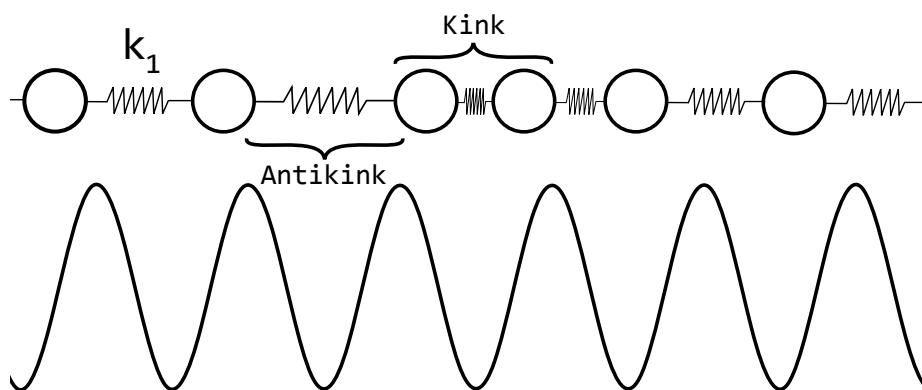


Figure 7: A simple Frenkel-Kontorova system exhibiting a kink-antikink (compression-expansion) pair due to mismatched lattice constants between the surface and the chain.

The equation of motion for particle  $i$  in the FK model with zero temperature, periodic boundary conditions, uniform elastic interparticle interaction (springs) and without external driving is

$$\begin{aligned} m\ddot{x}_i &= k_1(x_{i+1} - x_i - a_0) - k_1(x_i - x_{i-1} - a_0) - F_s(x_i) \\ &= k_1(x_{i+1} + x_{i-1} - 2x_i) - F_s(x_i), \end{aligned} \quad (2.2)$$

where  $k_1$  is the spring constant of the interparticle springs,  $a_0$  the equilibrium distance between two particles and  $F_s(x_i)$  the force from substrate-particle interaction at the location of a particle  $x_i$ , similarly to the Tomlinson model.

## 2.3 Frenkel-Kontorova-Tomlinson model

As its name implies, the Frenkel-Kontorova-Tomlinson (FKT) model is a unification of the Frenkel-Kontorova and Tomlinson models: the external driving from the Tomlinson model is combined with the interatomic interactions of the Frenkel-Kontorova model. From Eqs. (2.1) and (2.2), we obtain the equation of motion for a single particle in the one-dimensional case:

$$m\ddot{x}_i = F_d + k_1(x_{i+1} + x_{i-1} - 2x_i) + F_s(x_i) - \eta\dot{x}_i. \quad (2.3)$$

The system then consists of the substrate and  $N$  particles, each driven by a force  $F_d$  and attached to its neighboring particles with springs of spring constant  $k_1$ . From the equation of motion one can see that the FKT model has three competing interactions: the driving, the nearest-neighbor interparticle interaction and the particle-substrate interaction. The relative strength and rate of change (for example, how the driving force increases with time) in these interactions determines the behavior of the system.

In the context of this work we consider an overdamped system, in which the acceleration term  $m\ddot{x}_i$  can be neglected. This makes calculations easier and is often a good approximation for friction processes because of their highly dissipative nature. The driving of the system can be executed in various ways, the most popular being constant force or constant velocity driving via springs. Since the latter approach can be used to obtain a large amount of avalanches, it was the main focus of this thesis. The driving force for each spring in this case is the same as in spring-driven Tomlinson model,  $F_d(x_i) = k_0(x_{0i} + Vt - x_i)$ , where the driving spring stiffness  $k_0$  is taken to be equal for all particles. The springs are attached from their other end to a driving slab which is dragged forward with a constant velocity  $V$ .

The driving direction relative to the chain can be chosen to be perpendicular or parallel. In parallel driving, all the particles are on the same potential

surface (a true 1D case), whereas in the perpendicular driving each particle has its own randomized potential surface (representing different parts of the substrate in the direction of the chain). Fig. 8 depicts the scheme of the FKT model along with the different ways of driving. Though the perpendicular and parallel driving cases appear very different, previous works seem to indicate that the driving direction has little effect on the results [5, 38, 39].

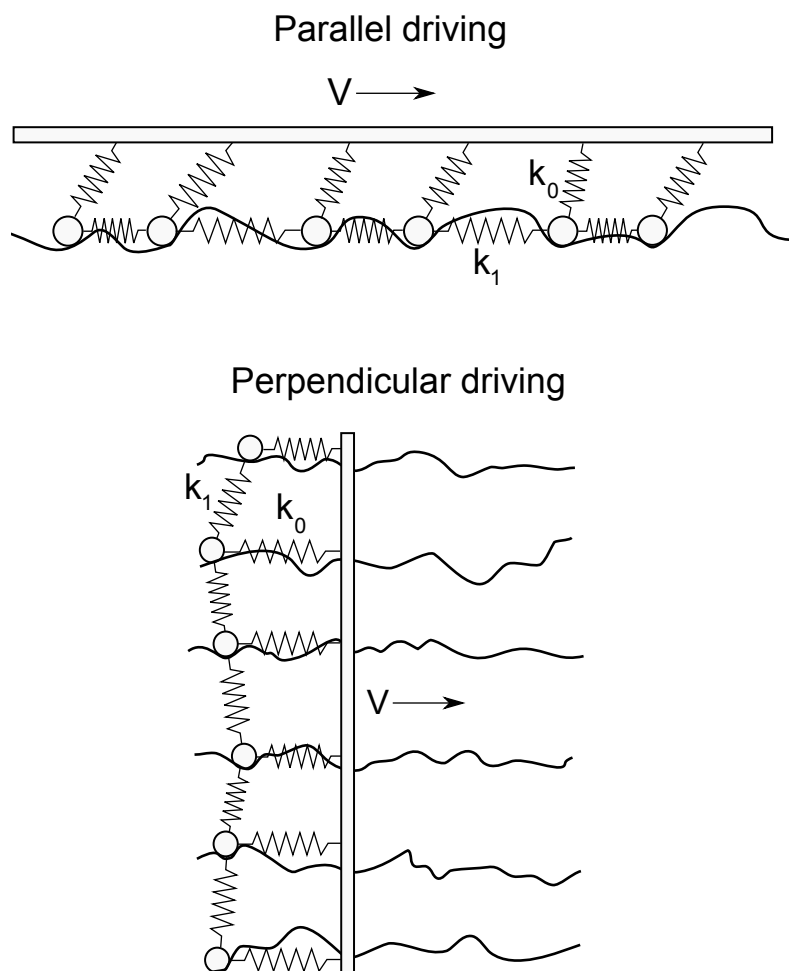


Figure 8: The 1-dimensional Frenkel-Kontorova-Tomlinson model and the two possible ways of driving. Periodic boundary conditions are not shown in the picture. In the case of perpendicular driving, the particles are locked in place in the direction perpendicular to the driving slab.



Reorganizing the terms in Eq. (2.3), dropping the acceleration term due to the overdamped system and inserting the constant velocity driving in place of  $F_d$  we find the equation of motion for a single particle  $i$ :

$$\eta \dot{x}_i = k_0(x_{0i} + Vt - x_i) + k_1(x_{i+1} + x_{i-1} - 2x_i) + F_s(x_i). \quad (2.4)$$

As for  $F_s(x_i)$ , we use a potential surface consisting of numerous randomly distributed Gaussian potential wells to represent a naturally rough substrate. The force  $F_s(x_i)$  affecting particle  $i$  due to a single potential well located at point  $x$  is thus defined as

$$F_s(x_i) = C(x - x_i)e^{-\frac{1}{2}\frac{(x-x_i)^2}{\sigma^2}}, \quad (2.5)$$

where  $C$  and  $\sigma$  are the depth and width of the potential well, respectively.

When driven with small  $V$  and  $k_0$ , the system exhibits stick-slip motion [40]. The stick-slip motion has two characteristic timescales determined by  $k_0$ ,  $k_1$  and  $F_s$ : the timescale in which the driving force becomes large enough to cause a new avalanche ( $t_i$ , slip interval timescale), and the timescale in which an avalanche is exhausted ( $t_d$ , slip duration timescale). In the ideal case, the driving is very slow compared to the response of the particles, so that the driving force during avalanches remains constant and the timescales are well separated ( $t_d \ll t_i$ ).

## Chapter 3

# Avalanche statistics

Computer simulations are advantageous in that all "observables" of the system are explicitly known at all times. Hence the main priority when conducting simulations and analyzing the results is determining the physical quantities of interest and their behaviour when various control parameters are changed. This chapter introduces the quantities that were primary objects of study in this thesis and explains how they are related to each other and to the parameters of the FKT model.

### 3.1 Correlation length, interface roughness and avalanche distributions

A quantity strongly related to many properties of the system is so-called *correlation length*, denoted by  $\xi$ . In general, correlation length is a measure representing the order in a system. In the case of the FKT model, this means how the positions of the particles are correlated in space. After a section of the FKT particle chain has experienced an avalanche, the positions of the particles in that section are strongly correlated (Fig. 9).

When a system is driven closer the critical force  $F_c$ , avalanches become larger and larger, and the correlation length grows accordingly. At the critical force, the system depins completely. In the thermodynamic limit (number of particles goes to infinity), this leads to an infinite-sized avalanche and a sharp phase transition characterized by the divergence of the correlation length, whereas in any finite system, the transition from pinned to depinned state is gradual and the correlation length has a well-defined maximum (the length of the system). The relationship between the distance to criticality

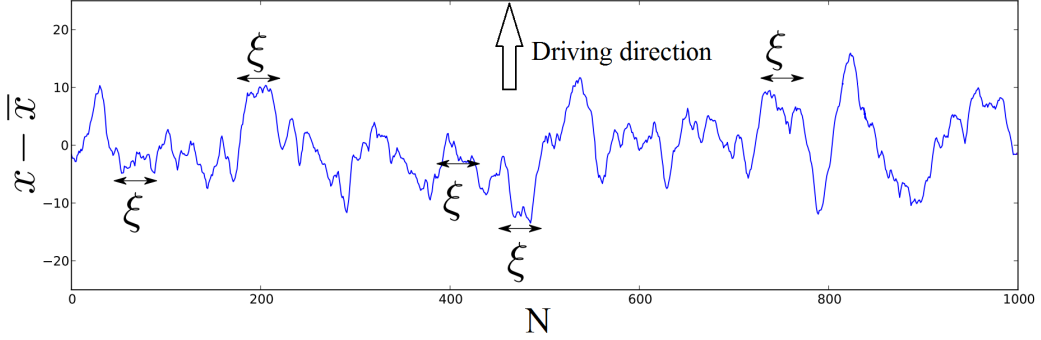


Figure 9: An illustration of the correlation length in a perpendicularly driven chain.  $N$  is the number of the particle and  $x - \bar{x}$  is the deviation from the mean displacement. Here  $\xi \approx 40$ . Picture adapted from [5].

and the correlation length is characterized by the critical exponent  $\nu$ :

$$\xi \propto |F - F_c|^{-\nu}. \quad (3.1)$$

Above the critical force  $F_c$ , the particle chain is never completely stationary, even though it may contain unmoving sections. In this case, the correlation length can be thought of as representing the correlations in the moving interface, being finite even when above the critical force [5].

With constant velocity driving, the driving force and by extension the distance to criticality depend on the driving velocity  $V$  and the spring constant of the driving spring  $k_0$ . Consequently, correlation length also becomes a function of  $V$  and  $k_0$ . In the stick-slip motion regime (quasistatic driving  $V = 0^+$ ), the correlation length attains a dependence on the ratio of the driving spring stiffness and the interparticle spring stiffness [5]. The dependence can be found by considering the energies of particles in a system of length  $l$ . The energy  $E_d$  stored in the driving springs and the energy  $E_p$  stored in the interparticle interactions can be written as

$$\begin{aligned} E_d(N) &= \frac{k_0}{2} \sum_{i=1}^N (d_i)^2, \\ E_p(N) &= \frac{k_1}{2} \sum_{i=1}^N (\Delta d_i)^2, \end{aligned} \quad (3.2)$$

where  $N$  is the number of particles in length  $l$ ,  $d_i$  is the distance to the driving slab and  $\Delta d_i$  is the distance between two neighboring particles. From the above equation, it can be inferred that the driving energy increases proportionally to the number of particles in the system and the driving spring

stiffness, i.e.  $E_d \propto k_0 N$ . The total energy of the interparticle interactions also scales with  $N$ , but  $\Delta d_i$  scales inversely proportionally to the density of the particles, which in a fixed-length chain means scaling inversely proportionally to the number of particles:  $\Delta d_i \propto 1/N$ . Hence we find out the scaling of the energies with  $N$ :

$$\begin{aligned} E_d(N) &\propto k_0 N, \\ E_p(N) &\propto k_1 N \left(\frac{1}{N}\right)^2 = k_1 N^{-1}. \end{aligned} \quad (3.3)$$

For large  $N$ , the driving energy contribution dominates over the interparticle interaction and the particles are mostly uncorrelated. With smaller values of  $N$ , the interparticle energy term becomes significant, resulting in highly correlated displacements. Hence it's natural to define the correlation length as the number of particles where the contributions from driving and interparticle interactions match. This way we find how the correlation length scales with  $k_0$  and  $k_1$ :

$$\begin{aligned} E_d(\xi) &\propto E_p(\xi) \\ \implies k_0 \xi &\propto k_1 \xi^{-1} \\ \implies \xi &\propto \left(\frac{k_1}{k_0}\right)^{1/2}. \end{aligned} \quad (3.4)$$

As Eq. (3.4) shows, increasing the strength of the interparticle interactions (spring stiffness  $k_1$ ) increases the correlation length. Thus correlation length also serves as a measure of rigidity of the system.

In numerical simulations, the width of avalanches (as in how many particles take part in the avalanche) ranges from 1 up to the correlation length. In order to avoid finite-size effects arising from reaching or exceeding the correlation length,  $k_0$  and  $k_1$  were chosen such that the correlation length is less than the size of the system. Appendix B elaborates on the effects of having correlation length equal to the system size.

Related to correlation length is a measure called *interface roughness* (or *typical width*)  $W$ , which in the 1D FKT model is defined as the standard deviation of the displacements of the particles [39]:

$$W(t) = \sqrt{\frac{1}{N} \sum_{i=0}^N (x_i(t) - \bar{x}(t))^2}, \quad (3.5)$$

where  $N$  is the amount of particles,  $x_i(t)$  is the displacement of particle  $i$  at the time  $t$  and  $\bar{x}(t)$  is the mean value of the displacements. Though the interface roughness is a function of time due to the repositioning of the particles during avalanches, near the critical point (i.e. after some driving if

the chain starts at rest) it attains a fairly stable value that scales with the correlation length via the so-called *roughness exponent*  $\zeta$ :

$$W \propto \xi^\zeta. \quad (3.6)$$

In the constant velocity driving simulations, the roughness exponent  $\zeta$  can then be determined with the help of Eq. (3.4) by considering how the interface roughness behaves as a function of the driving spring stiffness  $k_0$  when  $k_1$  is held constant:

$$W \propto k_0^{-\zeta/2}. \quad (3.7)$$

In the perpendicular driving case, the notion of roughness is intuitive. However, roughness can be defined similarly for the parallelly driven chain, one just has to take into account that the displacements are in relation to driver (which is not equal for all particles in the parallel case). [39].

When driven for long enough, the simulated system generates a large ensemble of avalanches with varying sizes and durations. The avalanche intervals (times between avalanches) are also of interest. Determining the sizes, durations and intervals of the avalanche events can be accomplished in a couple of ways. One method is measuring the drops of the friction force, in which the local maxima and minima indicate the beginning and end of a slip, respectively. This way of slip characterization is illustrated in Fig. 10.

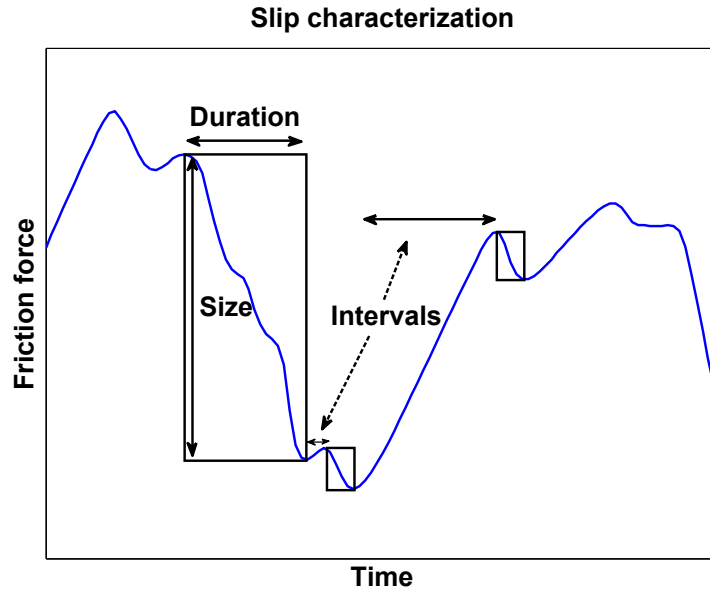


Figure 10: Determining the slip sizes, durations and intervals from the friction force drops.

Another method, which was primarily used in this thesis, is to set a certain velocity threshold and identify the start and end of an avalanche as the events of particles crossing the threshold and falling below the threshold, respectively. The avalanche sizes can then be calculated from the total movement of the particles while above the threshold. Both methods for determining slips are more closely examined in the next chapter.

The main interest in the avalanche events lies in their probability density distributions. To save space, the word "probability density" is hereafter omitted in the thesis, and all probability density distributions will be referred to only as "distributions". The distributions of interest are the avalanche size distribution  $P(S)$ , the avalanche duration distribution  $P(T)$  and the avalanche interval distribution  $P(I)$ . The size and duration of the avalanche events are distributed as power laws with certain critical exponents and cut-off values [5]. The interval distribution is controlled mostly by how the system is driven, and thus it's difficult to determine whether the distribution is a simple power law distribution or something more complex. Some results obtained in this work would seem to indicate that the interval distribution is similar to a power law, at least within a certain parameter regime.

The size and duration distributions are of the form

$$P(X) = X^{-\tau_X} g\left(\frac{X}{X_0}\right), \quad (3.8)$$

where  $X$  is the quantity in question and  $\tau_X$  the critical exponent corresponding to the quantity. Here  $g(x)$  is a cut-off function which decays rapidly when  $x > 1$ , and  $X_0$  is the cut-off value.

The cut-off values of these distributions are controlled by several parameters. The cut-off of the avalanche size distribution  $S_0$  is related to the dimension of the system  $d$ , correlation length  $\xi$  and roughness exponent  $\zeta$  [5]. The relation between these quantities is

$$S_0 = \xi^{d+\zeta}. \quad (3.9)$$

Using Eq. (3.4) for correlation length, we can find out how the cut-off of the size distribution behaves as a function of the driving spring stiffness:

$$S_0 \propto k_0^{-(d+\zeta)/2}. \quad (3.10)$$

The cut-off for avalanche duration is also related to the correlation length, but with it's own critical exponent, the *dynamic exponent*  $z$ :

$$T_0 \propto \xi^z \propto k_0^{-z/2}. \quad (3.11)$$

## 3.2 Scaling relations

The exponents described in the previous section are not totally independent, but instead related to each other via so-called *scaling relations*. These relations can be used to reduce the number of exponents to keep track of, and to verify the correctness of the values obtained from simulations. Scaling relations can be written in various forms, depending on which exponents one decides to use to calculate others. In this thesis, the scaling relations are based on the roughness exponent  $\zeta$  and dynamic exponent  $z$ , which are used to predict theoretical values for the critical exponents of size and duration distributions ( $\tau_S$  and  $\tau_T$ , respectively).

For the avalanche size, we can establish a scaling relation by considering that on average, the total distance traveled by the particles during a slip (denoted as  $\Delta x$ ) scales proportionally to the average force a slip relaxes and inversely proportionally to the driving spring stiffness,  $\langle \Delta x \rangle \propto \frac{\langle \Delta F \rangle}{k_0}$ . However, the average force relaxed by a slip is a constant depending on properties of the surface and the chain. Thus we get

$$\langle \Delta x \rangle \propto \frac{1}{k_0} \propto \xi^2. \quad (3.12)$$

The size of a slip,  $S$ , is equal to the total movement  $\Delta x$ , and thus we know that  $\langle S \rangle = \langle \Delta x \rangle \propto \xi^2$ . On the other hand, the average avalanche size can be calculated directly from power law part of the probability density distribution:

$$\langle S \rangle = \int_0^{S_0} S P(S) dS = \int_0^{S_0} S \cdot S^{-\tau_S} dS \propto S_0^{2-\tau_S}. \quad (3.13)$$

Equating these results and remembering from Eq. (3.9) that  $S_0 \propto \xi^{d+\zeta}$ , we get the scaling relation for  $\tau_S$ :

$$\begin{aligned} \xi^2 &= \xi^{(d+\zeta)(2-\tau_S)} \\ \implies 2 &= (d+\zeta)(2-\tau_S) \\ \implies \tau_S &= 2 - \frac{2}{d+\zeta}. \end{aligned} \quad (3.14)$$

The scaling relation for slip duration critical exponent  $\tau_T$  can be derived with the help of the above scaling relation, the fact that  $S = T^{(d+\zeta)/z}$  (from Ref. [5]), and the transformation property of probability density functions:

$$P(T) = \left| \frac{dS}{dT} \right| P(S). \quad (3.15)$$

Since the avalanche durations cannot be negative, the derivative  $\frac{dS}{dT}$  is always positive and we can leave out the absolute value, leading to

$$\begin{aligned} P(T) &= T^{\frac{d+\zeta}{z}-1} P(S) \\ \implies T^{-\tau_T} &= T^{\frac{d+\zeta}{z}-1} S^{-\tau_S}. \end{aligned} \quad (3.16)$$

Noting that  $S^{-\tau_S}$  is equal to  $T^{-(\frac{d+\zeta}{z})\tau_S}$ , we can write Eq. (3.16) as a function of  $T$  only, and then compare the exponents:

$$\begin{aligned} \implies T^{-\tau_T} &= T^{\frac{d+\zeta}{z}-1-(\frac{d+\zeta}{z})\tau_S} \\ \implies -\tau_T &= \frac{d+\zeta}{z} - 1 - \left(\frac{d+\zeta}{z}\right)\tau_S. \end{aligned} \quad (3.17)$$

Now we can utilize the scaling relation for  $\tau_S$  to get

$$\begin{aligned} \tau_T &= 1 - \frac{d+\zeta}{z} + \left(\frac{d+\zeta}{z}\right)\left(2 - \frac{2}{d+\zeta}\right) \\ &= 1 + \frac{d+\zeta-2}{z}. \end{aligned} \quad (3.18)$$

Based on the critical exponents, stick-slip motion (and critical phenomena in general) can be divided into several *universality classes*: systems which have similar fundamental dynamics near the critical point which typically depends only on few so-called *relevant* parameters (such as dimensions and the range of the interactions within the system), instead of e.g. material parameters. As an example, the case where all particles interact (*fully connected model*), i.e. mean field stick-slip dynamics, is a universality class characterized by avalanche size and duration critical exponents  $\tau_S = 3/2$  and  $\tau_T = 2$ , respectively. The nearest neighbor interactions present in the model of this thesis and some previous work tend to yield exponents  $\tau_S \approx 1.1 - 1.3$  and  $\tau_T \approx 1.2 - 1.4$  [5, 39]. Expanding the range of the interactions or increasing dimensionality of the model takes it closer to the mean field case.



## Chapter 4

# Implementation of the FKT model

In this thesis, a computer program was developed to simulate the stick-slip motion of the one-dimensional FKT chain presented in Chapter 2. C++ was chosen as the programming language due to its relative simplicity and decent performance. The numerical integration of the equations of motion in Eq. (2.3) was done with a fourth order Runge-Kutta method, since it was deemed good enough in terms of stability and accuracy. To obtain smooth distributions for avalanche sizes, durations and intervals, a large number of simulations with different random seeds (and thus different potential surfaces) were run in parallel, after which the statistics compiled into single files for analysis.

Two external libraries were utilized in the work: a Mersenne twister random number library `mtwist.h` by Geoff Kuenning [41] and a spline construction library `spline.h` by Tino Kluge [42]. Both are distributed under the GNU Library General Public Licence.

### 4.1 Simulation basics

The disordered potential surface was created by randomly distributing large amount of potential wells (*pinning centers*) in space. The space was then densely sampled and a natural cubic spline of the potential was calculated. This speeds up the simulation, since one does not have to evaluate the multiple exponential functions of the interactions between pinning centers and individual particles, but instead just calculate the value from the spline, evaluating a single third-order polynomial. A typical potential surface created this way is shown in Fig. 11.

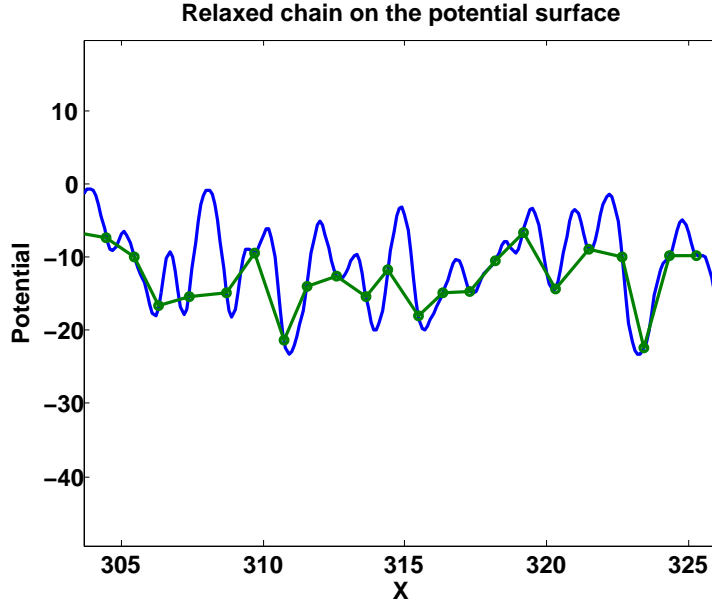


Figure 11: A short slice of a potential surface (blue curve) with a relaxed parallel particle chain (green dots connected by line). The units are arbitrary.

At the beginning of the simulation, the particle chain is placed on the potential surface and let relax. After the relaxation, the driving slab starts moving forward, increasing the driving force. At some point, determined by checking if each particle has traveled a specific distance along the surface, the chain reaches a steady state. In the steady state, the driving force stays consistently near the critical force, only experiencing small drops due to avalanches. The simulations are thus separated into two phases, the onset of motion and the steady state, both of which were studied in this work. During the onset of motion, the positions and velocities of the particles are recorded every few timesteps, providing accurate data about the behaviour of the chain at the beginning phase of the simulation. In the steady state, the avalanche size, duration and interval data is collected until a sufficiently large amount of events have been obtained.

As mentioned in Chapter 3, the avalanche events were registered either as the drops in the friction force or via the velocity threshold, and the two different methods should in principle give similar results. In the friction force method, the friction force, defined as the sum of all the forces due to the springs driving the system,  $F_{tot}(t) = \sum_{i=1}^N k_0(Vt - x_i(t))$ , is monitored during each timestep. When the force starts to decrease, the maximum force  $F_{dmax}$  and the simulation time  $t_1$  are stored in memory. Once the force starts

increasing again, the minimum force  $F_{dmin}$  and time  $t_2$  are stored, and the slip size is then calculated as

$$S_{FD} = \frac{F_{dmax} - F_{dmin}}{k_0}, \quad (4.1)$$

where  $S_{FD}$  stands for the slip size measured via the friction force derivative method. The durations of the slips and the intervals between them are calculated from the stored times: the duration is  $T = t_2 - t_1$  and the interval  $I = t_1^{(2)} - t_2^{(1)}$ , where the superscripts denote two consecutive avalanche events.

In the velocity threshold method, the recording of slip events went according to the following: when a particle crosses the relaxation velocity threshold (henceforth shortened as RVT) the sum of the locations of all particles  $x_{tot}(t_1) = \sum_{i=1}^N x_i(t_1)$  is saved into memory. Once the chain has relaxed, indicated by the velocity of each particle dropping below the RVT, the locations of the particles are saved again as  $x_{tot}(t_2)$ . The size of the avalanche is thus the total distance covered by the particles:

$$S_{RVT} = x_{tot}(t_2) - x_{tot}(t_1) = \sum_{i=1}^N (x_i(t_2) - x_i(t_1)), \quad (4.2)$$

where  $S_{RVT}$  is the slip size measured by the relaxation velocity threshold method and  $t_1$  and  $t_2$  are the start and end times of the slip, respectively. The durations and intervals of the slips are calculated same way as with the force derivative method.

The velocity threshold and force derivative methods of determining slips are nearly equivalent, and when driven slowly and using the basic FKT model, both slip determination methods indeed give the same results. The minor differences between the methods are elaborated in Appendix A. For consistency, velocity threshold method was used in all the simulations.

## 4.2 The timescale issue

When simulating stick-slip motion with the Frenkel-Kontorova-Tomlinson or similar model, an approximation called *narrow wells approximation* and space discretization are typically used to improve calculation speed. In the narrow wells approximation, the potential wells forming the disorder are approximated as infinitesimally thin. This way the jumps made by particles in stick-slip motion are always discrete, and continuous integration with respect to time and space is not required [5]. In this thesis, however, such approximations were not made in order to preserve as much similarity to real stick-slip

motion as possible. However, this brings forth a problem related to the time span of the simulation.

When an avalanche event occurs in the system, the driving slab should stay as stationary as possible in order to not cause other avalanches, since the new avalanches would mix with the initial avalanche. This would in turn result in some avalanches being registered as too large and long in duration, distorting the avalanche distributions. The effect can be avoided by driving the system with smaller velocities. However, when the driving velocity is lowered, the simulation takes longer to reach the steady state, and the triggering of avalanches is also slowed down. In some cases, the simulation time could increase to somewhat intolerable levels.

Two approaches were used to mitigate the problem, the first being the option to stop the driving during avalanches, so that only one avalanche is resolved at a time. This removes the distortion from the avalanche distributions (Fig. 12), and thus the driving velocity is not as large an issue. However, the driving velocity still had to be sufficiently small to not induce multiple avalanches in one timestep. The velocity threshold also had an effect on the critical exponents of the distribution (more about this in Appendix A).

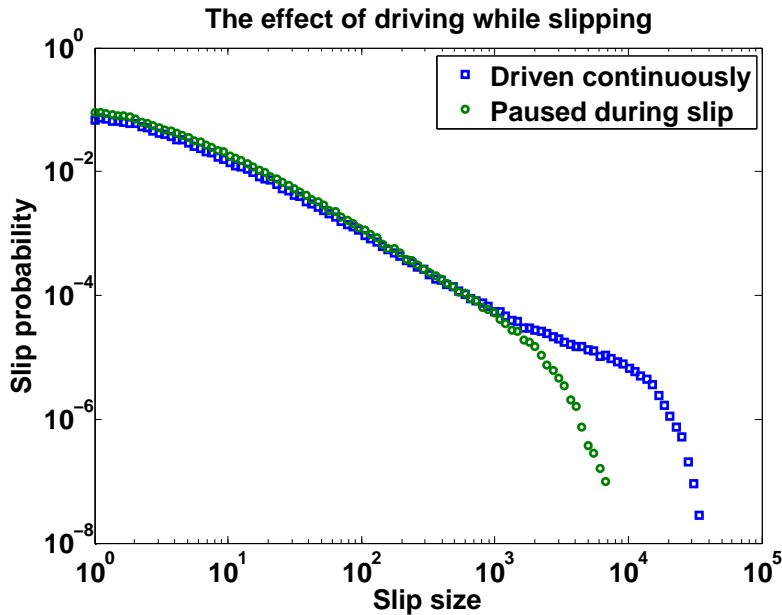


Figure 12: If the driving is not stopped while the system is slipping, multiple small slips can be accidentally recorded as one large slip, and thus the higher end of slip size distribution can become bloated. Similar effect happens with the duration distribution. The distributions in the picture were obtained with perpendicular driving.

To reach the steady state faster, a possibility was added to drive the system faster in the beginning (if not investigating the onset of motion), and slow down when the steady state is reached and the avalanche measurements started. This solution greatly sped up the simulation process, since reaching the steady state with low velocities could take considerable amount of time.

### 4.3 Control parameters

The simulation takes various parameters (*control parameters*) as input, for example the amount of particles, the length of the potential surface, the stiffnesses of the springs in the system. The disordered potential surface has quite a complex dependence on three parameter values: the depth and width of the potential wells, expressed as  $C$  and  $\sigma$  in Eq. (2.5), and the density of the wells  $\rho$ .

In a continuous simulation, the chain is continuously creeping forward, even when seemingly pinned. This can result in an unwanted accumulation of infinitesimally small "avalanches", which must be in some way distinguished from the actual avalanche events [5]. When the avalanches are measured by the drops in the total friction force, this is not an issue, since the total force still grows despite the small movements. In the velocity threshold case, the creep has to be taken into account by setting a sufficiently large velocity threshold to disregard the mini-slips caused by the creep. Additionally, an option to disregard slips that were beneath certain size was included in the simulation options.

The aim of the simulations was not to accurately emulate a specific physical material or situation, and thus the relations of the control parameters were more important than their actual values. Due to the large size of the parameter space, not all combinations could be tested; the most essential parameters were deemed to be the driving spring stiffness and the driving velocity, both of which need to be relatively small to reach the stick-slip motion regime. Since the properties of the simple 1D FKT model have been examined previously in literature [40, 43], the main point of this work was to alter the model with novel features introduced in the next chapter and see how the control parameters related to these features affected the dynamics.

## Chapter 5

# Augmenting the FKT model

Though exhibiting many properties encountered in friction, the purely elastic interactions of FKT model fail at describing frictional processes adequately. Both quantitative and qualitative differences exist when compared to experimental data [5]. The purpose of this work is to implement and investigate in the FKT model two properties that have seen less study but are widely considered to affect the dry friction between surfaces: viscoelasticity and contact aging. So far the research on the subject has been scarce, especially with continuous numerical models. An excellent study on viscoelastic effects in a discrete setting is in Ref. [5].

The goal was not to come up with the real physical interactions causing viscoelasticity and contact aging, but instead look at the consequences that these effects have in the stick-slip motion and the avalanche statistics. Therefore the effects are quite artificially plugged on top of the dynamics already present in the FKT model.

### 5.1 Viscoelasticity

Linear elastic materials obey Hooke's law ( $\sigma = E\epsilon$ ), meaning their stress response to a fixed strain is instant and linear with the proportionality constant  $E$ , the Young's modulus. Contrasting elasticity there are viscous materials, in which the stress is dependent on the strain rate instead of the strain itself:  $\sigma = \eta \frac{d\epsilon}{dt}$ , where  $\eta$  is the viscosity [44]. Though most solids are usually presented as linear elastic materials, no material is ideally elastic (even if the approximation is good in small deformation regimes). A natural extension in the treatment of solids is to include viscous effects, leading to a concept of viscoelasticity.

Viscoelastic materials exhibit both elastic and viscous characteristics. As a result, viscoelastic materials display various time-dependent phenomena, the most important in the context of this work being the *viscoelastic relaxation*, during which stress decreases with time as strain is held constant [44]. The stress-strain response in viscoelastic materials also exhibits hysteresis (curved response as seen in Fig. 13 bottom), differing from the straight line response of linear elastic materials.

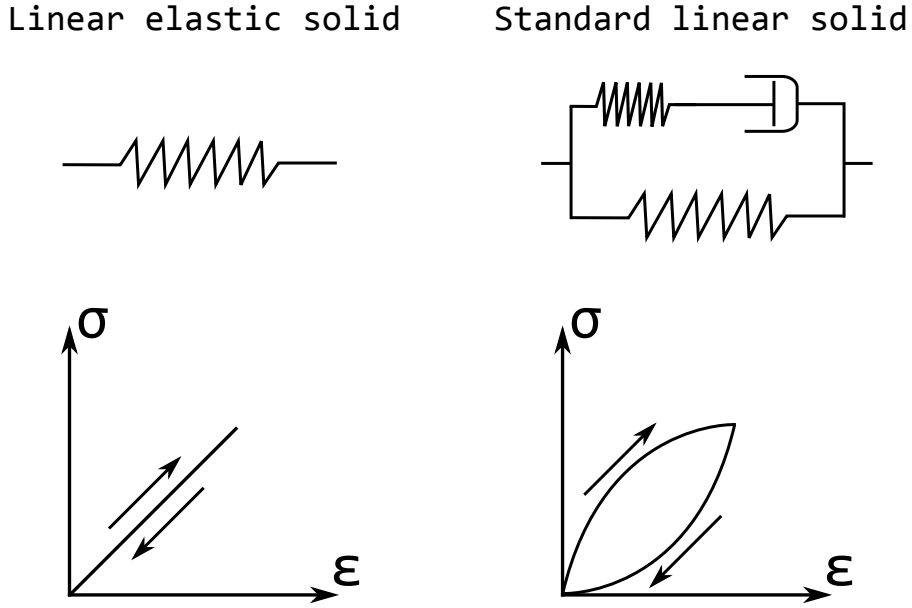


Figure 13: A mechanical circuit representation and the stress-strain curve of a linear elastic solid element versus a standard linear solid (viscoelastic) element during loading and unloading.

The inner relaxations of materials and the time-dependent response to external stimulus are considered to have a large impact in the frictional behaviour of solid surfaces [5, 13, 45]. Hence it's sensible to include viscoelastic effects in the FKT simulation, introduced to the model by replacing the springs between particles with standard linear solid (SLS) elements. The SLS elements consist of a spring and a dashpot in a series, parallel to another spring (Fig. 13 top). These elements add a new term to the dynamic equations of the particles, and a set of separate equations for the elongations of the dashpots [46]:

$$\begin{cases} \eta \dot{x}_i = k_0(x_{0i} + Vt - x_i) + k_1 \Delta x_i + k_2(\Delta x_i - u_i) + F_s(x_i) \\ \eta_u \dot{u}_i = k_2(\Delta x_i - u_i), \end{cases} \quad (5.1)$$

where  $k_2$  is the spring constant of the new springs and  $u_i$  and  $\eta_u$  are the elongation and viscosity of dashpot  $i$ , respectively (all dashpots are assumed to have the same viscosity).  $\Delta x_i$  is the distance between nearest neighbors written in a more concise notation. The spring constant and dashpot viscosity of the SLS elements become control parameters for the simulation.

The term  $k_2(\Delta x_i - u_i)$  represents the effect of the dashpots on the dynamics of the particles in Eq. (5.1). When the chain is completely relaxed, the elongations of the dashpots are equal to the distances of the particles,  $u_i = \Delta x_i \forall i$ , and the term  $k_2(\Delta x_i - u_i)$  is zero. However, if the relaxation of the dashpots is slow compared to the chain ( $\eta_u \gg \eta$ ), the dashpots don't have enough time to fully relax during avalanches. This leads to probably the most distinguishing feature of the viscoelasticity, the emergence of *aftershocks*: the relaxation of the dashpots takes place between avalanches, making it possible for new avalanches to occur without the increase in external driving. This introduces time-dependency even in a seemingly pinned state and memory effects which are absent when the interparticle interactions are purely elastic.

## 5.2 Contact aging

Another effect studied in this thesis is contact aging, already briefly touched upon in Chapter 1. Contrary to the phenomenological laws of friction, static friction is known to exhibit an increase over time, a phenomenon arising from various different causes. In fact, the viscoelastic effects described in the previous section have also been linked to contact aging [5]. Experiments have established that the static friction coefficient  $\mu_s$  grows with time roughly as

$$\mu_s(t) = \mu_0 + \alpha \ln(1 + t/t_\alpha), \quad (5.2)$$

where  $\mu_0$  is the static friction coefficient immediately after contact,  $\alpha$  is the adhesive increase coefficient for static friction, and  $t_\alpha$  is the characteristic contact aging timescale [9]. When the system slips, the contact aging is rapidly reversed due to the breaking of contact between asperities and atoms. In this thesis, a simple exponential function  $e^{-t/t_\beta}$ , was used to model the de-aging. Here  $t_\beta$  is the de-aging timescale ( $t_\beta \ll t_\alpha$ ).

The change of friction coefficient is implemented in the simulation by strengthening the surface force felt by a particle  $i$  remaining in place (determined by its velocity being below the relaxation velocity threshold) via a "surface force increase coefficient"  $\mu_i$ , which represents the term  $\alpha \ln(1 + t/t_\alpha)$  in Eq. (5.2). The coefficient  $\mu_i$  grows during the stick phase, and when a particle slips (crossing the relaxation velocity threshold),  $\mu_i$  drops back to 0



following the exponential function  $e^{-t/t_\beta}$ . The de-aging of the contact results in a rapid decrease in the friction force felt by the particle at the beginning of an avalanche. This behaviour is qualitatively depicted in Fig. 14. Contact aging increases the control parameters of the simulation by three, with  $\alpha$ ,  $t_\alpha$  and  $t_\beta$ .

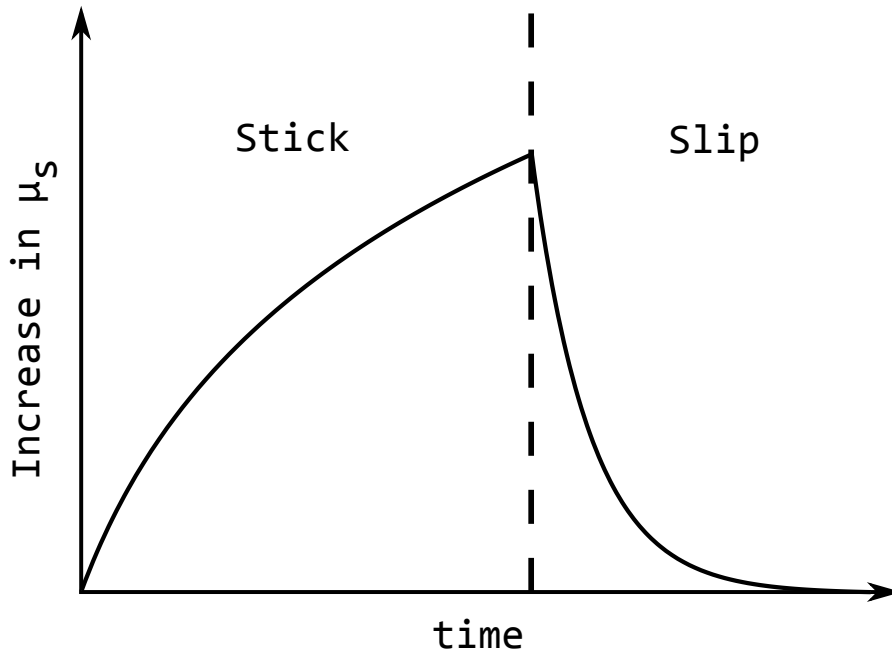


Figure 14: The logarithmic increase of the static friction coefficient  $\mu_s$  while pinned and the exponential drop when slipping.

The addition of contact aging to the stick-slip motion is likely to make the slip interval distribution skewed towards the larger interval side, since the force resisting movement grows with time along with the driving force. Depending on dragging velocity  $V$  and the adhesive friction increase coefficient  $\alpha$ , the time between slips can grow very high. However, due to the logarithmic increase in the friction force and linear increase in the driving force, the chain cannot become pinned for an indefinite amount of time.

Because of the aging contact, the occurring avalanches are likely to be larger and last longer, since generally a greater force is needed to unpin the chain. Another contribution to the avalanche size increase is the fact that the friction force due to contact aging vanishes very fast in an unpinning event, leading to less resistance when sliding.

## Chapter 6

# Results

The simulations conducted in this thesis are divided into four categories: the FKT model without either viscoelasticity or contact aging, then simulations with one of these effects, and finally with both effects on at the same time. Separate simulations were run for perpendicular and parallel driving. In the parallel driving case the particles at the ends of the chain were not connected, whereas in the perpendicular driving case the chain had periodic boundary conditions.

Since the magnitudes of the control parameters relative to each other were of more significance than the specific values themselves, some control parameters were fixed to a value and not altered in any simulations unless otherwise stated. These parameters are listed in Table 6.1. With parallel driving, the equilibrium distance between particles greatly influences the results, as it controls the relative density of the pinning centers with respect to the length of the chain. In the perpendicular driving case, the equilibrium distance is not a relevant variable (since the periodic boundary conditions eliminate it from the equations of motion), and so was simply set to 1.

Table 6.1: The constant control parameter values.

Control parameter	Value
Number of particles $N$	1000
Damping coefficient $\eta$	1
Interparticle spring constant $k_1$	1
Disorder strength parameter $D$	1
Well width $\sigma$	0.3
Pinning density $\rho$	2
Timestep $\Delta t$	0.1

## 6.1 The vanilla FKT model with a perpendicularly driven chain

The first simulations were performed with perpendicular driving and without the inclusion of viscoelastic effects or contact aging, to see if the results obtained from the model matched with those previously found in literature. Additionally, the effect of control parameters  $k_0$  and  $V$  to the onset of motion are documented. The onset of motion is relatively recent as a research subject, and thus there is not a lot of material covering it. Some experimental and numerical investigations can be found in Refs. [32] and [47].

### 6.1.1 Onset of motion

There are various quantities to study in the onset of motion, the most interesting being the friction force and the mean and individual values for the velocities and positions of the particles which show how the slip propagates in the chain. The velocities of the particles and the total friction force experienced by the chain as a function of time are presented in Fig. 15 for different values of  $k_0$ . Other control parameters are kept constant with values as presented in Table 6.2. Since avalanche statistics are not collected from the onset of motion, there was no need to stop the driving when the chain slips in these simulations.

From theory it is known that  $k_0$  has a dramatic effect on the movement due to increased correlation length, and this shows also in the simulations: with a stiff driving spring (Fig. 15 top), the avalanches are very small and highly localized. By contrast, with small  $k_0$  (Fig. 15 bottom) the avalanches cover relatively wide regions (with largest avalanches being roughly 200 particles wide) of the chain. The critical force becomes smaller with increasing  $k_0$ , since the driving starts to dominate over the nearest neighbor interactions, and the resulting local slips lower overall the friction force.

Table 6.2: The relevant control parameter values used when running the initial onset of motion simulations.

Control parameter	Value
Driving velocity $V$	0.005, 0.05
Driving spring stiffness $k_0$	0.1, 0.01, 0.001

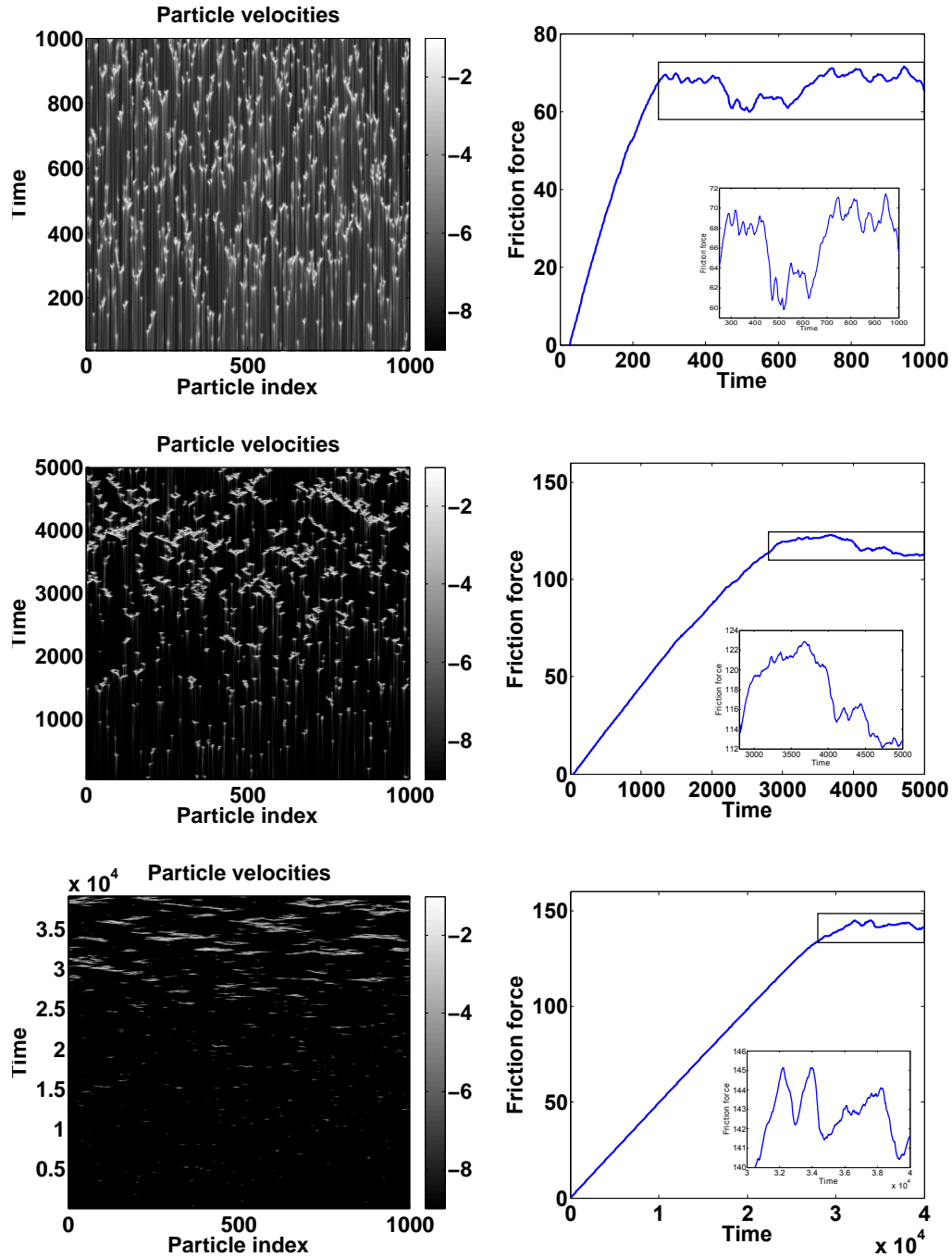


Figure 15: The growth of slip sizes when  $k_0 \rightarrow 0$  for a perpendicularly driven chain of 1000 particles. The values for  $k_0$  from top to bottom are 0.1, 0.01 and 0.001, respectively. The velocity values of individual particles (left) are shown in logarithmic scale for better viewability. The friction force (right) shows that the maximum friction force is smaller with  $k_0$  and it is achieved faster. Insets display enlarged view of the force fluctuations at the steady state.

The size of the force fluctuations appear larger in the higher  $k_0$  case, but this is likely due to the simultaneous slips and the fact that the data is averaged over 30 timesteps. Fluctuations caused by individual slips were seemingly independent of  $k_0$ . Since the avalanches don't cover the whole system, the fluctuations in the friction force are quite smooth instead of the typical sawtooth behavior observed in macroscopic stick-slip motion. However, system-wide slips (Appendix B) display a sawtooth-like curve.

Increasing the driving velocity also leads to fluid motion, but the mechanism seems to be a bit different: instead of the avalanches becoming smaller, new avalanches are started before the others are exhausted, and thus the system enters an infinite avalanche with only few temporarily stopped regions (Fig. 16). The steady state friction force is increased with the velocity and the fluctuations become smaller. The increase in friction force due to velocity has been observed in experiments and named *velocity strengthening* of dry friction [48]. A contrasting behaviour, *velocity weakening* is not present in the vanilla FKT model.

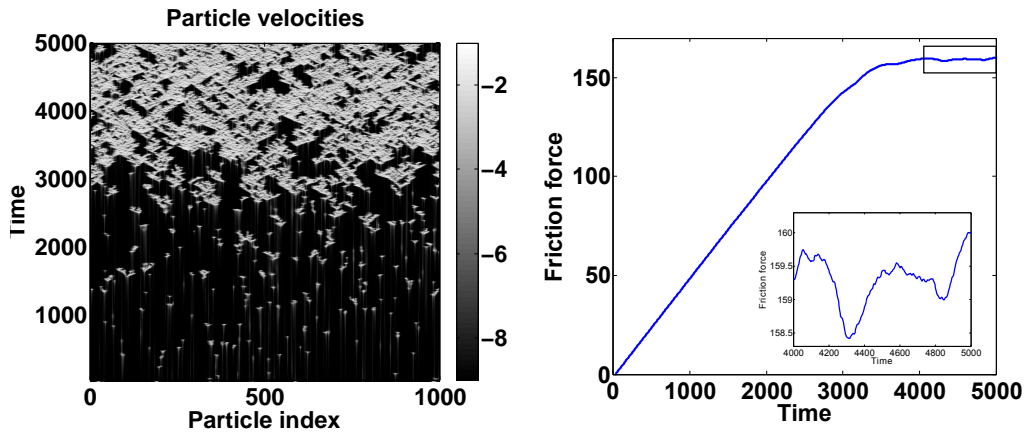


Figure 16: The smooth sliding due to increase in the driving velocity for the perpendicularly driven chain of 1000 particles. The velocity in this case is  $V = 0.05$ , i.e. tenfold compared to Fig. 15, and  $k_0 = 0.001$ . The inset illustrates the fluctuations in the steady state.

### 6.1.2 Avalanche statistics

The initial simulations concerning avalanches were conducted to see how the roughness and cut-off values for size, duration and interval distributions scaled with the driving spring stiffness  $k_0$ , in order to determine the roughness exponent  $\zeta$  and the dynamic exponent  $z$ . Much like in the onset of motion

simulations, the value of  $k_0$  was varied in the range  $10^{-3} - 10^{-1}$  while other parameters were kept constant (Table 6.3).

When investigating avalanche statistics, three new parameters affected the distributions: the way the slips are determined ("Slip characterization method" in Table 6.3), whether the driving is paused when the system slips ("Pause driving while slipping") and the velocity below which the particles are considered relaxed ("Relaxation velocity threshold"). The values in Table 6.3 for these three parameters gave results best conforming to those found in other literature. However, changing the parameters, different results were also obtained. The response of the system to the changes is discussed in Appendix A.

It was theorized that the maximum values of the distributions would scale similarly to the cut-off values, and thus the maximum values were measured instead of fitting an exponential cut-off function in each distribution (as this would've been tedious to do by hand for 60 different values of  $k_0$  and 3 distributions). The scaling of the values is plotted in Fig. 17. However, it was later noted that the maximum values of each distribution seem to not scale exactly with the same exponents as the cut-offs (demonstrated with slip size and duration cut-offs in Fig. 18), and so the dynamic exponent was determined using few accurate cut-off values instead.

Table 6.3: The control parameter values used when running the avalanche distribution simulations.

Control parameter	Value
Driving velocity $V$	0.005
Driving spring constant $k_0$	0.1 – 0.001
Driving paused while slipping	True
Slip characterization method	Velocity threshold
Relaxation velocity threshold	0.05

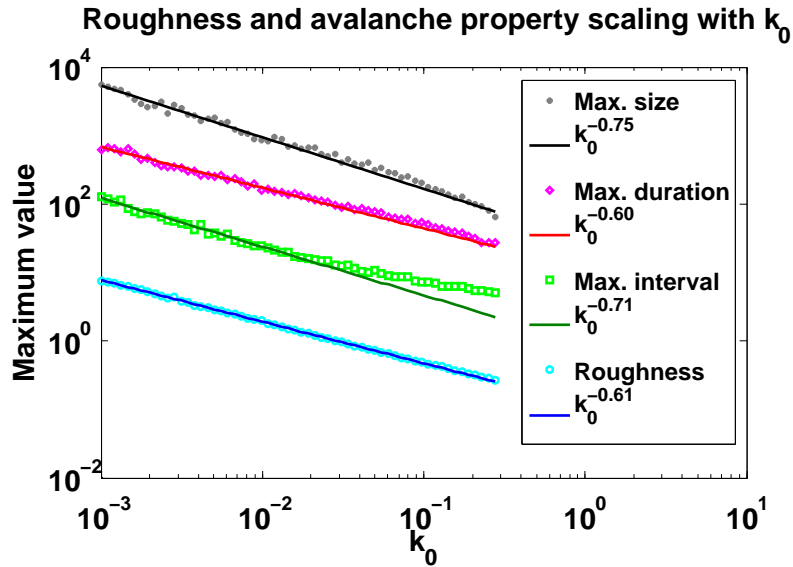


Figure 17: The scaling of roughness and maximum avalanche sizes, durations and intervals as a function of the driving spring stiffness  $k_0$  for the perpendicular chain. The values are scaled so that they're easily distinguishable.

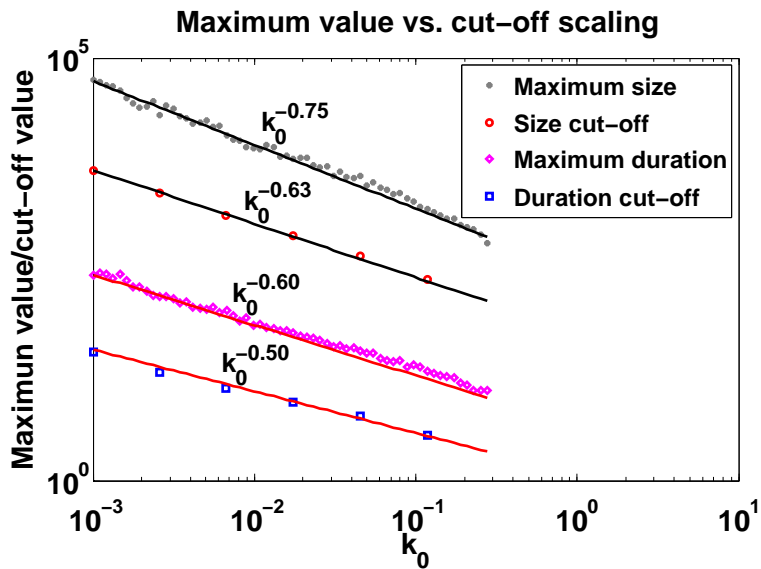


Figure 18: The scaling of the avalanche maximum size and durations compared to the respective cut-off values of the perpendicular chain, obtained by fitting an exponential function to the end of the distribution. There seems to be a slight difference in the scaling exponents.

From the power law fits made with Matlab and Eqs. (3.7) and (3.11), values for the roughness exponent  $\zeta$  and dynamic exponent  $z$  were found to be

$$\zeta = 1.22 \pm 0.09 \quad \text{and} \quad z = 0.98 \pm 0.14.$$

Similar values for the roughness exponent have been found in various 1D depinning models [39, 49–51]. However, in most sources where the roughness exponent was comparable to the above, the dynamic exponents were larger, usually 1.4 – 2.0.

The size, duration and interval distributions computed with the control parameter values in Table 6.3 are shown in Figs. 19, 20 and 21 along with their critical exponents. The distributions are averaged over 300 simulations, with a total of 90 000 slips. The curve fitted to the size and duration distributions is a power law with a "stretched exponential" cut-off:

$$f(x) = x^{-\alpha} e^{-(\frac{x}{\beta})^\gamma}, \quad (6.1)$$

in which the fitting parameter  $\alpha$  corresponds to the critical exponent of the power law part ( $\tau_S$  for size and  $\tau_T$  for duration),  $\beta$  is the cut-off ( $S_0$  and  $T_0$ ) and  $\gamma$  determines the steepness of the cut-off, with higher values expressing steeper cut-offs. The function was fitted with a nonlinear least squares fit using inverse variance weighting, where the variance was calculated between the different simulations. The variance decreases with larger slips, so the weights favor the end of the distribution. The function was fitted to the distribution obtained with the lowest value of  $k_0$ , since it had the longest power law.

In all distributions, varying  $k_0$  affected the cut-off, which was expected at sufficiently low velocities [39]. In the size and duration distributions, however, the critical exponents also seem to become a bit larger with lower  $k_0$ .



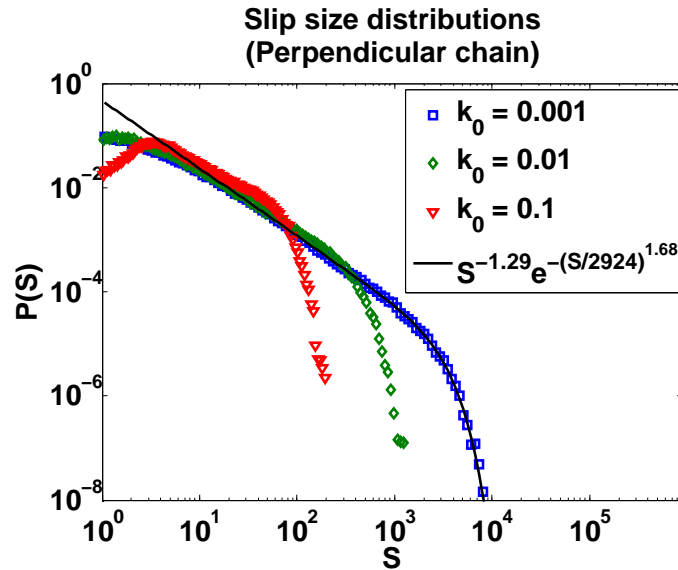


Figure 19: The slip size distributions for perpendicular driving, averaged over 90 000 events. The number of small events drops with high  $k_0$ , likely due to concurrent slips despite pausing the driving while slipping. The distribution conforms to the fitted function mostly after  $S \approx 10$ .

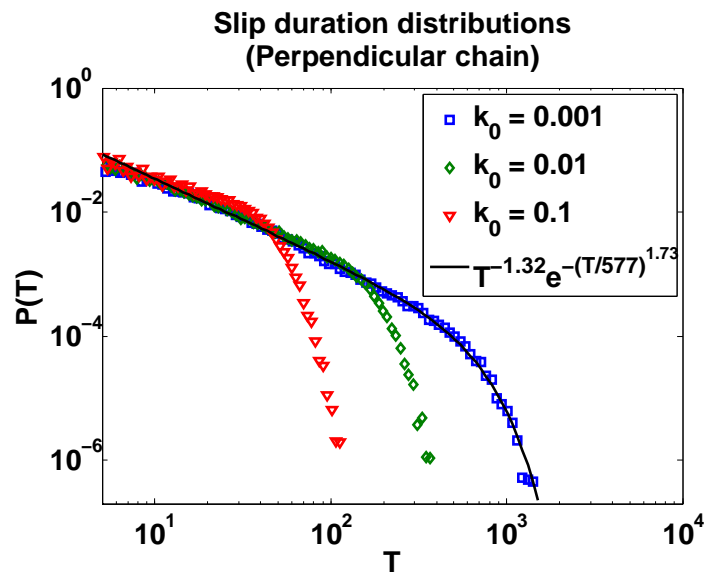


Figure 20: The slip duration distributions, similarly organized as in Fig. 19. It would seem that the cut-off is a bit sharper in the duration distributions.

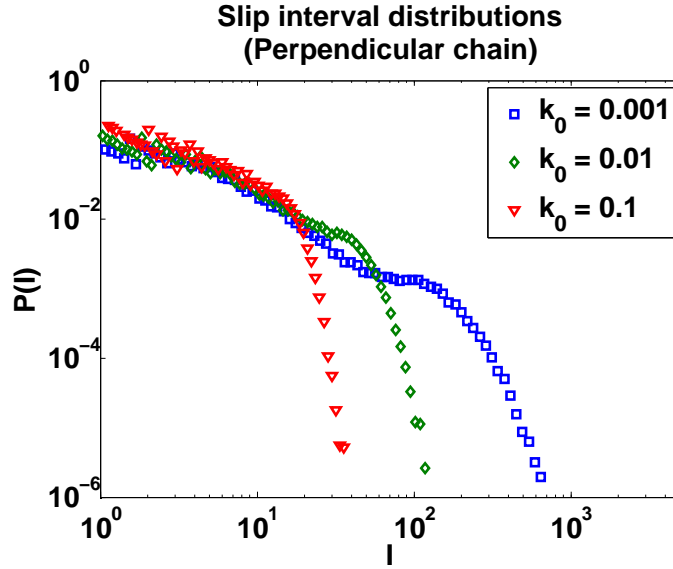


Figure 21: The slip interval distributions of the perpendicularly driven chain. The interval resemble power laws only marginally, and hence no fit was attempted.

The critical exponents found with these parameters are

$$\tau_S = 1.29 \pm 0.12 \quad \text{and} \quad \tau_T = 1.32 \pm 0.13.$$

The errors were approximated by taking a variable amount of points of the distribution to the fitting and observing how the exponents and cut-offs changed. The size and duration distributions are slightly curved, especially at smaller slips, and thus fitting the power law with more points from the small slips yielded lower exponents. The interval distribution did not necessarily have a well-defined linear part in the log-log plot, and thus characterizing it as a power law distribution is dubious. The values obtained for the size and duration exponent correspond quite well to results found in literature [5, 39, 52].

The scaling relations from Chapter 3 can also be used to predict values for the avalanche size and duration critical exponents. Based on the exponents  $\zeta$  and  $z$  and the dimensionality of the system, Eqs. (3.14) and (3.18) give exponents

$$\tau_S = 2 - \frac{2}{d + \zeta} = 2 - \frac{2}{1 + 1.22} \approx 1.10 \pm 0.04$$

$$\tau_T = 1 + \frac{d + \zeta - 2}{z} = 1 + \frac{1 + 1.22 - 2}{0.98} \approx 1.22 \pm 0.14.$$

The exponents attained from the perpendicularly driven simulations with these parameter values correspond within errors to the theoretical predictions, though the size exponent is a bit high. Compared to experiments, the exponents do not match; a fact that has been noted in articles dealing with this kind of minimalistic simulations of frictional stick-slip motion [14, 53]. A relatively recent pin-on-disc experiment with aluminum and steel reports as high size distribution exponents as 2.83 – 3.33 [23].

## 6.2 The vanilla model with parallel driving

With perpendicular driving, the slips are always chaotic, since each particle has its own unique potential surface. In the parallelly driven chain, all the particles see the same potential to an extent, the movement will eventually become semi-regular and periodic if the system is underdamped and large relative to the amount of particles slipping at once, i.e. finite-size effects are not present. The period of the motion depends on the density of potential wells compared to chain length, which is controlled by the equilibrium distance between particles. Two distinct types of parallel chain were identified in the simulations: a chain with many potential wells between individual particles (large equilibrium distance, for example 20), from here on referred to as the *sparse* chain, and a chain with few wells between particles or even multiple particles in the same well (requires small equilibrium distance, e.g. 1), dubbed *dense* chain. The motion and avalanche statistics of the two chains have considerable differences.

For example, with the same parameters that were used in perpendicular driving (Table 6.4) and a dense chain, the motion of the chain is almost continuous (particles slip frequently) and very regular as is seen in Fig. 22. Disregarding the regularity, the behaviour is otherwise similar to the perpendicular case: with large  $k_0$ , the driving spring dominates over the nearest neighbor springs, increasing the amount of small independent slips.

Table 6.4: The parameters used in the onset of motion simulations for the dense parallel chain.

Control parameter	Value
Driving velocity $V$	0.005, 0.05
Driving spring stiffness $k_0$	0.1, 0.01, 0.001
Particle equilibrium distance $d$	1

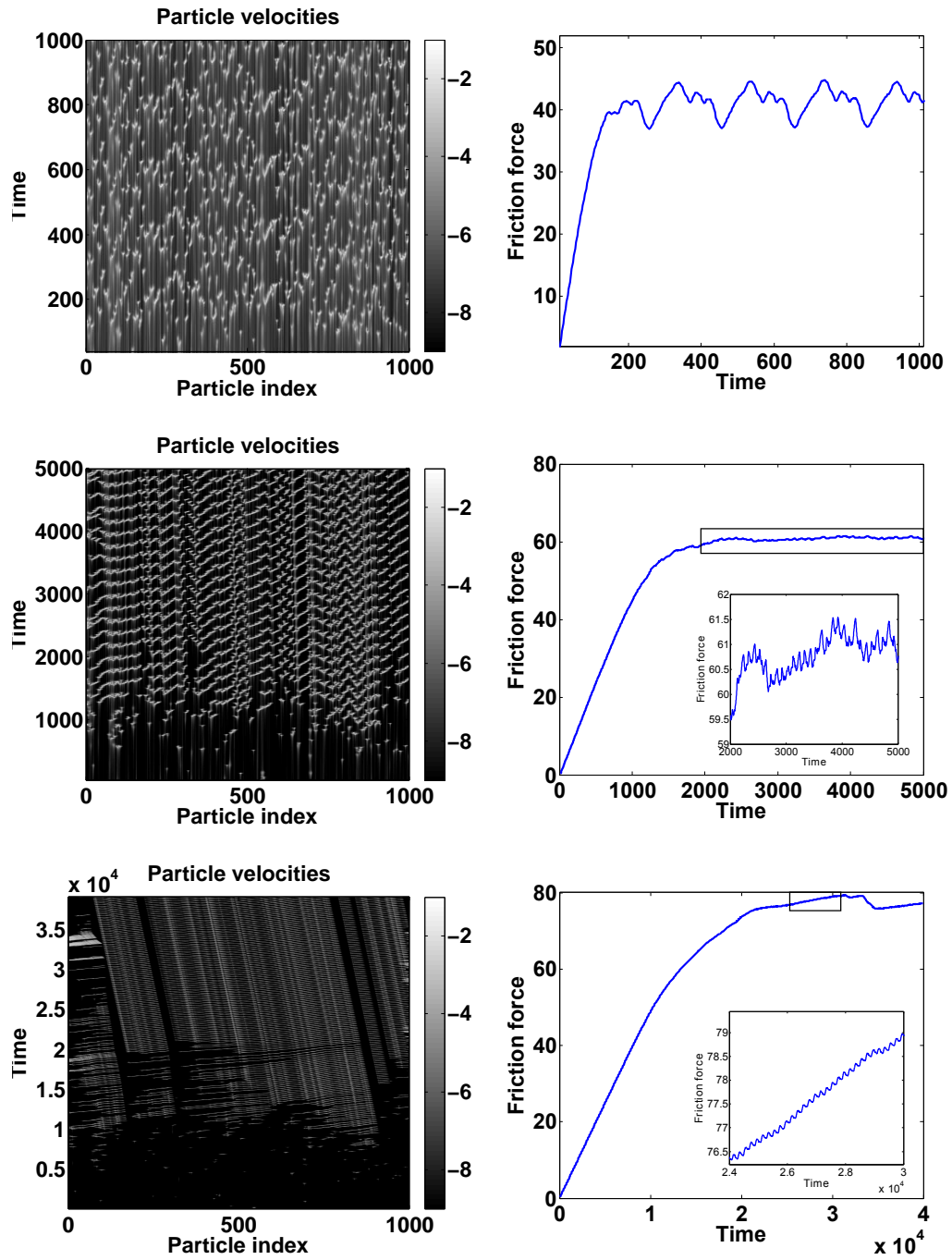


Figure 22: The onset of motion with parallel driving and a dense chain. As in the perpendicular case, the values for  $k_0$  from top to bottom are 0.1, 0.01 and 0.001, respectively, and the velocity values are displayed in logarithmic scale for better viewability. The insets show the small fluctuations of the friction force.

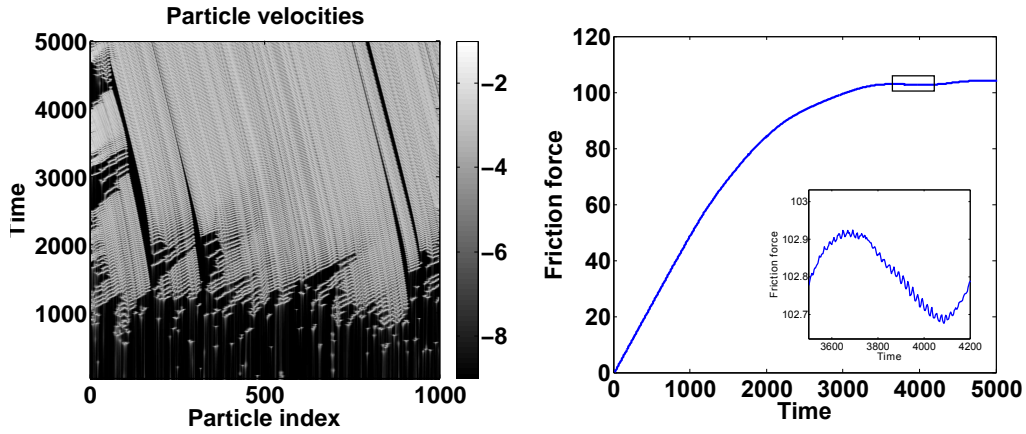


Figure 23: The smooth sliding due to increase in the driving velocity ( $V = 0.05$  in this case) for the dense parallelly driven chain. Like in the perpendicular chain, the total friction force is increased, and the fluctuations become smaller.

An increase in driving velocity also has an effect comparable to what was seen with perpendicular driving: the time between avalanches becomes very small or nonexistent (Fig. 23), and velocity strengthening is observed.

In this parameter regime, a couple of dissimilarities to the perpendicular case can be noted: new avalanches start before others are exhausted even with low  $k_0$ , leading to smoother motion, and the slips seem to propagate more eagerly to the driving direction (in the perpendicular chain, the propagation was roughly equal in both directions). Both of these are related to the property unique to the parallel chain: two or more particles can occupy the same potential well, forming a local compression (kink) in the chain, provided the well is deep and wide enough. This leaves an extension (antikink) of the chain in some other location. The dynamics of kinks and antikinks change how particles slip in and out of the wells in the parallel chain.

### 6.2.1 Kinks and the particle equilibrium distance

When the chain is let relax on the potential surface, kinks and antikinks can form in various locations. Though any compression can be counted as a kink, the most visible effects on the slip propagation is seen when the equilibrium distance is small enough to have multiple particles occupy the same potential well. The kinks and antikinks are good start points for an avalanche, since they are somewhat unstable: the nearest neighbor interactions push/pull the nearest particles in addition to the driving spring, so they leave their

potential wells easily. When the particle slips to a new potential well, its neighbor might then jump to the next potential well due to the relaxed nearest neighbor interaction, causing the next particle to jump and so forth, moving the kink along the chain. Finally some particle either reaches a potential well deep and wide enough to contain multiple particles for an extended amount of time, trapping the kink, or the kink reaches the end of the chain, moving the particle on the boundary forward and thus disappearing. An example of the kink behaviour is illustrated in Fig. 24.

An antikink is also sent backwards through the chain, though if the starting location of the slip was a kink (which it usually is), the chain relaxes, and the antikink propagation is not seen. The size and velocity of the kink are determined by the interparticle spring stiffness and the equilibrium distance: with a low stiffness (or small distance), the particles can more easily occupy the same potential well and the kinks are localized, whereas high stiffness (or large distance) requires more movement from the neighboring particles to allow a slip, widening the compression but at the same time making it move (and thus disappear) faster.

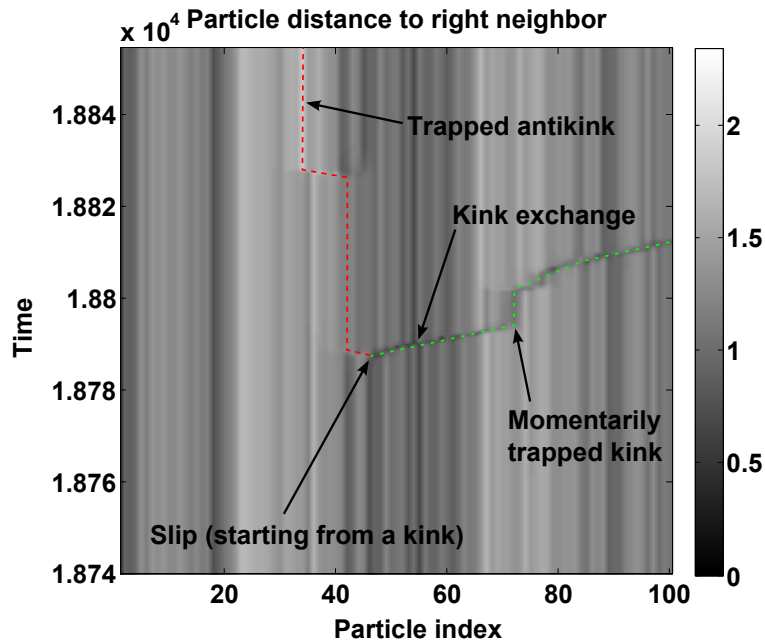


Figure 24: Kink and antikink propagation and trapping in a chain of 100 particles. The picture depicts the distance of neighboring particle pairs: lighter colors mean that the distance is larger, while darker colors indicate shorter distance. A moving kink (antikink) is highlighted by the green (red) dashed line.

When a kink encounters an antikink, they annihilate and the chain relaxes at that location. There's also a possibility of a moving kink encountering a well with more than one particle, i.e. another (more stable) kink. In this case, typically a "kink exchange" happens: if the potential well is not deep enough to accommodate more particles at the time, the first particle "in line" is pushed out when the last enters the well. Similar kink configurations (though with an underdamped chain) are noted in Ref. [54] and appropriately dubbed "traffic jams". This explains the type of onset of motion seen in the previous subsection: the steady state slips consist of single kinks leaving the deepest wells and moving through the system. The period is small due to the forwardmost particles in each deep well having a relatively small energy barrier (the *Peierls-Nabarro barrier* [36]) to overcome in order to leave the well.

When the equilibrium distance is increased, the period of the motion also grows. The reason for this is twofold: Firstly, the particles have to travel a larger distance in order to end up in the same configuration (or almost the same configuration, since the boundaries are shifted forward equal to the equilibrium distance) as in the beginning. Thus the slips in between the initial configuration and shifted configuration contribute to the length of the period. Secondly, small equilibrium distances allow particles to be in the same well without the repulsive force from interparticle springs growing too large, but larger equilibrium distances prohibit this. Since there aren't traffic jams in the same well to diminish the backward propagation of the avalanche, the avalanche advances in both forwards in the driving direction and backwards. Dense and sparse chains atop a potential surface are shown in Fig. 25, and the effect of increasing equilibrium distance on the onset of motion and avalanche size distribution is shown in Fig. 26.

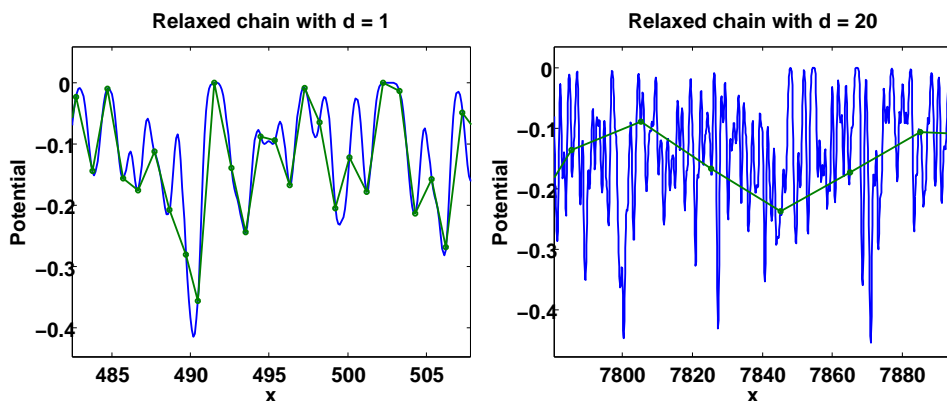


Figure 25: Parts of a dense (left) and sparse (right) chains relaxed on potential surface.

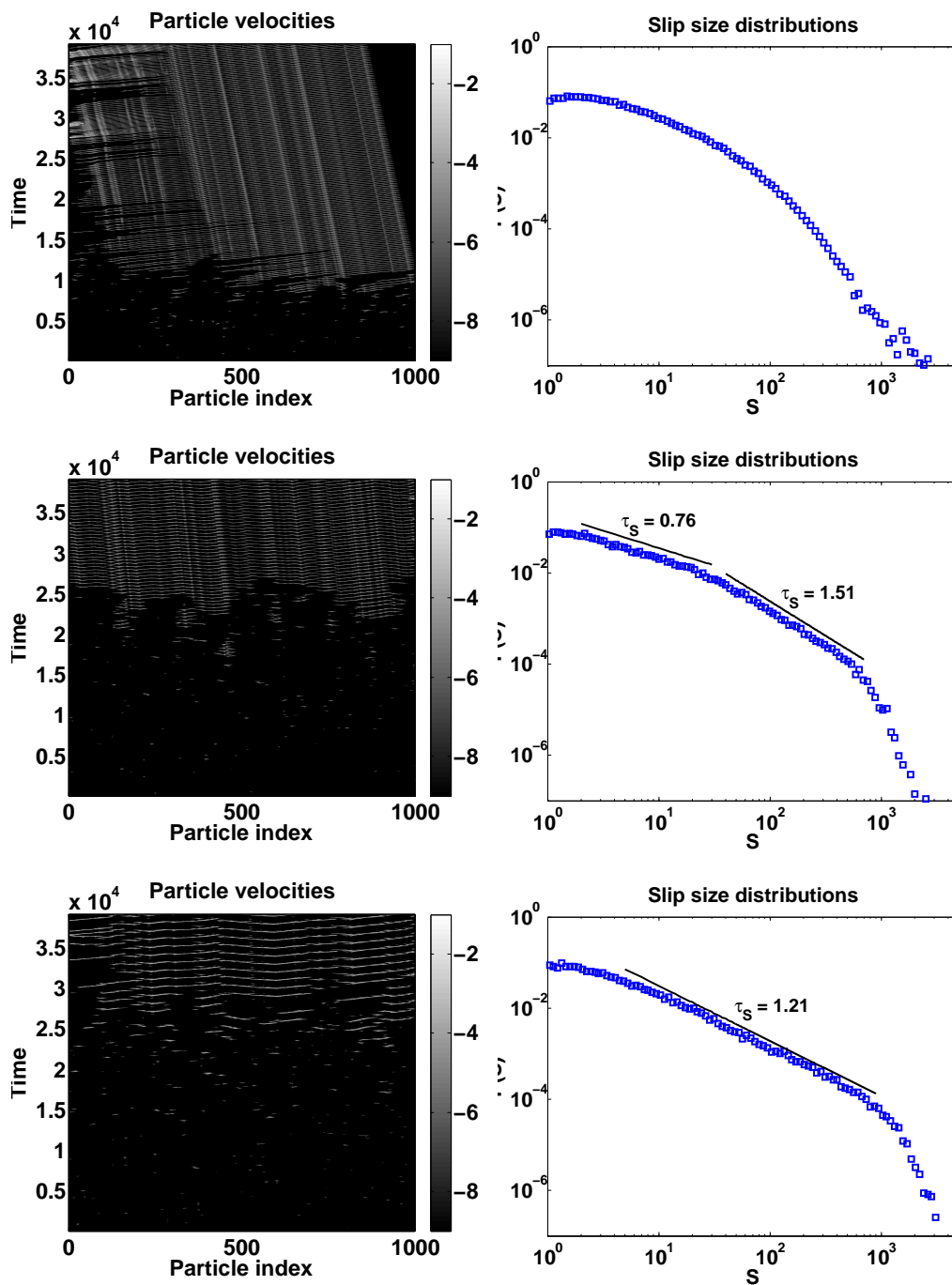


Figure 26: The onset of motion with 1000 particles with equilibrium distances 1 (top), 2 (middle) and 5 (bottom) and their corresponding slip size distributions.



Due to the particles not aggregating in the same wells with higher equilibrium distance  $d$ , the driving required to cause slips is increased, and thus the steady state is pushed further away in time. The avalanche size distribution behaves curiously when  $d$  is increased: at  $d = 1$ , the distribution doesn't seem to have a well-defined power law part or cut-off. Increasing  $d$ , two power laws appear, one with a low  $\tau_S$  and one with high  $\tau_S$ . There's also a clearer cut-off. As the equilibrium distance still increases, the two power laws seem to merge into one with a critical exponent between the two values, leaning towards the higher one.

### 6.2.2 Precursory avalanches

Both parallel and perpendicular driving display small avalanches after the driving has begun but before reaching the steady state. In the parallel chain, these can possibly be identified with the precursors to stick-slip motion found in the experiment of Ref. [32], which are similar kind of small slips inside the material that cause drops in the measured friction force even before the actual steady-state stick-slip motion starts. This behaviour is depicted in Fig. 27 for a sparse parallel chain of 200 particles. The shorter chain was used to be able to better observe the precursors; the transition to steady state is quite smooth with a large chain because of the aforementioned uniform driving and the system size: some parts of the system can slip independently and getting closer to criticality increase the amount of these slips. Consequently, the number of force drops increase while the force keeps growing in other parts of the chain, leading to a smoother transition.

It should be noted that the simulation differs from the experiment in that the driving slab used in the simulation is effectively infinitely rigid, and the notion of "height" in the 1D case is irrelevant. Thus the simulated interface is not pushed from the trailing edge like in the experiment, but each particle is driven forward uniformly. Therefore the precursor slips are not necessarily created at the trailing edge, but can start from anywhere in the system. Additionally, the small slips are present even in the steady state if the chain is not too rigid. In a rigid chain, the steady state consists mostly of the whole chain slipping at once and the small slips are absent (Appendix B), but the precursory slips still show up in the beginning and the overall stick-slip motion in this case resembles the experiment more closely.

A good numerical study on precursor events can be found in Ref. [26]. It is pointed out that with uniform loading, the precursors should be absent, at least in systems with long range interactions. However, in disordered systems with short range interactions, the precursory slips are expected to occur.

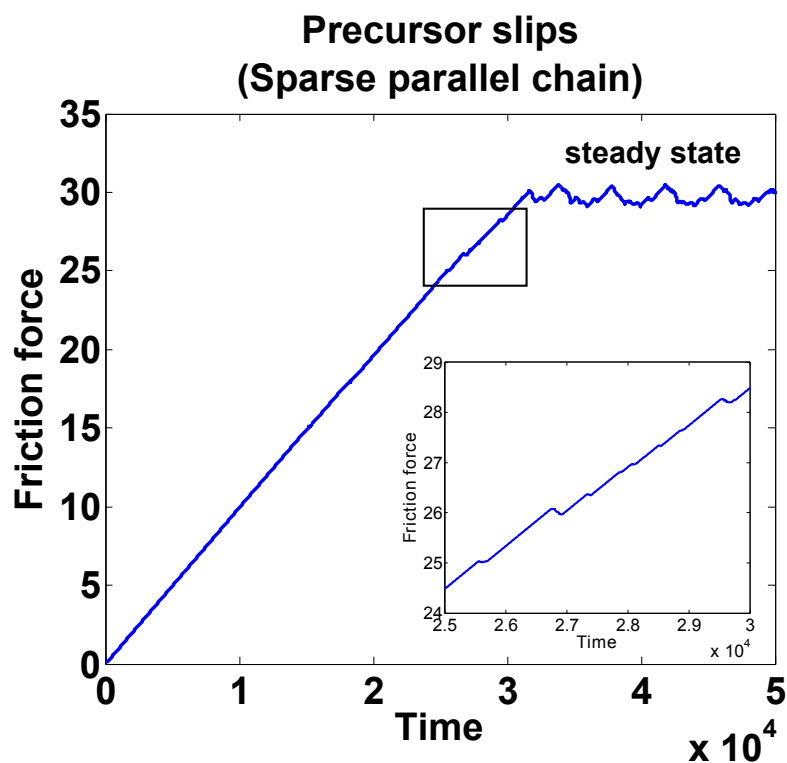


Figure 27: The precursor slips can be seen as a drop in the friction force when the loading is increased. The chain used here was a parallel sparse chain consisting of 200 particles. The three larger precursors and some smaller ones are shown in the inset.

### 6.2.3 Avalanche statistics

The equilibrium distance of particles influences not only the onset of motion, but also the avalanche statistics. Using the control parameter values in Table 6.5 (same as in the perpendicular driving case) separately for the sparse and dense chains, quite different statistics were obtained. The dense chain (equilibrium distance 1), where the avalanches are mostly kinks traversing between "traffic jams" as seen in the initial onset of motion simulations, the distributions tend to be more curved and the cut-offs are smaller. For the sparse chain (equilibrium distance 20), the dynamics resemble those of the perpendicular chain, with large portions of the chain slipping at once. In either case, the movement becomes periodic in the steady state, with only small variations.

Table 6.5: The control parameter values used when running the avalanche distribution simulations for parallel chain.

Control parameter	Value
Driving velocity $V$	0.005
Driving spring constant $k_0$	0.1, 0.01, 0.001
Driving paused while slipping	True
Slip characterization method	Velocity threshold
Relaxation velocity threshold	0.05
Particle equilibrium distance $d$	1, 20

The scalings of roughness and maximum avalanche distribution values with  $k_0$  for both chains are shown in Fig. 28. The scalings were quite similar in both parallelly and perpendicularly driven systems. Curiously, with the dense chain the scaling of maximum size and duration are closer to the perpendicular case, even though the observed onset of motion was considerably different. However, the roughness and interval scaling differ considerably. By contrast, the sparse chain had somewhat different scaling in the maximum size and duration but intervals and roughness closer to the perpendicular chain.

In the dense chain, the values for the dynamic exponent could not be determined like in the perpendicular case (i.e. from the accurate cut-off values), since the exponential fits did not yield cut-offs that would show sensible power law scaling (Fig. 29). Thus, the dynamic exponent was instead determined by the scaling of the maximum duration. The exponents for the dense chain measured this way were

$$\zeta = 1.45 \pm 0.21 \quad \text{and} \quad z = 1.22 \pm 0.08.$$

With the sparse chain, the roughness scaling with  $k_0$  is much smoother, and the roughness exponent and the dynamic exponent are closer to that of the perpendicular chain. The cut-off values also display power law scaling better in this case (Fig. 30), yielding exponents

$$\zeta = 1.29 \pm 0.11 \quad \text{and} \quad z = 1.02 \pm 0.18.$$

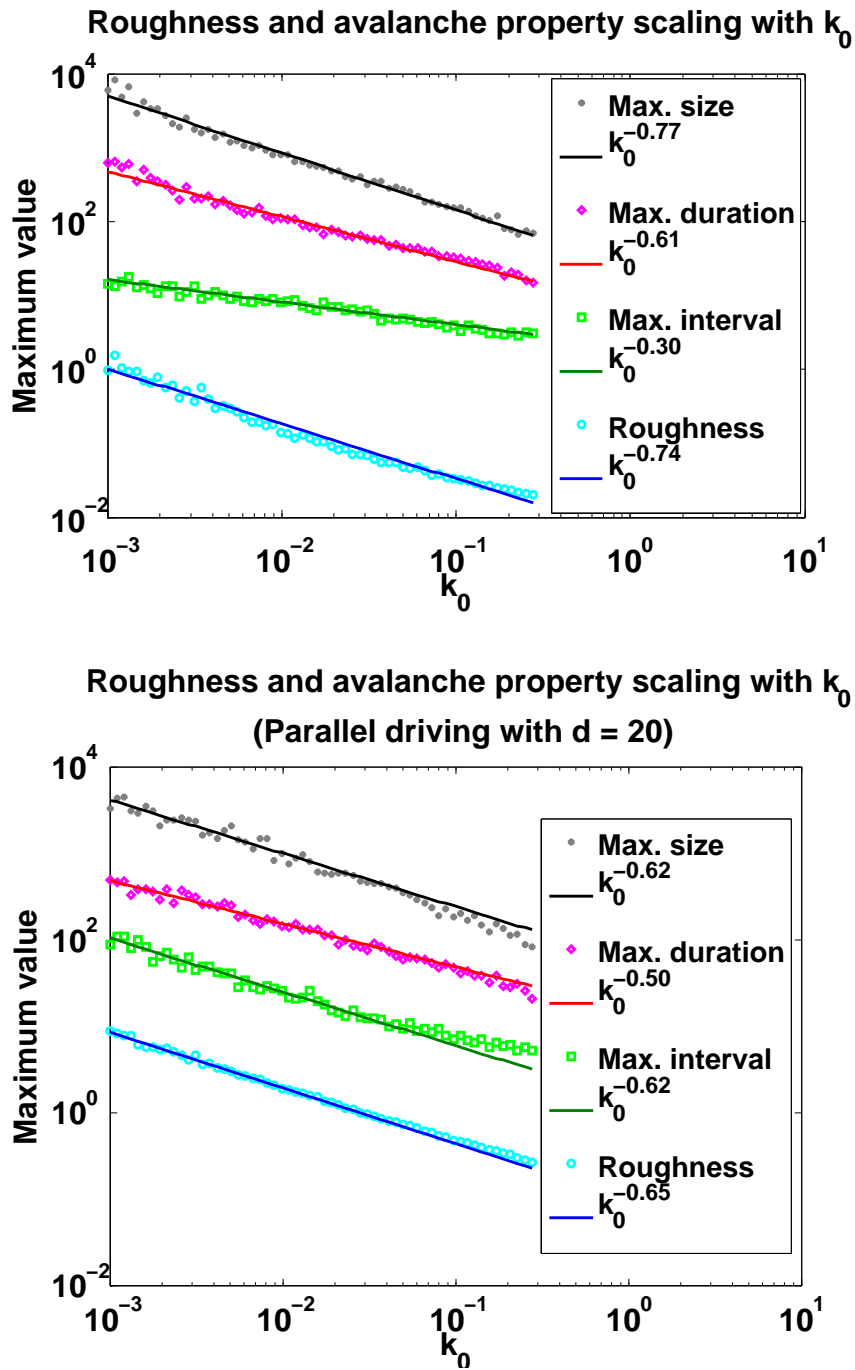


Figure 28: The scaling of roughness and maximum interval as a function of  $k_0$  with a dense parallelly driven chain yields values different from the perpendicular driving case (top). With a sparse chain (bottom), the values are closer to those of the perpendicular chain, but the size and duration scalings are seemingly different.

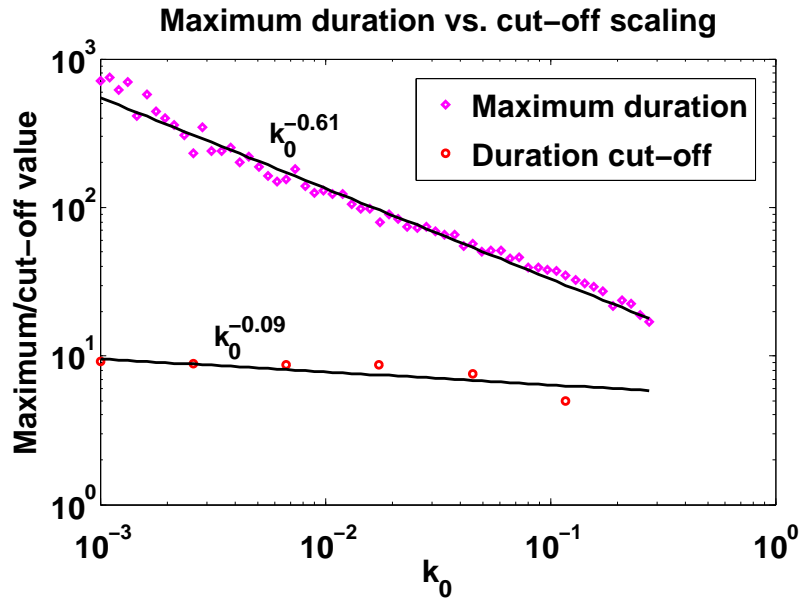


Figure 29: With equilibrium distance 1, the cut-off values do not lie up neatly in a line, and thus the scaling with  $k_0$  is unclear, even though the maximum value shows a power lawish scaling.

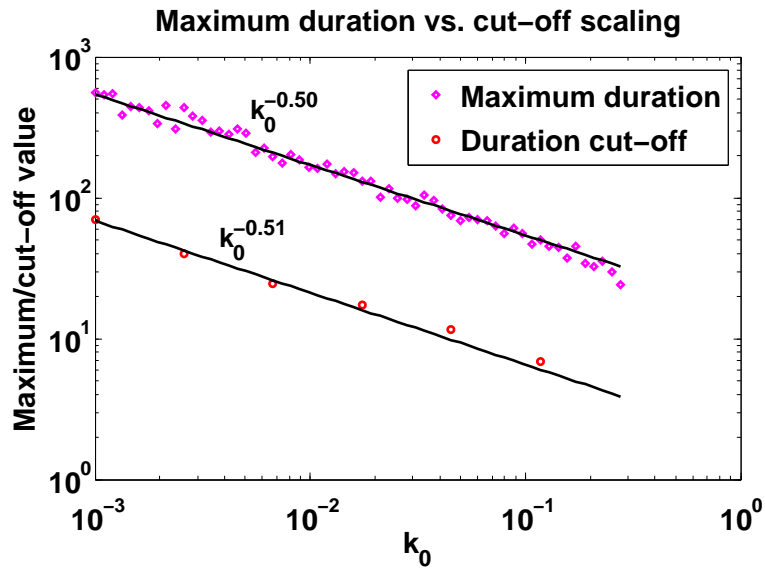


Figure 30: For equilibrium distance 20, the cut-off values scaled comparably to the maximum values.

In the dense chain, the fluid kink-propagating motion does not resemble avalanches and thus cannot be well characterized with the correlation length and roughness as defined in Chapter 3. This, and possibly concurrent motion of the kinks in different parts of the chain are likely the cause for the unusual scalings, resulting in roughness and dynamic exponents clearly distinct from the perpendicular or sparse parallel chain. This effect is lessened for larger values of  $k_0$ , since the stiffness of the driving springs somewhat prevent the aggregation of particles in the same wells. As a result, distributions somewhat reminiscent to power laws with exponential cut-offs were obtained for large values of  $k_0$ . However, due to the short power law part, the critical exponents  $\tau_S$  and  $\tau_T$  are difficult to determine. With lower  $k_0$ , the size and duration distributions of the dense parallel chain corresponds better to an exponential function instead of a power law (Fig. 31).

With the sparse chain and thus increased period and more avalanche-like motion not based on kinks, the power laws in the distributions become more clearly visible (Fig. 32) with all  $k_0$  values and the cut-off behaves as in the perpendicular case, though they might be a bit steeper.

The theoretical predictions based on these values are collected in Table 6.6 along with the actual values measured from the distributions. The values obtained with the sparse chain correspond better to the theoretical predictions, likely due to the motion resembling single avalanches instead of continuous kink propagation. However, the values from both chains compare adequately to similar simulations [5, 39, 52], at least within this parameter regime.

Table 6.6: The critical exponents for dense and sparse parallel chains. For the dense chain, the values are for  $k_0 = 0.1$ .

Exponent	Dense chain	Sparse chain
$\tau_S$ prediction	$1.18 \pm 0.06$	$1.12 \pm 0.04$
$\tau_S$ measured	$1.07 \pm 0.19$	$1.24 \pm 0.11$
$\tau_T$ prediction	$1.37 \pm 0.21$	$1.28 \pm 0.19$
$\tau_T$ measured	$0.92 \pm 0.21$	$1.19 \pm 0.15$

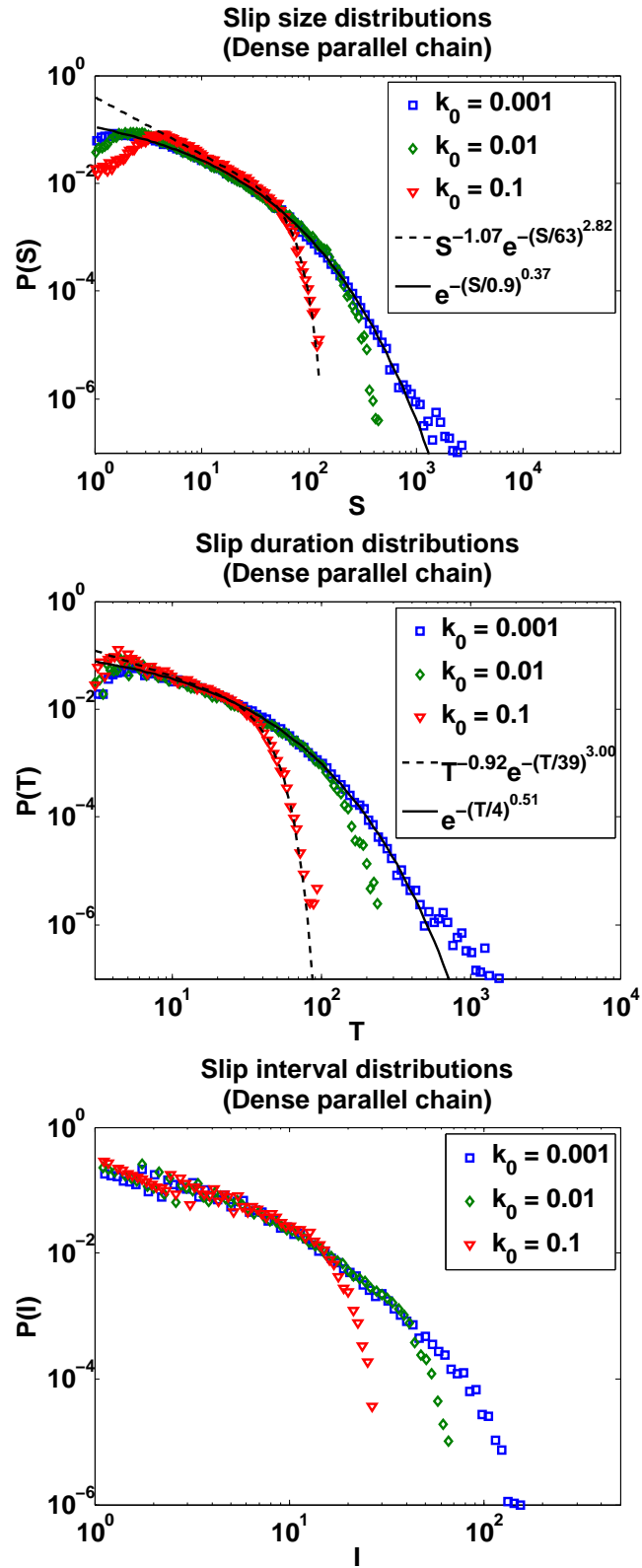


Figure 31: Having an equilibrium distance  $d = 1$  makes it more difficult to determine the linear part of the logarithmic plot for low  $k_0$ , and the cut-off does not behave like in the perpendicular chain.

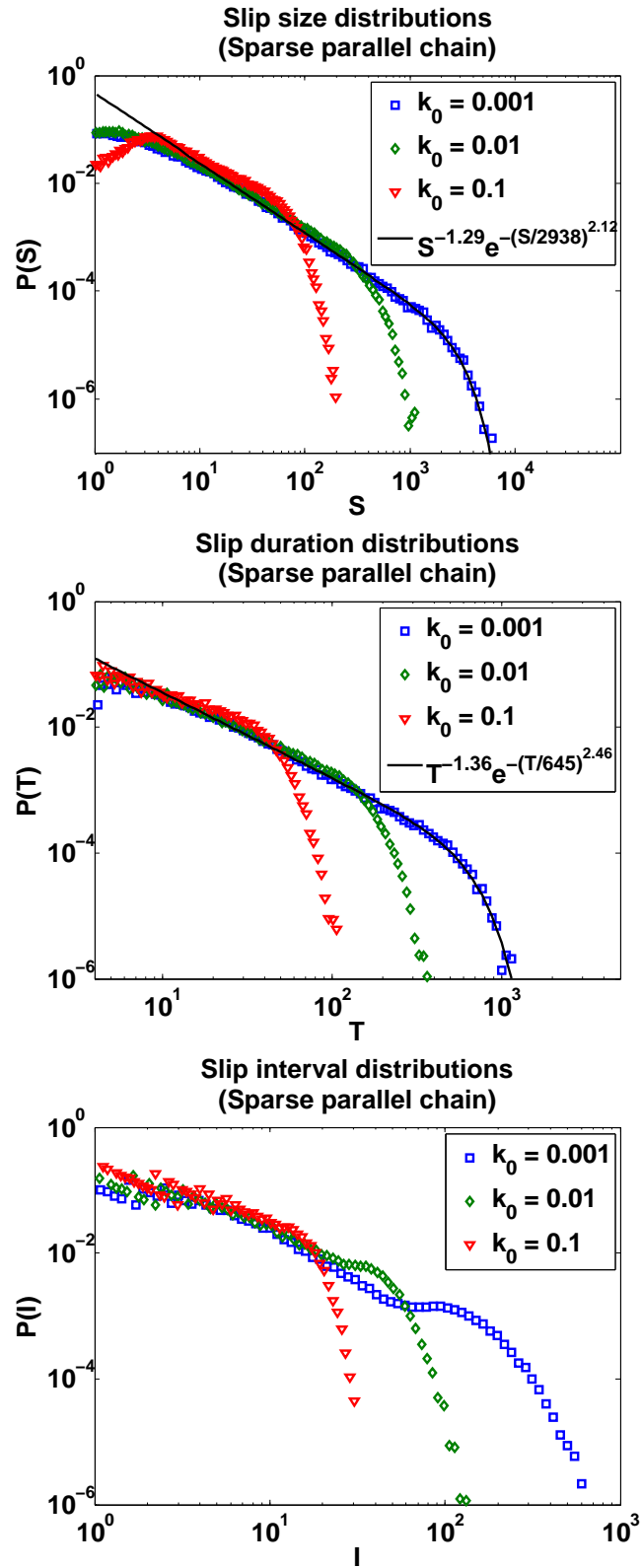


Figure 32: With larger particle equilibrium distance ( $d = 20$ ), the distributions of the parallelly driven chain become similar to the distributions of the perpendicularly driven chain.



## 6.3 Viscoelasticity

The viscoelastic response of the chain depends primarily on the damping coefficient for the dashpots  $\eta_u$ . It determines the timescale of the viscoelastic relaxation: if the relaxation is very fast, the dashpots have little effect and the main change to the model comes from the additional spring. Conversely, if the relaxation is slow, the dashpots won't have time to relax until the external driving triggers a new avalanche. For this reason, an addition was made to the option of pausing driving when slipping: the driving would start only after the dashpots were relaxed, determined by the viscoelastic force falling below certain threshold. This way the relaxation could be slow without new avalanches caused by the driving during relaxation.

The control parameter values for the simulations incorporating viscoelasticity are collected in Table 6.7. It was noticed that the spring stiffness  $k_2$  had very little effect on the dynamics so value  $k_2 = 1$  was used. As was done in the vanilla model simulations, the avalanche distributions are averaged over 300 simulations and 90 000 events.

Table 6.7: The control parameter values for viscoelastic chain.

Control parameter	Value
Driving velocity $V$	0.005
Driving spring constant $k_0$	0.1, 0.01, 0.001
Particle equilibrium distance $d$	1, 20
Dashpot viscosity $\eta_u$	1, 10, 50
Dashpot spring stiffness $k_2$	1
Driving paused while slipping	True
Slip characterization method	Velocity threshold
Relaxation velocity threshold	0.05

### 6.3.1 Perpendicular chain: onset of motion

The onset of motion is not very much affected by the viscoelasticity, at least when viewing the chain as a whole. When examining individual slips, however, a slight change in dynamics can be seen (Fig. 33): due to the viscoelastic relaxation, the particles taking part in a slip don't immediately stop moving after hitting the next potential well. In some cases, the relaxation can push the neighboring particles to initiate a new slip. Additionally, the viscoelasticity makes it possible for a particle to be pushed backwards by the relaxing dashpot, though this effect is not very pronounced.

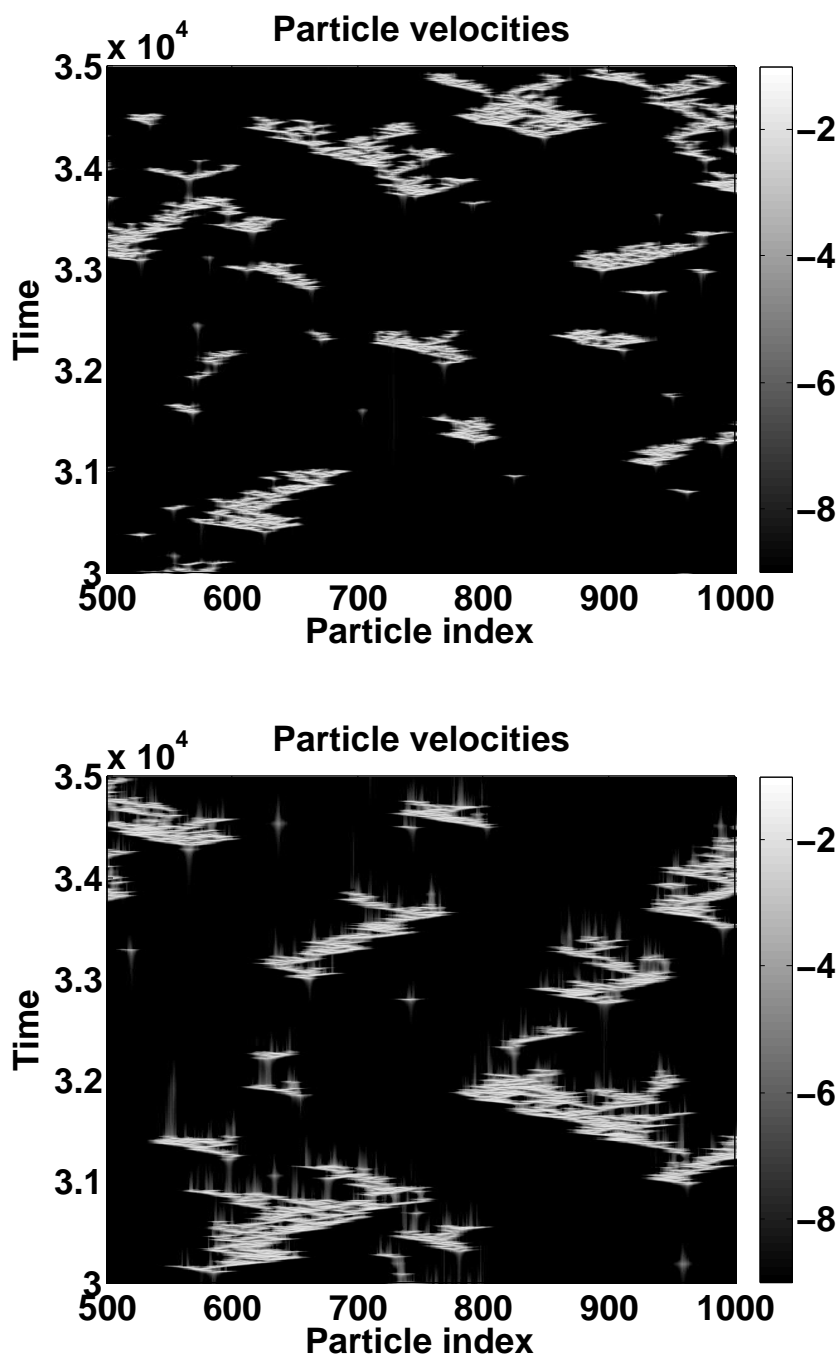


Figure 33: The avalanches of the vanilla FKT model (top) compared to avalanches with the inclusion of viscoelastic effects (bottom), with perpendicularly driven system. The  $\eta_u$  used was 50.

### 6.3.2 Perpendicular chain: avalanche statistics

The consequences of viscoelasticity had a somewhat more visible effect on the avalanche statistics, especially with sufficiently high values for  $\eta_u$ . Fig. 34 shows that the avalanches in viscoelastic model tend to be visibly clustered, unlike in the basic FKT model, where the start times of the avalanches are seemingly random. After a large event in the viscoelastic case, the relaxation of the dashpots can trigger new, usually smaller, events. In Ref. [46], these are identified as aftershocks in the seismic context.

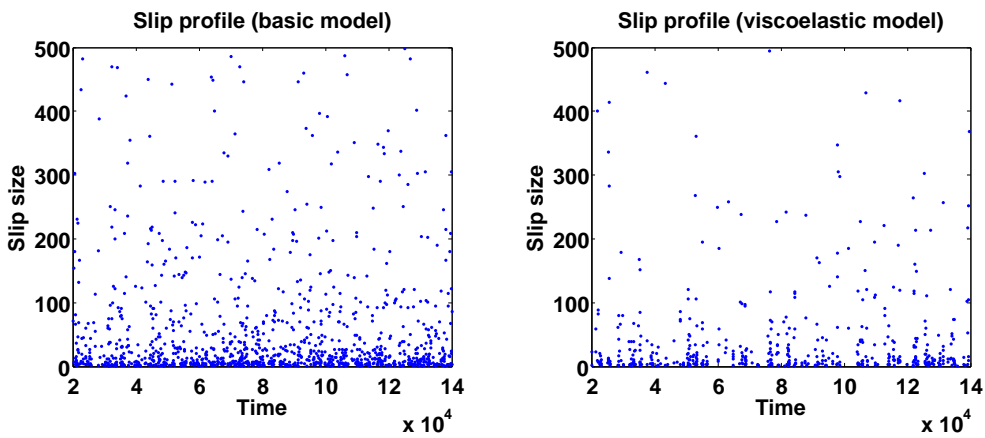


Figure 34: The slip profiles of single runs consisting of 1500 slips show the clustering of avalanches in the viscoelastic model.

In the viscoelastic model, few avalanches are caused by the driving, and most of the avalanches are "relaxation avalanches" (caused by the relaxation of the dashpots). This can be seen as in the avalanche distributions: the size and duration critical exponents in this kind of system are a few tenths higher than in the basic FKT model.

The interval distribution also acquires a power law distribution, with the exponent inversely proportional to the dashpot viscosity. The power law portion most likely represents the intervals between aftershocks induced by the inner relaxations of the chain. This observation is supported by the fact that faster relaxation (smaller  $\eta_u$ ) shortens the power law part.

The avalanche distributions for damping coefficient values  $\eta_u = 10$  and  $\eta_u = 50$  are plotted in Figs. 35, 36 and 37.

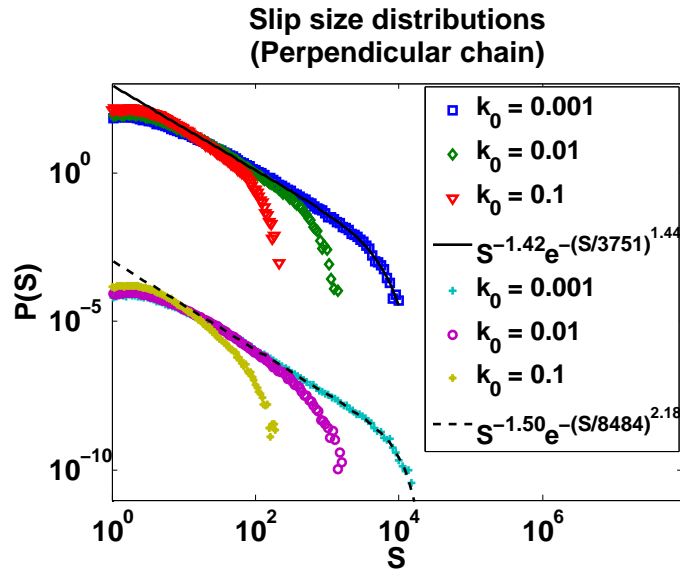


Figure 35: The slip size distributions for perpendicular driving with viscoelasticity. The top three distributions are for  $\eta_u = 10$ , while the bottom three are for  $\eta_u = 50$ . The distributions are scaled so that they don't overlap.

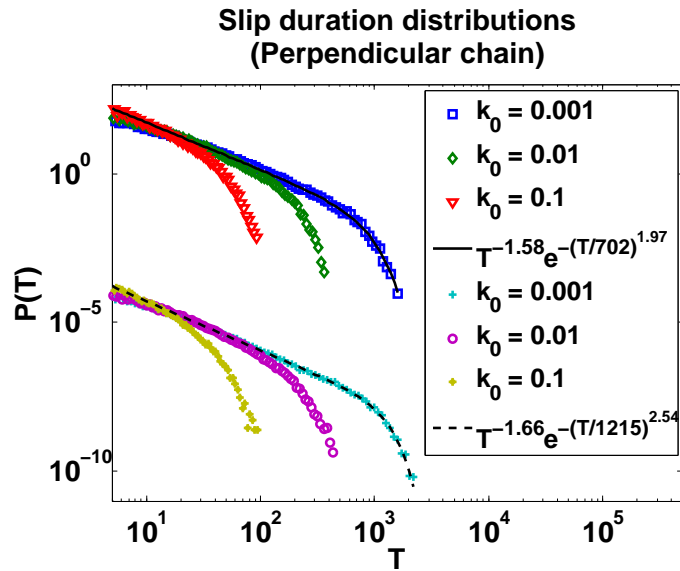


Figure 36: The slip duration distributions (similarly arranged as the size distributions) also display a change in exponent when  $\eta_u$  grows. The cut-off seems to be a bit steeper than in the size distributions, not corresponding as well to the exponential cut-off.

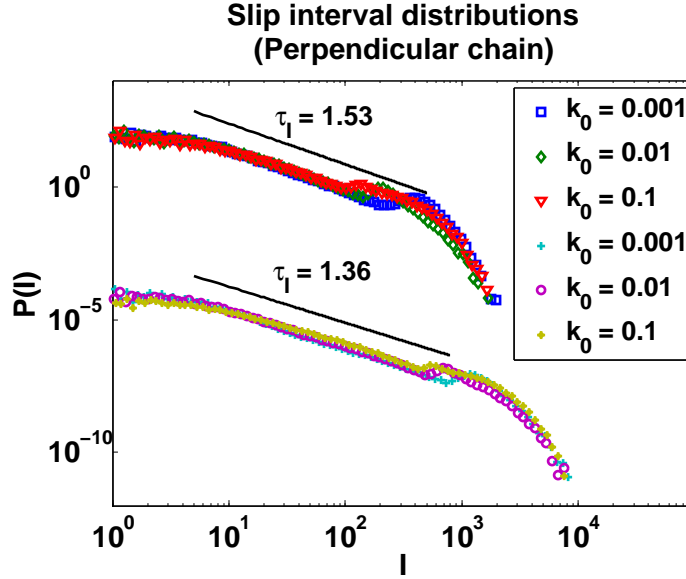


Figure 37: The interval distributions show a power law and a bump at high intervals with the viscoelastic model.

At control parameter value  $\eta_u = 50$ , it would seem that both size and duration exponents experience a roughly 0.2 increase. Since  $\eta_u$  determines how fast the dashpots relax, larger values typically mean greater ratio of relaxation avalanches to avalanches caused by driving (as the dashpots don't relax as much during these slips). Thus the higher value for  $\eta_u$  can be considered to more accurately represent the avalanche distributions of the aftershocks. The increase in avalanche size exponents coincide with results in [46], though the critical exponent change is not as drastic. This might be due to the fact that the simulations in this thesis are performed in only one dimension. The simulations are also continuous in time, meaning the dashpots might still have relaxed somewhat even during the slips caused by driving, resulting in less aftershocks and thus  $\tau_S$  and  $\tau_T$  closer to the basic FKT model. However, having  $\eta_u > 50$  did not have a significant effect on the exponents.

A possible explanation for the increase in exponents is the so-called *avalanche oscillator*: due to the viscoelastic relaxations, the distance from critical force is not stationary in time [55]. Since the cut-off of the size and duration distributions are related to the distance from criticality, the cut-offs and by extension the probability distributions of avalanche sizes and durations oscillate in time. The probability distributions are then sampled from all over the oscillations, leading to a distribution with higher exponents. The value of the driving spring stiffness affected the size and duration distribu-

tions: higher  $k_0$  values had a tendency to skew the distributions towards small slips, further increasing the critical exponents.

A bump appears at the end of the interval distribution after the power law part. The bump is formed due to the intervals between the last after-shocks and a new global slips. This increase in probability happens because the driving is paused when slipping, and the driving continues only after the dashpots have relaxed. Thus even if the relaxation won't cause new after-shocks, the system can stay still for some time before a new global event, seen as the bump in probability for larger intervals. Curiously, the cut-offs of the interval distribution are seemingly independent on  $k_0$  in the viscoelastic case.

### 6.3.3 Parallel chain: onset of motion

The effect of viscoelasticity on the parallel chain is in many ways comparable to the perpendicular chain, at least for the sparse chain (Fig. 38 ). In the onset of motion simulations, the relaxation of the dashpots changed the motion of the sparse chain similarly, i.e. individual slips were slightly larger and the particles don't stop immediately after the slip.

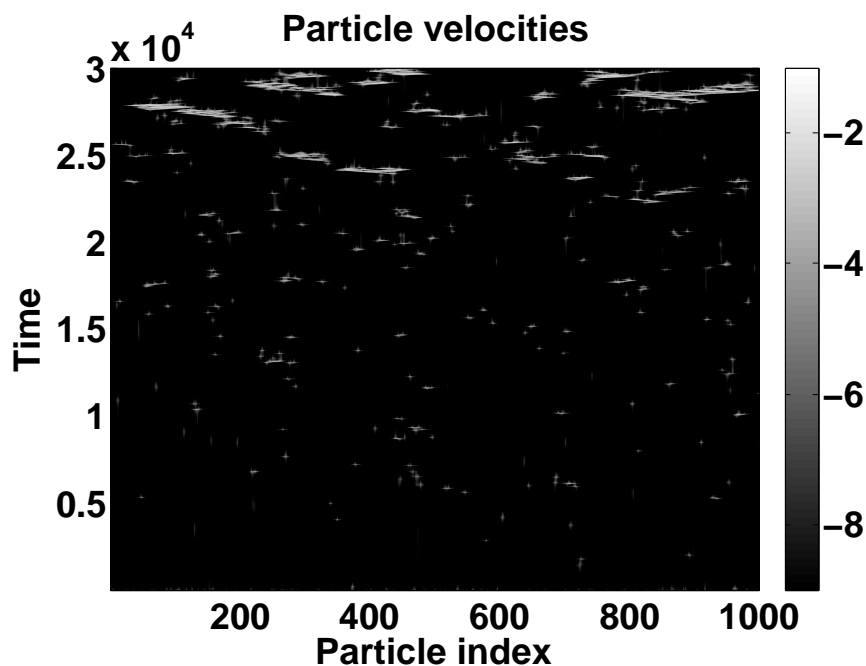


Figure 38: The onset of motion for the sparse chain. Like the perpendicular chain, the relaxation can keep particles moving after the initial slip and cause new slips.

In the sparse and dense parallel chains, the viscoelastic relaxation also served to make the motion a little more chaotic. The general slipping trends are still there, but the movement pattern is not exactly the same for each particle.

In contrast to the perpendicular chain and the sparse parallel chain, where the effects of viscoelasticity are mostly visible when examining individual slips, the dense chain displays differences also at a larger scale (Fig. 39). The period between slips seems to be increased, and larger regions of the chain seem to be moving at the same time than in the dense chain of the basic FKT model. It's likely that in addition to the particles arriving at the traffic jams pushing the forward particles out, the viscoelastic relaxations can also make a particle leave the jam, inducing new avalanches.

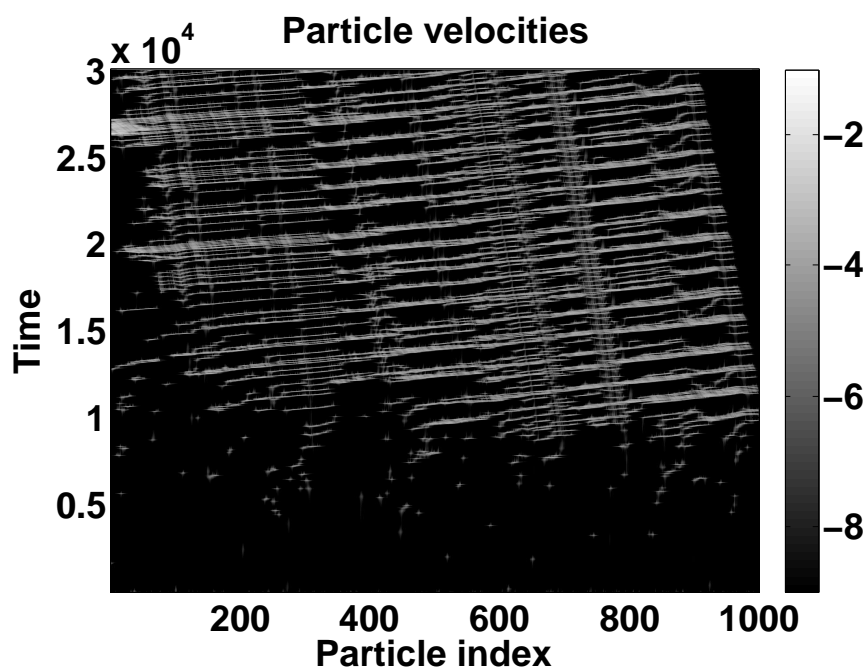


Figure 39: The onset of motion for the dense chain. Compared to the vanilla model, the movement of the chain is considerably different, though still somewhat periodic.

#### 6.3.4 Parallel chain: avalanche statistics

In the presence of viscoelastic effects, the avalanche distributions of the sparse parallel chain behave almost identically to the perpendicular chain (Figs. 40, 41 and 42). The response to change in dashpot viscosity coefficient  $\eta_u$  seems to be a bit weaker, though the effect is within the error limits and thus may just be a result of fitting to slightly different points.

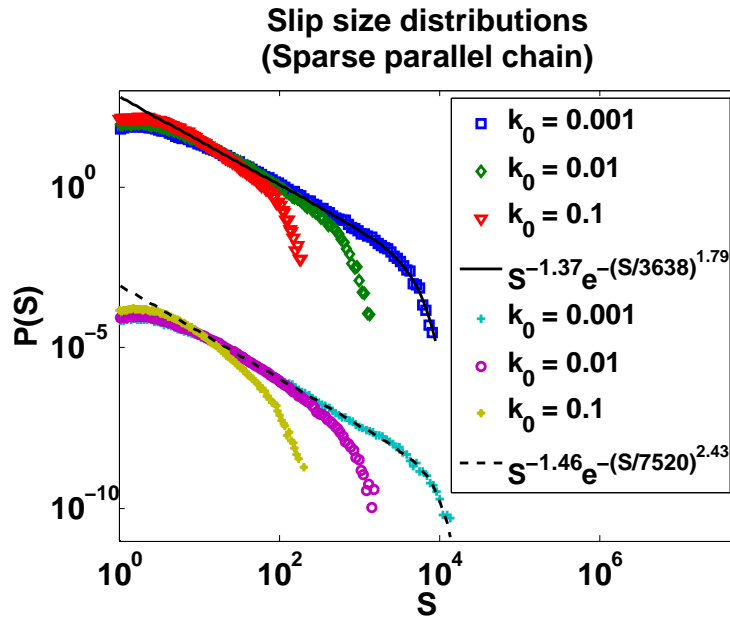


Figure 40: The slip size distributions for  $\eta_u = 10$  (top three distributions) and  $\eta_u = 50$  (bottom three distributions) using parallelly driven, sparse chain with viscoelasticity.

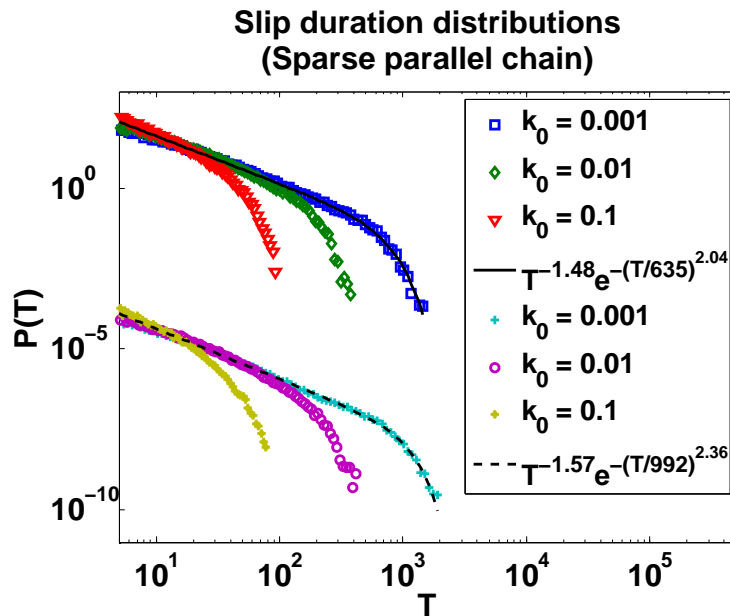


Figure 41: The slip duration distribution of the sparse chain reacts to the increase in  $\eta_u$  much like the perpendicularly driven chain.



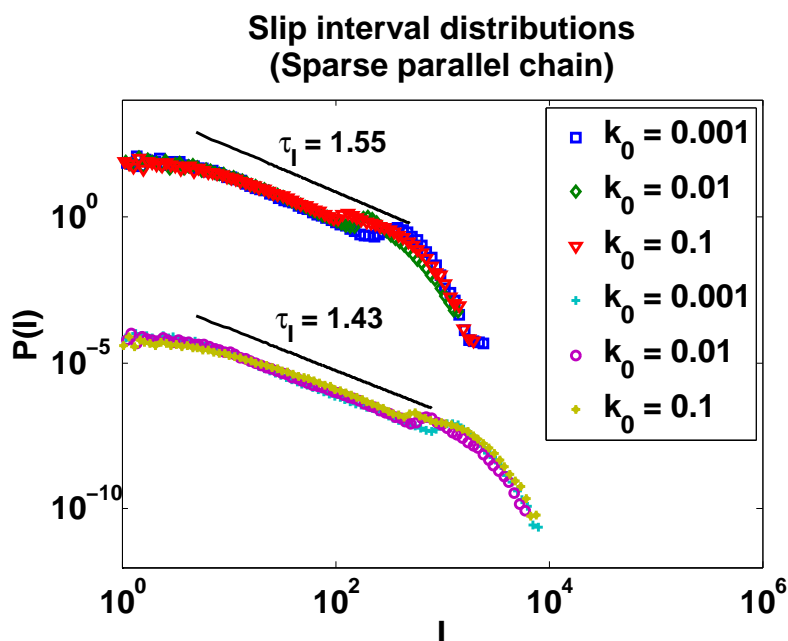


Figure 42: The interval distributions exhibit a power law also in the sparse parallel chain.

The dense parallel chain, on the other hand, has a more interesting reaction to the viscoelasticity. High values for  $k_0$  give distributions with a short power law part and cut-off, but with low  $k_0$ , it would seem that the cut-off of the vanilla FKT model becomes a power law (Figs. 43 and 44). Thus it's hard to find a distinct cut-off in the size and duration distributions. The critical exponents are very high, with size exponents larger than 2 and duration exponents being close to 3. The duration distributions might also have two separate power law parts, a small one in the short slip regime with exponent roughly  $\tau_T \approx 1.80$  and longer where the cut-off was in the basic model with  $\tau_T \approx 2.80$ . The interval distribution displays a power law part like the sparse parallel chain and the perpendicular chain, but the bump in probability near the cut-off is smaller.

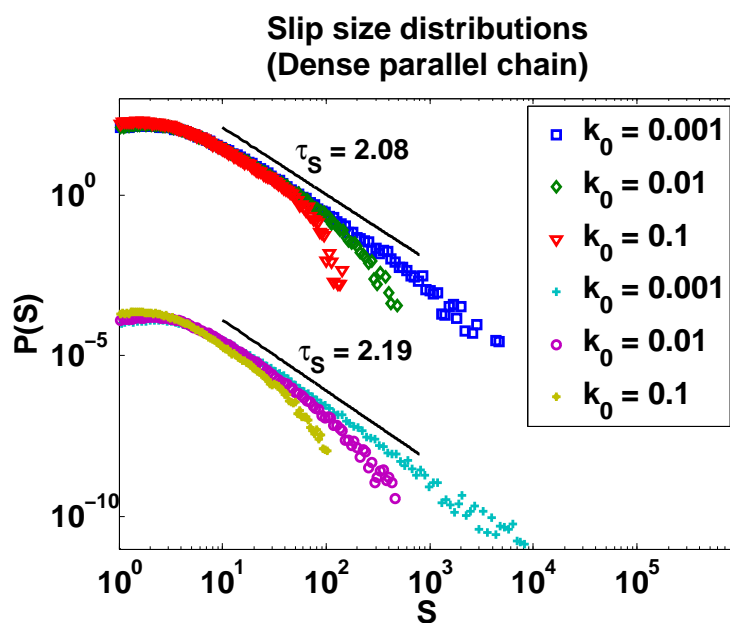


Figure 43: The size distribution of the dense parallel chain is greatly altered by viscoelastic effects. Once again the top three distributions are for  $\eta_u = 10$  and the bottom three for  $\eta_u = 50$ .

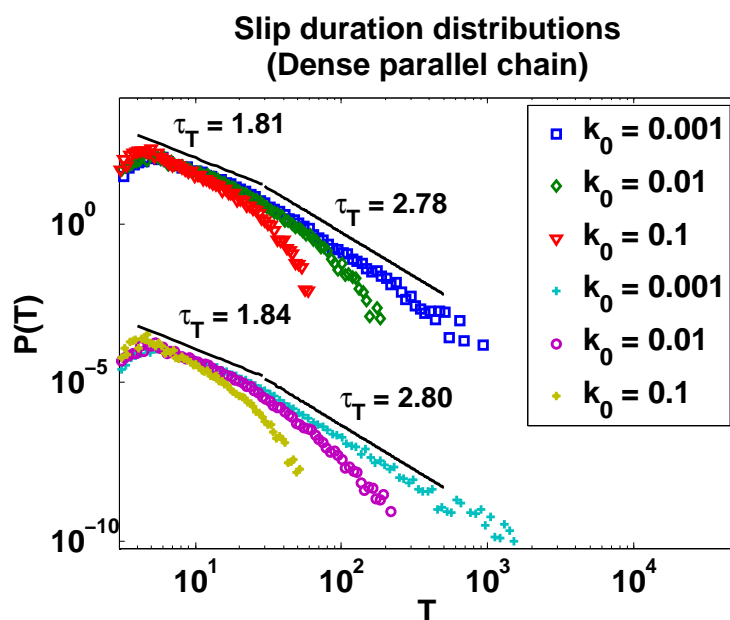


Figure 44: The duration distribution of the dense parallel chain seems to have two power law parts, at least with low values for  $k_0$ .

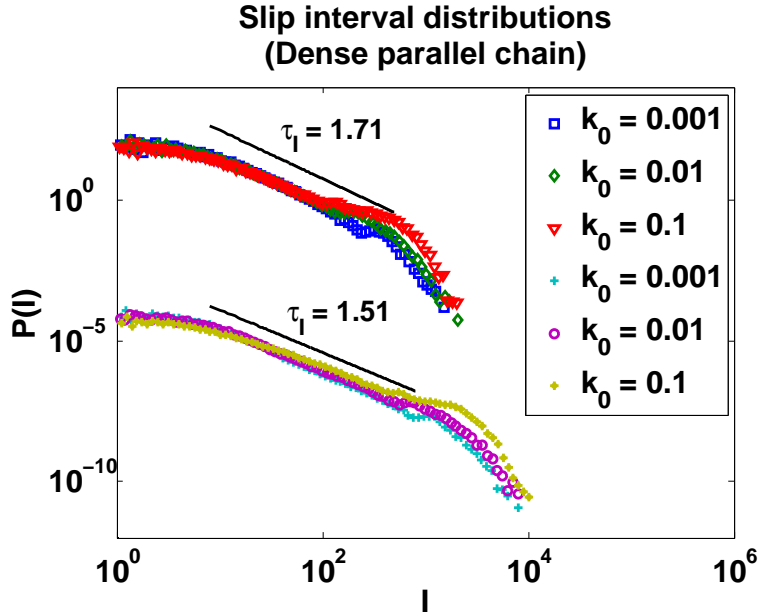


Figure 45: Unlike the perpendicular and sparse parallel chains, the interval exponent of the dense chain seems to depend on  $k_0$ , with lower values giving higher  $\tau_I$ .

Overall, the viscoelasticity affected the slip statistics in both parallel and perpendicular chains in two ways: the aftershock-dominated distributions tended to have higher critical exponents, and the viscoelastic relaxation gave the interval distribution a power law part. The cut-offs of interval distribution of all chains also became more dependent on  $\eta_u$  than  $k_0$ , roughly characterizing the timescale of the viscoelastic relaxation of the whole chain after each global event. The critical exponents along with their estimated errors for all the chains are collected in Table 6.8.

Table 6.8: The critical exponents in the viscoelastic model for the perpendicular chain and the dense and sparse parallel chains. The listed values are for parameter values dashpot viscosity coefficient  $\eta_u = 50$  and driving spring stiffness  $k_0 = 0.001$ .

Exponent	Perpendicular chain	Dense chain	Sparse chain
$\tau_S$	$1.44 \pm 0.08$	$2.19 \pm 0.08$	$1.40 \pm 0.10$
$\tau_T$	$1.42 \pm 0.09$	$2.80 \pm 0.08$	$1.42 \pm 0.10$
$\tau_I$	$1.36 \pm 0.12$	$1.51 \pm 0.14$	$1.43 \pm 0.11$

## 6.4 Contact aging

Even though contact aging does not introduce new avalanches like the after-shocks in the viscoelastic model, it alters the existing dynamics by introducing a form of memory to the system. The prominence of contact aging can be tuned with the aging coefficient  $\alpha$ , the aging timescale  $t_\alpha$  and the de-aging timescale  $t_\beta$ .

If the aging of the contact is rapid, the surface force increase coefficient  $\mu_i$  saturates very fast when a particle is stationary. Hence the aging timescale was set such that with the lowest driving spring stiffness,  $k_0 = 0.001$ , the surface force multiplier saturates slowly enough so that particles with different rest times have significantly different surface force multipliers. The de-aging timescale  $t_\beta$  was chosen to be very small, so that the contacts de-age rapidly when the system moves. This means that the surface force increase coefficient  $\mu_i$  decays by about 63% in 10 timesteps (by comparison, the shortest slips typically last about 100 timesteps). The control parameter values are collected in Table 6.9.

Table 6.9: The control parameter values for contact aging simulations.

Control parameter	Value
Driving velocity $V$	0.005
Driving spring constant $k_0$	0.1, 0.01, 0.001
Particle equilibrium distance $d$	1, 20
Aging coefficient $\alpha$	0.1, 0.3, 0.5
Aging timescale $t_\alpha$	10000
De-aging timescale	1
Driving paused while slipping	True
Slip characterization method	Velocity threshold
Relaxation velocity threshold	0.05

### 6.4.1 Perpendicular chain: onset of motion

Contact aging tends to promote large slips, especially in the beginning (since the chain is at rest for a long time in the start, giving the contacts time to age). The preference for larger slips can be seen also in the velocity data for the particles (Fig. 46).

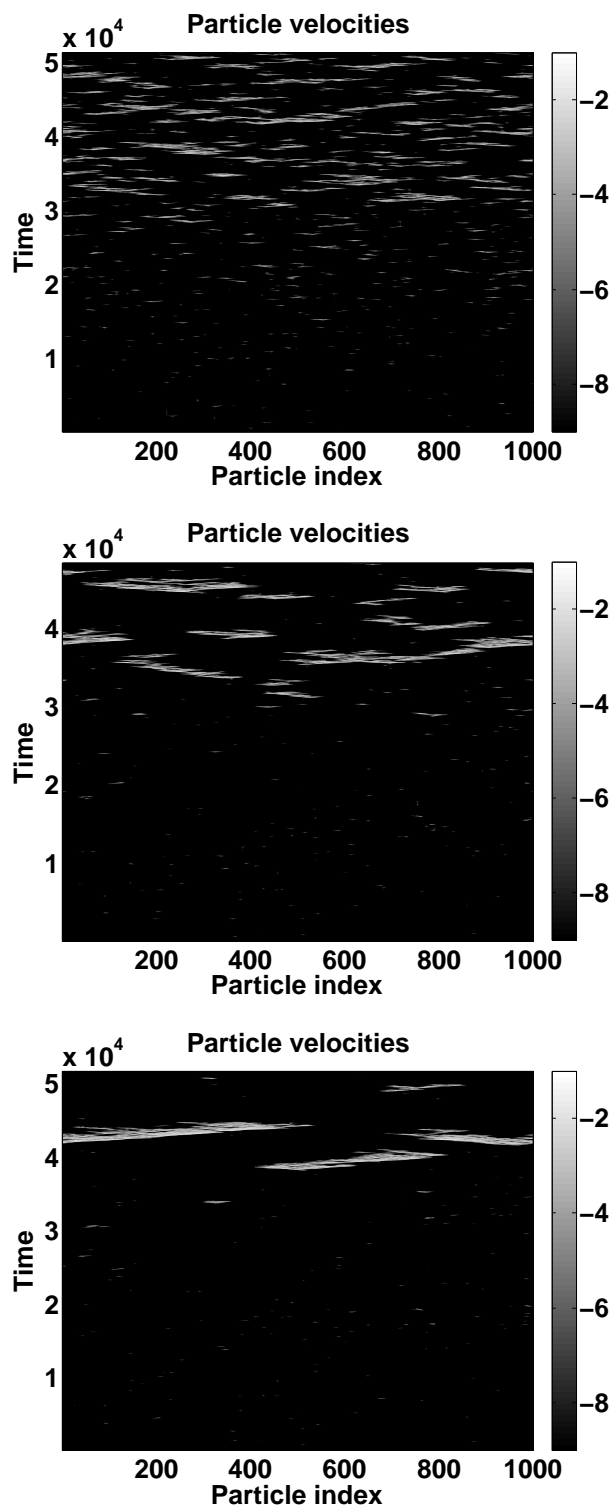


Figure 46: Compared to the basic model (top), the contact aging increases the size of the slips, depending on the aging coefficient  $\alpha$  (0.3 in the middle, 0.5 at the bottom). With high  $\alpha$  system-wide slips can occur even in the 1000-particle chain.

The friction force without contact aging and with aging coefficient values 0.1, 0.3 and 0.5 is illustrated in Fig. 47. Due to the roughly system-wide slips at higher values for  $\alpha$ , the time development of the friction force starts resembling the sawtooth-like curve of macroscopic stick-slip.

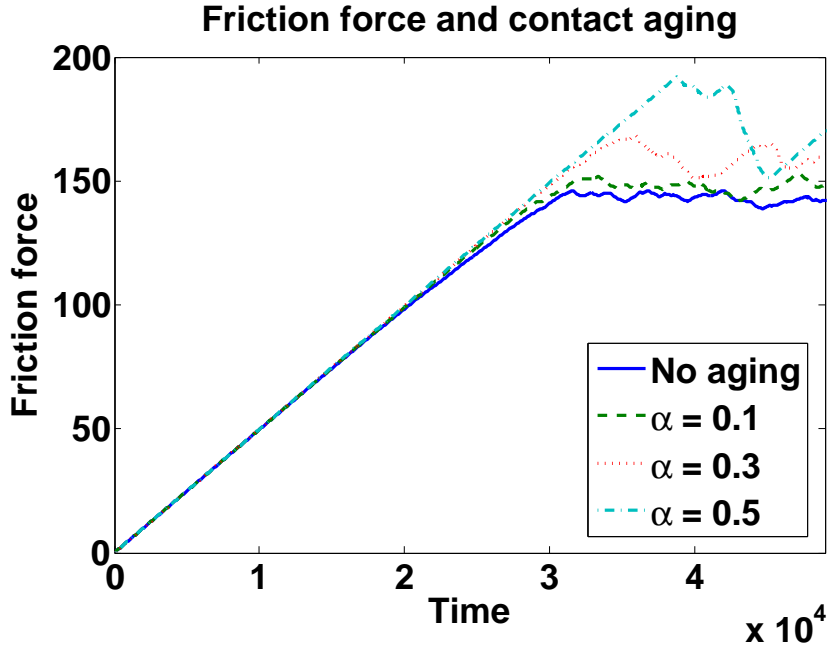


Figure 47: The friction force during the onset of motion for a perpendicular chain with and without contact aging.

Due to the contact aging, the friction force starts showing velocity weakening behaviour: higher driving velocities give the contacts a smaller time window for aging, resulting in smaller slips and overall lower friction force (Figs. 48 and 49). When the velocity increases sufficiently, the friction force starts increasing again. This naturally happens only when the driving is not stopped while slipping, and thus does not show up in the avalanche statistics, which are performed simulating quasistatic driving. However, velocity weakening has been observed in stick-slip motion, and thus the model incorporating contact aging could be considered more realistic than the vanilla FKT model in this regard [48].

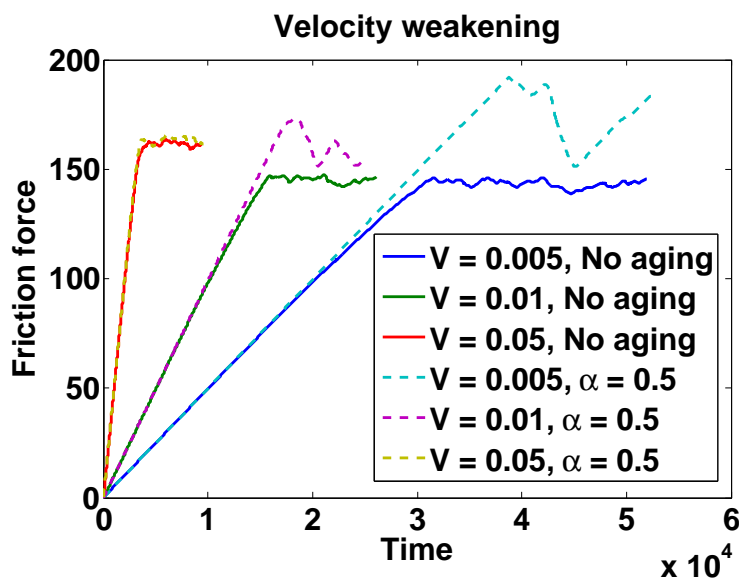


Figure 48: The weakening of the friction force with  $\alpha = 0.5$  for velocities 0.005, 0.01 and 0.05 for a perpendicular chain of 1000 particles. The basic FKT model does not display velocity weakening. On the contrary, the steady state friction force is strengthened with higher velocities.

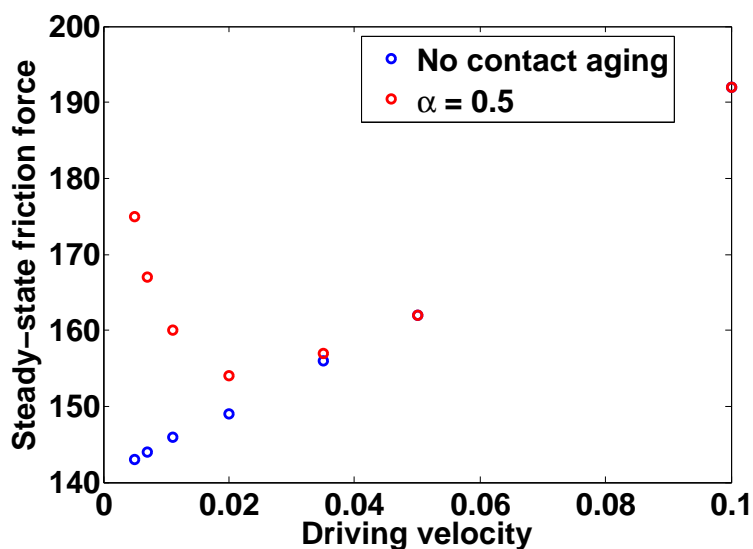


Figure 49: The average steady-state friction force for multiple velocities in the basic model and the model with contact aging.

### 6.4.2 Perpendicular chain: avalanche statistics

The contact aging has an effect on the slip statistics in the form of increased cut-off for all distributions and a small bump in probability at largest/longest slips for high values of  $\alpha$ . With stiffer driving spring, the effect is diminished, since (like in the increased velocity case seen above) the contacts don't have time to age as much. Fig. 50 presents the comparison between the basic model and the model with contact aging for  $k_0$  values 0.1, 0.01 and 0.001. Since the case  $k_0 = 0.001$  displays the effects of contact aging the most, the simulations for different  $\alpha$  values were run for this driving spring stiffness only.

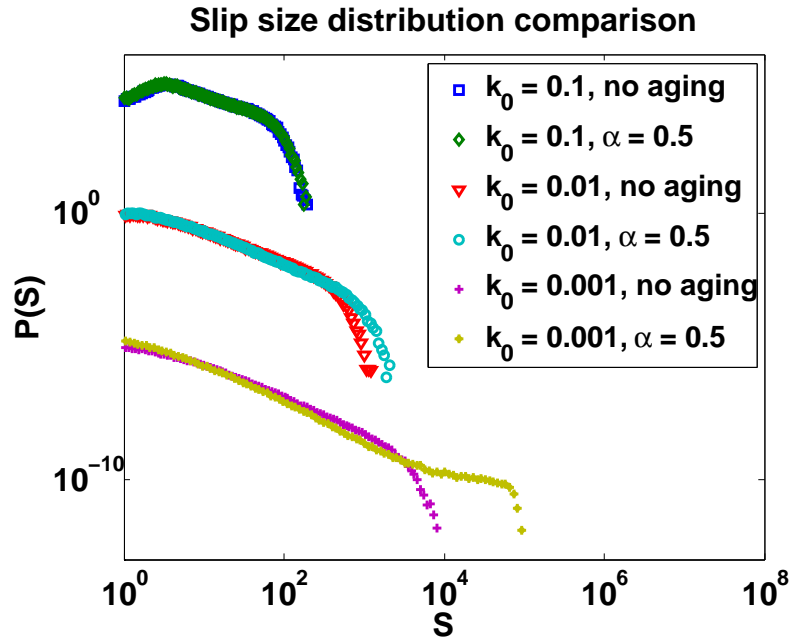


Figure 50: When  $k_0$  is large, the contacts don't have time to age and so the distributions look similar with or without contact aging. The distributions are scaled to separately show the effects of the different values of  $k_0$ .

Much like in the viscoelastic case, the avalanche size and duration exponents grow due to contact aging (Figs. 51 and 52), and the increase is higher with larger  $\alpha$ . An explanation for this might be that on average, the larger slips tend to require longer driving, feeling the effects of contact aging more. Thus the larger slips of the basic FKT model have a higher chance to be "converted" to still larger slips (which form the probability bump/plateau after the power law section in the distributions) because of contact aging.



Hence the slips of the contact aging model tend to be more divided in size than in the vanilla model; there are the small slips, for which the contact aging has little effect, and the larger, possibly system-wide slips. The high values of  $\alpha$  enforce this division. The larger slips are accompanied by longer intervals (Fig. 53), but otherwise the interval distribution is similar to the vanilla model.

It's also possible that like in the viscoelastic case, an avalanche oscillator is induced by the nonstationary dynamics: the aging contact competes with the increase in driving, causing oscillations in the distributions. The total distribution is sampled over all phases of the oscillation, and thus has higher exponents.

The increase of probability of large slips causes the distributions to not conform to fitting a power law with exponential cut-off. Thus the critical exponent of the power law part was determined by fitting a line to the log-log plot to the power law part before the bump in the distribution.

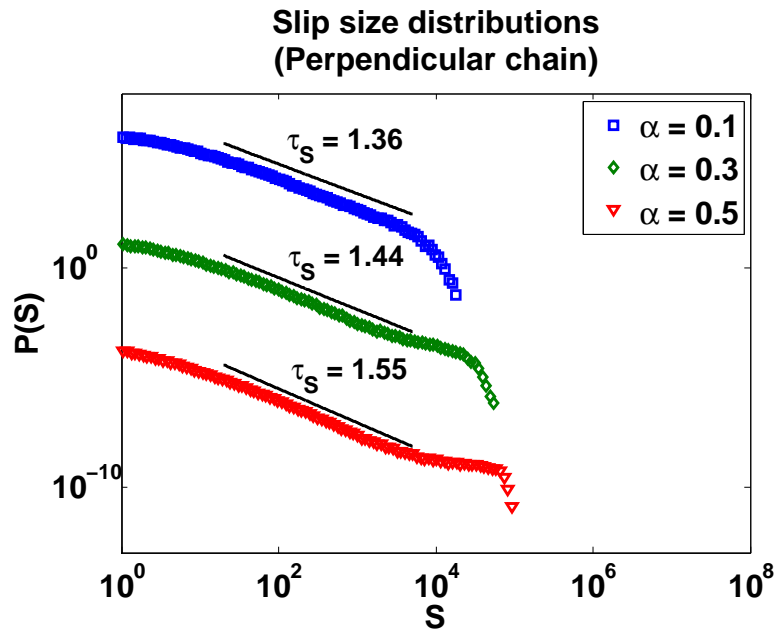


Figure 51: The critical exponent  $\tau_S$  grows with stronger contact aging, and the cut-off is pushed towards larger slips.

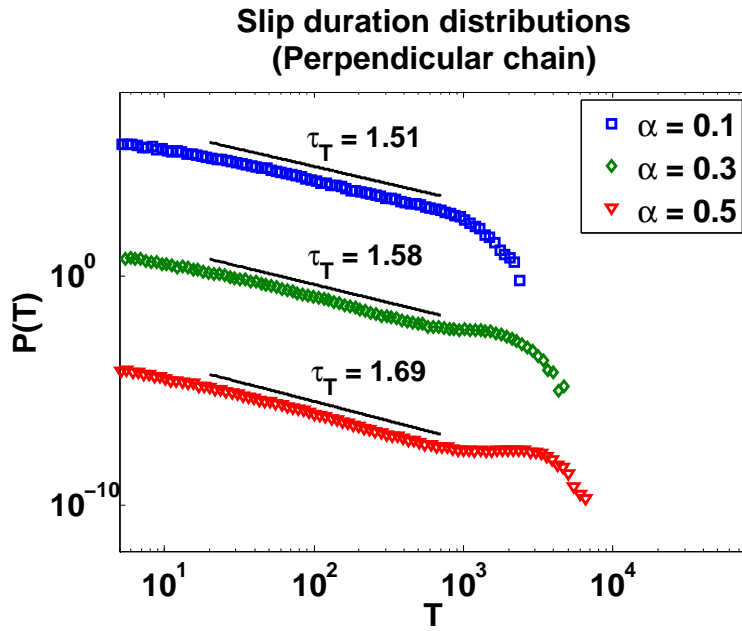


Figure 52: The duration critical exponent  $\tau_T$  also follows a similar pattern as the size exponent, but the exponents are little higher.

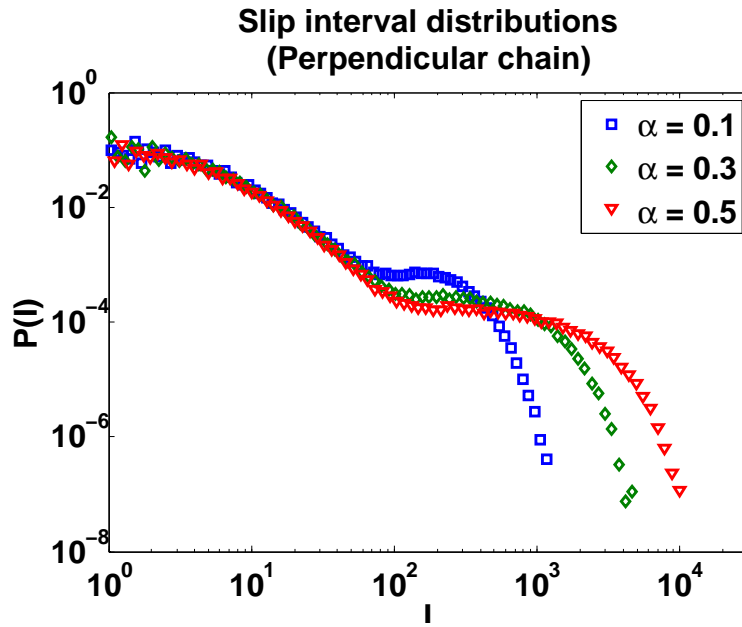


Figure 53: The contact aging increases the cut-off of the interval distribution, but other than that, the effects of contact aging are minor.

### 6.4.3 Parallel chain: onset of motion

In onset of motion of the sparse chain, the effects of contact aging are comparable to the perpendicular chain: the slips become larger and the intervals get longer. The periodicity is reduced because of the memory effects from the contact aging (Fig. 54).

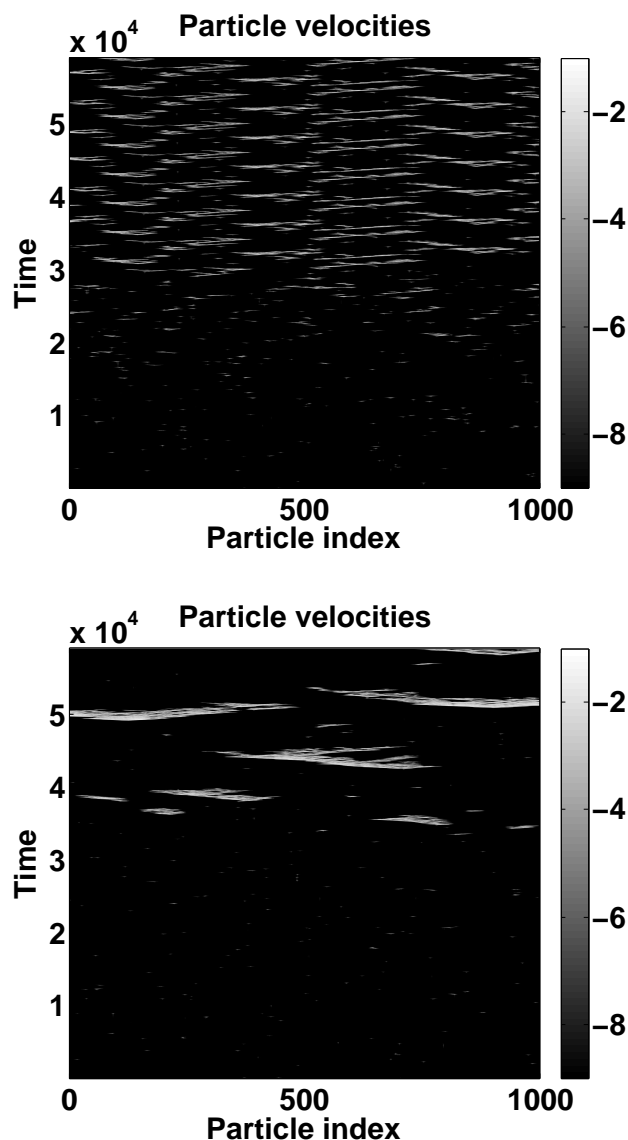


Figure 54: Comparison between parallelly driven 1000-particle sparse chains without contact aging (top) and with aging coefficient  $\alpha = 0.5$  (bottom).

In the dense chain, the behaviour of particles in the deepest wells is altered somewhat. In addition to the traffic jams and single propagating kinks seen in the basic model, the deep wells start to accumulate particles if the contact aging is strong enough. When the forwardmost particle exits the well, the friction force it is experiencing decreases rapidly, and as a result the particle slips far enough to cause the next particle in the well to accelerate above the relaxation threshold velocity. Thus the contact strength diminishes also for the second particle, and it too slips, dragging the next particle and so on. The effect propagates through most of the particles in the well, resulting in a large avalanche (Fig. 55).

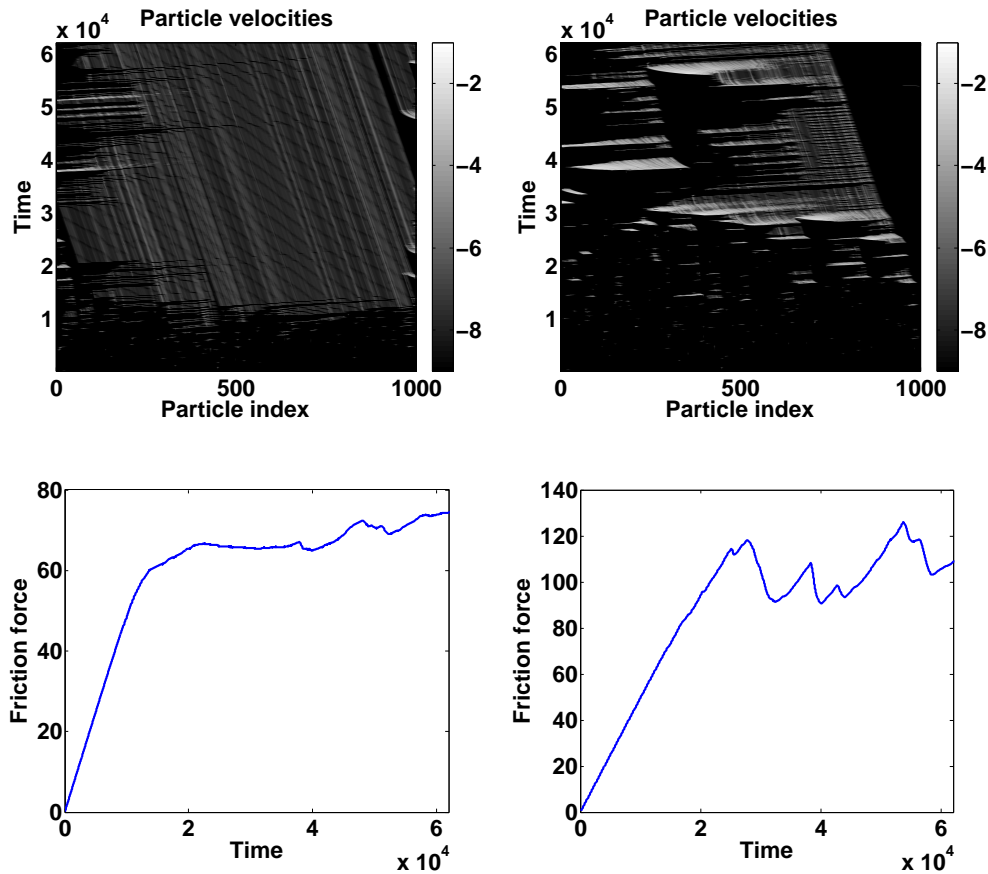


Figure 55: In the dense parallel chain, the smooth motion of the basic model (left) is disturbed by the contact aging. The avalanches originating from the deep wells are large enough to show up as large fluctuations in the friction force (right).

#### 6.4.4 Parallel chain: avalanche statistics

The results for the sparse parallel chain resemble those of the perpendicular chain: the cut-offs of size and duration distributions are pushed towards larger and longer slips, respectively, and the intervals also become longer. The size and duration critical exponents increase depending on  $\alpha$ . The distributions for the sparse chain are presented in Figs. 56, 57 and 58.

Surprisingly the dense parallel chain behaves a quite like in the viscoelastic simulations: the power law section (if there can be said to be one) seems to move towards larger slips and the cut-off disappears (Fig. 59), though the part with smaller slips does not change as much as in the viscoelastic case and the critical exponents  $\tau_S$  and  $\tau_T$  are not as high. Interestingly, the exponent seems to decrease a bit with the highest  $\alpha$ . The cut-off of the interval distribution moves toward longer intervals.

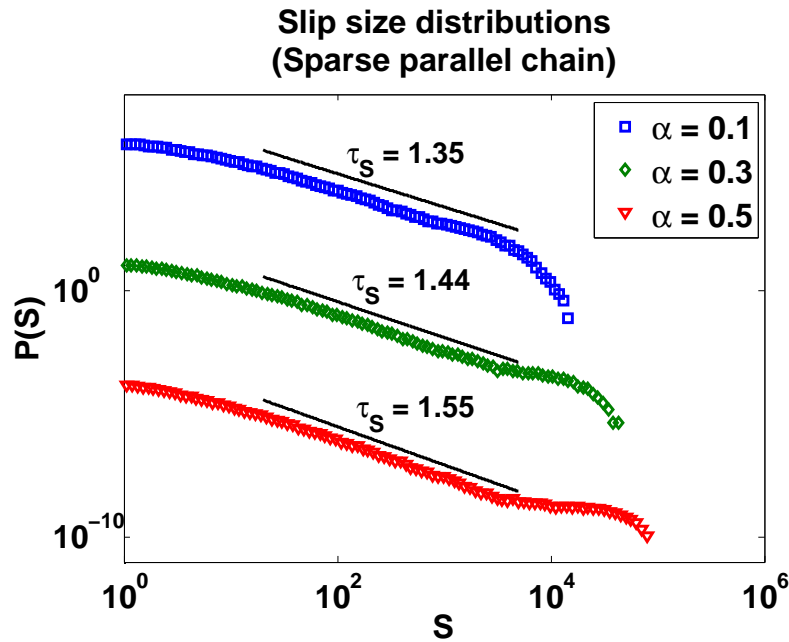


Figure 56: The sparse parallel chain behaves comparably to the perpendicular chain in the model incorporating contact aging.

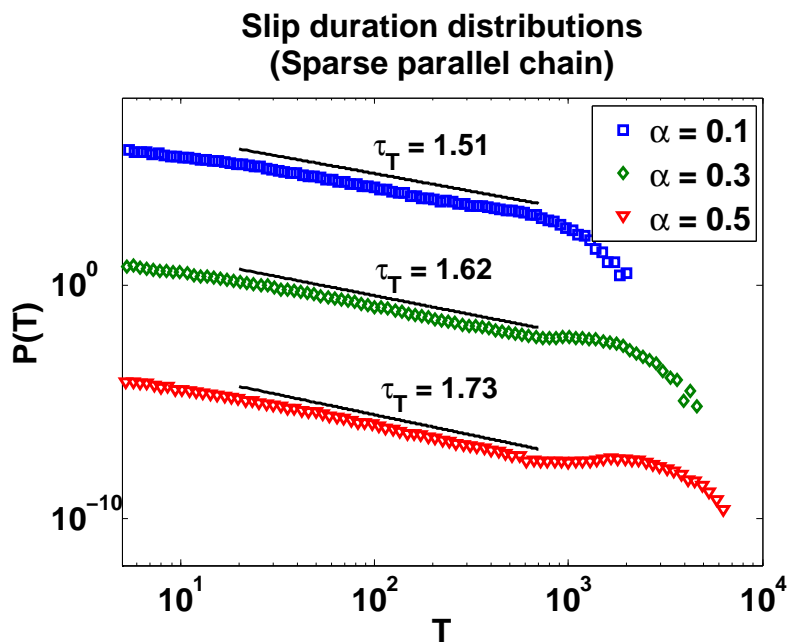


Figure 57: The bump in the duration distributions seem more pronounced than in the size distributions.

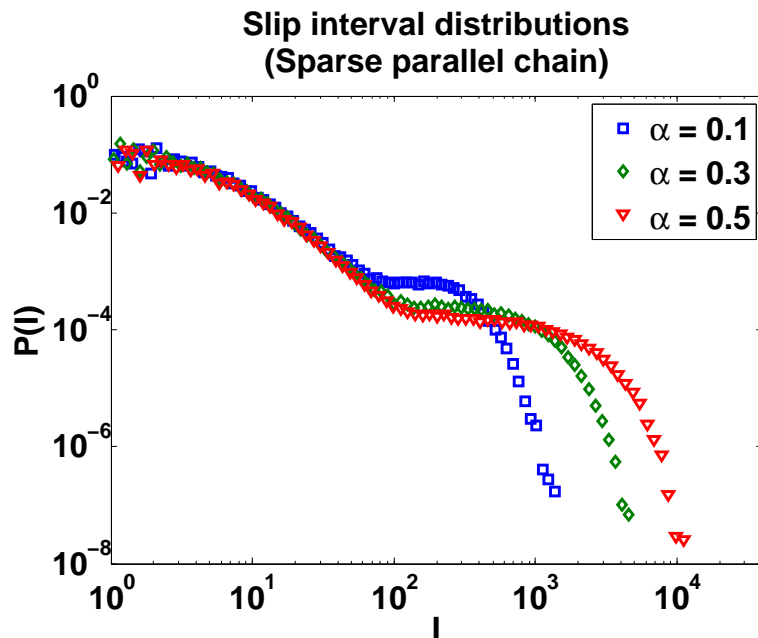


Figure 58: The interval distribution of the sparse parallel chain is also nearly identical to that of the perpendicular chain.

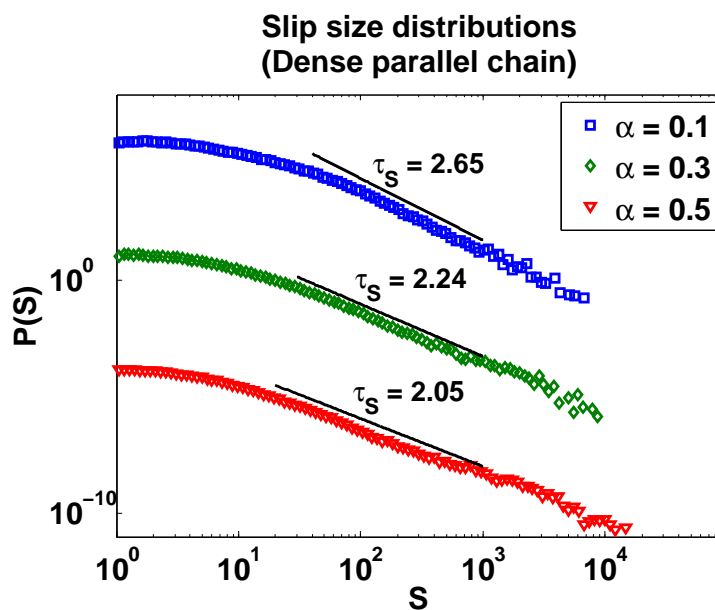


Figure 59: The size distribution of the dense chain reacts to the contact aging similarly to viscoelasticity: the larger slips seem to become power law distributed.

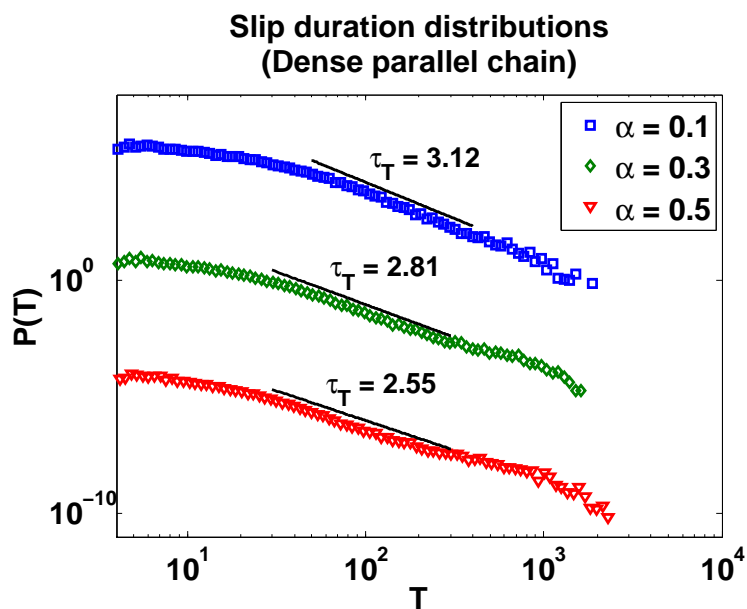


Figure 60: The duration distribution of the dense chain seems to retain the same very short linear part in the small slip region. Like in the size distributions, the cut-off might turn into a power law.

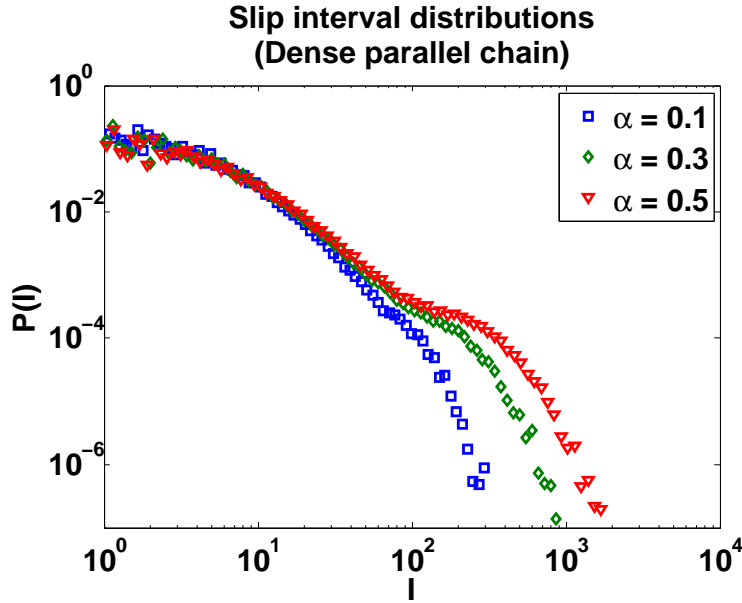


Figure 61: The cut-off of the interval distribution of the dense parallel chain reacts to the increasing  $\alpha$ , most likely due to the large collective slips from traffic jams.

All in all, the effects of contact aging were relatively minor, at least in the perpendicular chain and the sparse parallel chain. The critical exponents increased roughly like in the viscoelastic model, though the growth in the exponents was a bit more pronounced. The cut-offs were moved toward the larger and longer slips, which was expected.

The dynamics of the dense parallel chain experienced a qualitative change in the form of "traffic jam avalanches", which were likely the cause of the power law -like distribution of larger avalanche sizes. The critical exponents for  $\alpha = 0.5$  and  $k_0 = 0.001$  are collected in Table 6.10.

Table 6.10: The critical exponents in the contact aging model for the perpendicular chain and the dense and sparse parallel chains.

Exponent	Perpendicular chain	Dense chain	Sparse chain
$\tau_S$	$1.51 \pm 0.07$	$2.06 \pm 0.18$	$1.54 \pm 0.11$
$\tau_T$	$1.68 \pm 0.08$	$2.55 \pm 0.19$	$1.68 \pm 0.10$



## 6.5 Simulations with both contact aging and viscoelasticity

When both effects are on, the dynamics of the system consist mainly of large slips because of the contact aging, followed by numerous aftershocks due to the viscoelastic relaxations. However, there's some interplay between the two effects. Since the viscoelastic relaxations happen below the relaxation velocity threshold, the contacts age also during the relaxations, and might impede the movement. Additionally, since a slip combined with a relaxation event takes more time than just slipping, the parts of the chain not taking part in the slip have their contacts strengthened more. This leads to the cut-off moving even further towards larger slips.

In order to avoid finite size effects, the aging coefficient value used was 0.3 instead of 0.5 (with  $\alpha = 0.5$ , system-wide slips were frequent). To be able to best observe the combined effects of viscoelasticity and contact aging, the viscoelastic relaxation was kept slow, with  $\eta_u = 50$ . The parameters used in the simulations are presented in Table 6.11.

Table 6.11: The control parameter values used with simulations incorporating both viscoelasticity and contact aging.

Control parameter	Value
Driving velocity $V$	0.005
Driving spring constant $k_0$	0.1, 0.01, 0.001
Particle equilibrium distance $d$	1, 20
Dashpot viscosity $\eta_u$	50
Dashpot spring stiffness	1
Aging coefficient $\alpha$	0.3
Aging timescale	10000
De-aging timescale	1
Driving paused while slipping	True
Slip characterization method	Velocity threshold
Relaxation velocity threshold	0.05

### 6.5.1 Perpendicular chain: onset of motion

In the onset of motion simulations, the combined effects resulting in larger slips are not easily noticeable, since the chain is not stopped during slips and viscoelastic relaxations. Thus the contact aging and viscoelasticity had

seemingly independent effects: the slips were made larger by the aging contacts, and viscoelastic relaxation happened between the larger slips, possibly causing aftershocks. The contact aging seems to dominate the onset of motion, since the effects of viscoelasticity show better at smaller length scales. However, when comparing the onset of motion of the model with only contact aging and model with both effects (Fig. 62 top and bottom, respectively), it can be seen that there are more precursory slips and smaller slips in general, and the larger individual slips extend longer in time and space. Both changes can be attributed to the viscoelastic relaxations.

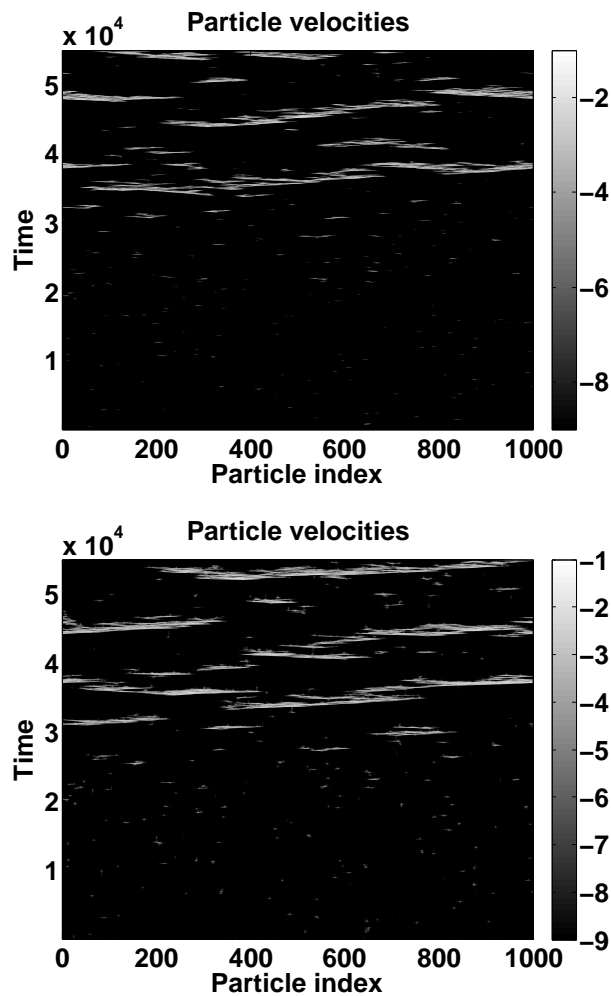


Figure 62: The onset of motion of the perpendicular chain with just contact aging (top) and with both effects (bottom). The size of larger slips is increased when both effects are incorporated in the simulations, though there seem to be more slips of smaller size as well.

### 6.5.2 Perpendicular chain: avalanche statistics

The critical exponents  $\tau_S$  and  $\tau_T$  don't change drastically for the system with both viscoelasticity and contact aging when compared to just contact aging, though one has to take into account that  $\alpha = 0.3$  was used when obtaining the avalanche distributions (Figs. 63 and 64). Higher values of  $k_0$  tend to reduce the effects of contact aging, and the results thus match better to the model incorporating only viscoelasticity. Distributions acquired with low  $k_0$  show the cut-off increase seen with contact aging, but the effect is further strengthened due to the viscoelastic relaxations.

The interval distribution displays similarities to the viscoelastic case, indicating the presence of aftershocks (Fig. 64). However, the value of  $k_0$  has a larger effect on the results than in the simulations incorporating only viscoelasticity. Increase in  $k_0$  makes the aftershock intervals (assumed to be the middle portion of the distribution) curved. The sharp increase in probability after the power law part is also mitigated by the contact aging, and is only visible with the lowest  $k_0$ .

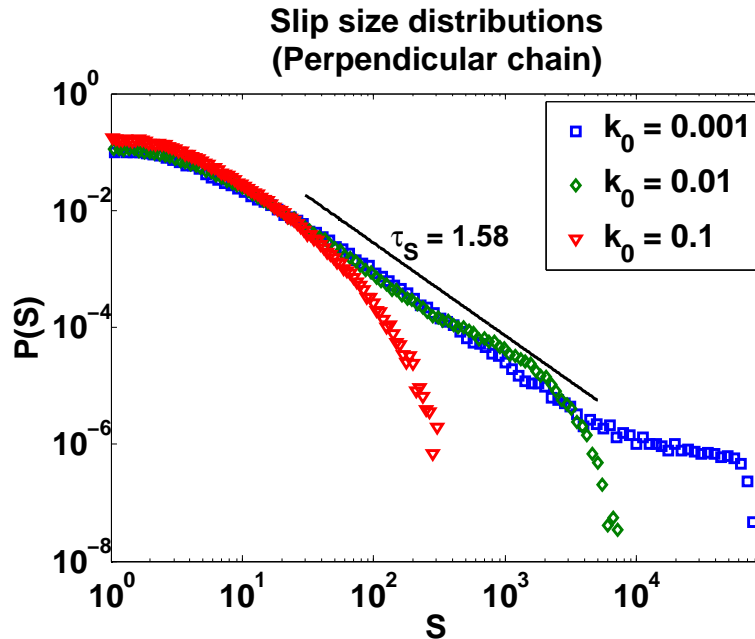


Figure 63: The size distributions for various values of  $k_0$ . Growing  $k_0$  diminishes the bump in the larger size events, since the system stays pinned less and the contacts don't age as much.

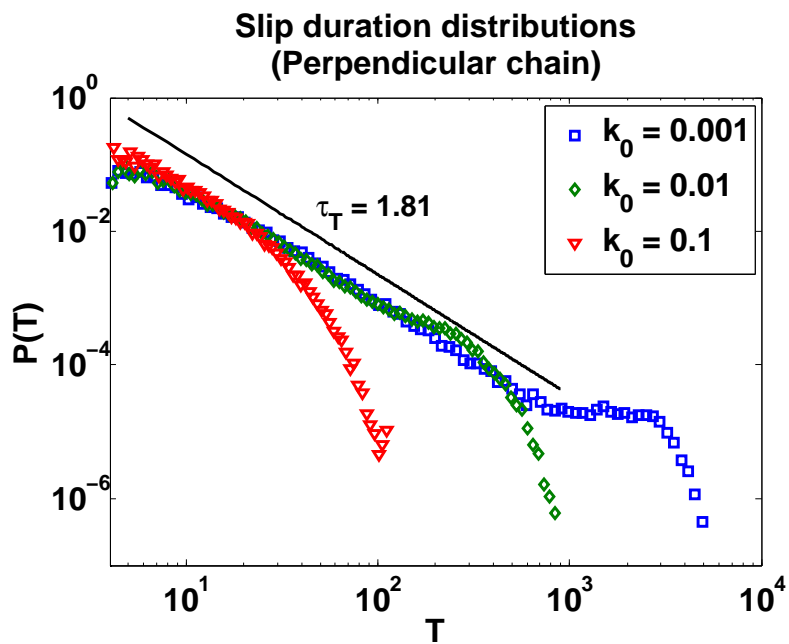


Figure 64: As usual, the interval distributions follows a similar pattern as the size distributions.

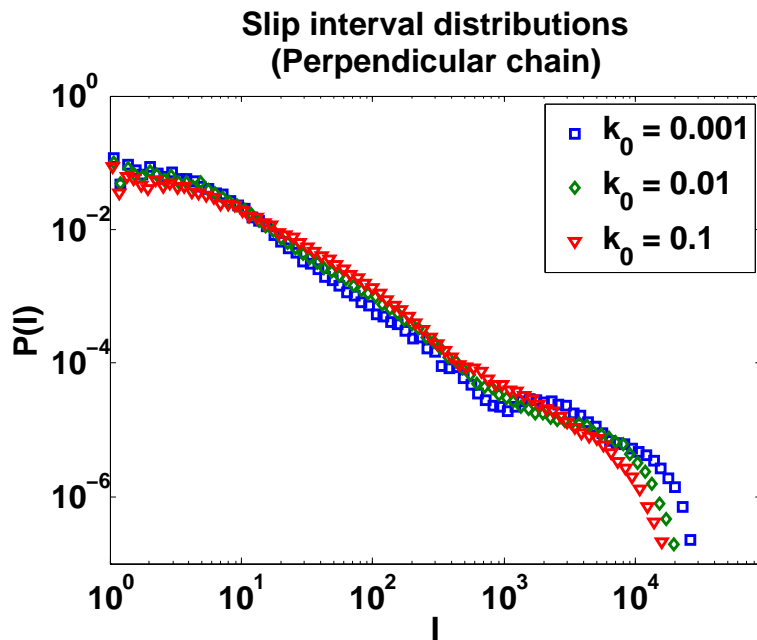


Figure 65: The interval distribution is changed the most when combining both contact aging and viscoelasticity.

### 6.5.3 Parallel chain: onset of motion

The sparse parallel chain seems to experience a more drastic change with both viscoelastic effects and contact aging: even with  $\alpha = 0.3$ , the slips cover much wider area of the chain than with just contact aging (Fig. 66). The dense chain also sees an increase in larger slips originating from the traffic jams, and the periodicity is further lessened (Fig. 67). In both dense and sparse chains, the number of small precursory slips is increased.

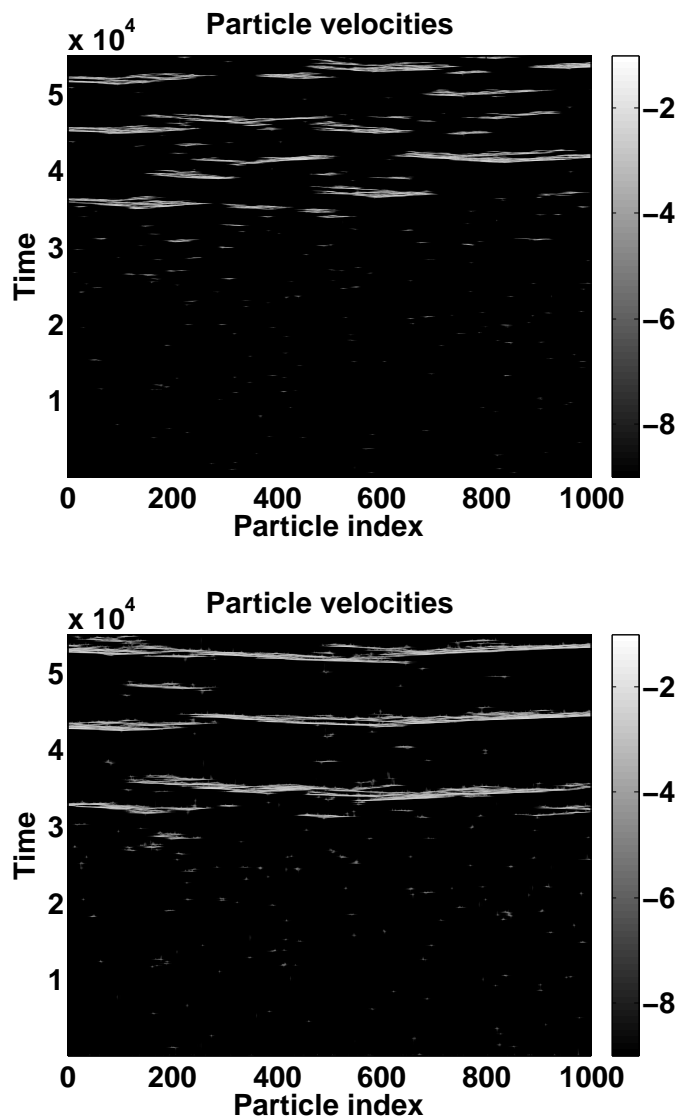


Figure 66: The onset of motion of the sparse parallel chain with contact aging (top), and with both viscoelasticity and contact aging (bottom).

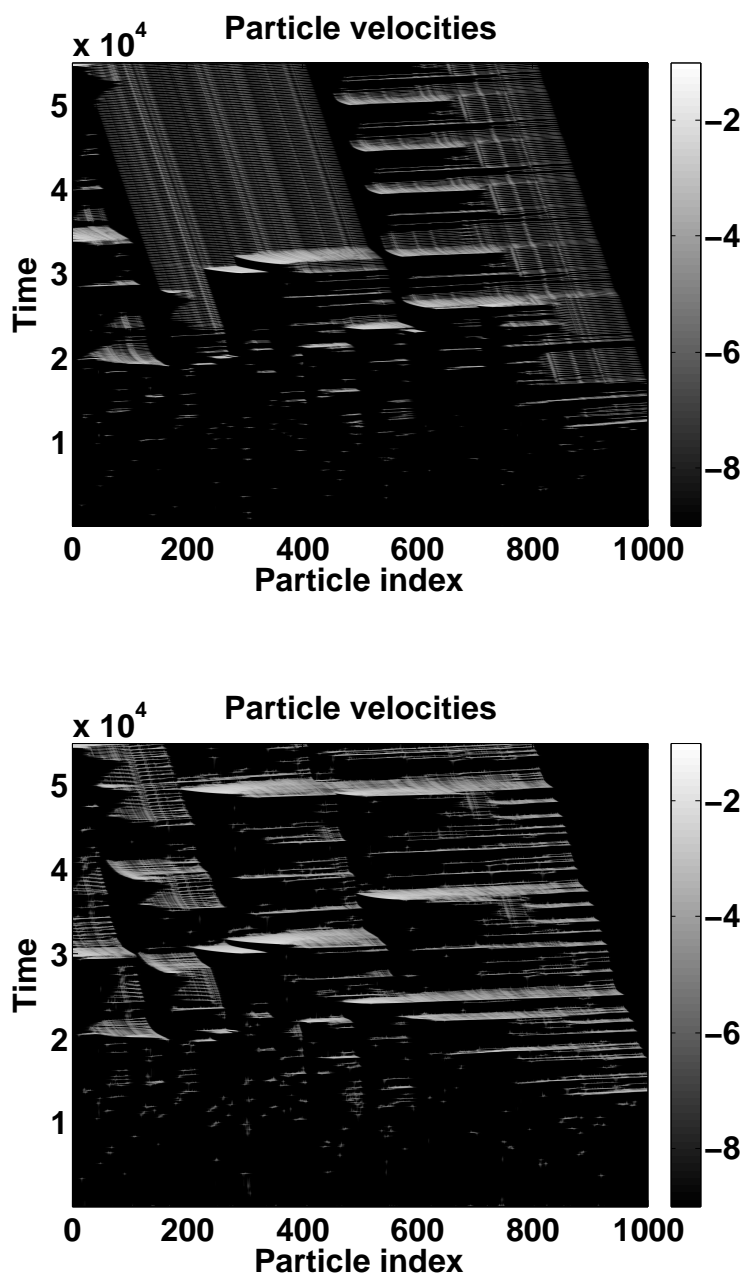


Figure 67: When compared to simulations with only contact aging (top), the dense chain becomes more chaotic when viscoelasticity is also included (bottom). The number of "traffic jam" avalanches seems to increase.

### 6.5.4 Parallel chain: avalanche statistics

Other than possibly slightly larger critical exponents, the avalanche statistics of the sparse parallel chain do not differ much from the perpendicular chain, which at this point could be expected. The size, duration and interval distributions are shown in Figs. 68, 69, 70, respectively.

In the case of the dense chain, the size distribution is similar to the one obtained from the model with only contact aging (Fig. 71), but surprisingly the size exponent  $\tau_S$  is a bit lower. The power law part is also more easily distinguished from the cut-off than in the contact aging simulations. The duration distribution becomes curved with  $k_0 = 0.001$  (Fig. 72), and there might even be three power law parts: short one at the smallest slips, steep in the middle, and one with low  $\tau_T$  for the largest slips. The slip interval distribution experiences barely any change at all, when compared to the viscoelastic case.

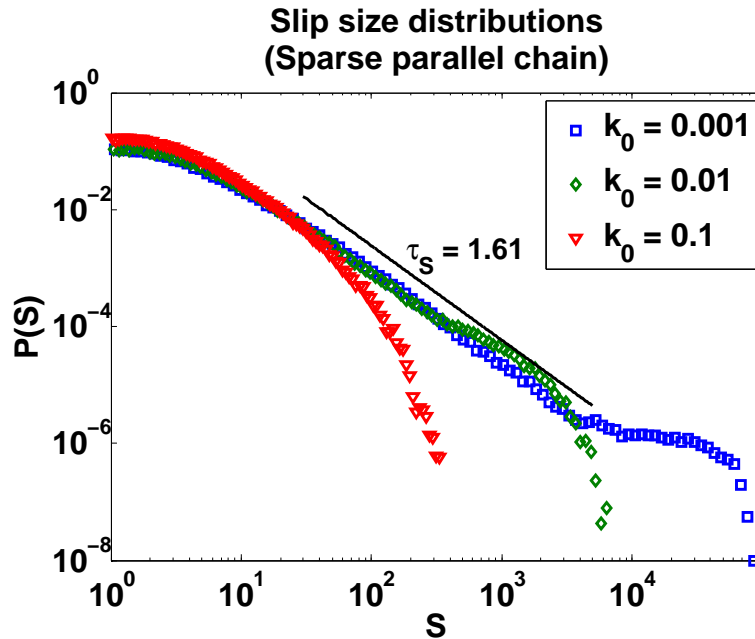


Figure 68: The sparse parallel chain exhibits similar behaviour as the perpendicular chain: longer cut-off with small  $k_0$ , and distribution closer to the viscoelastic case with large  $k_0$ .

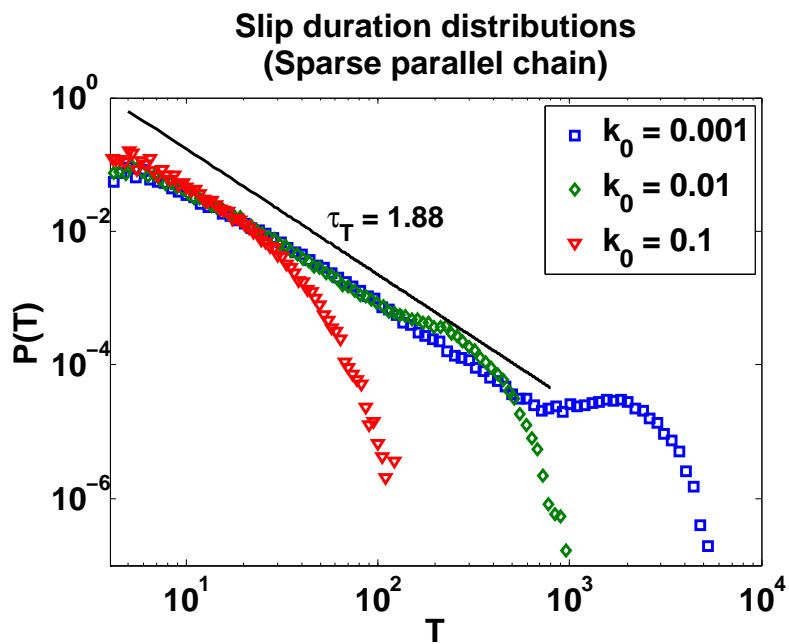


Figure 69: Like in the contact aging model, the durations show a larger bump in the distribution at lower values of  $k_0$ .

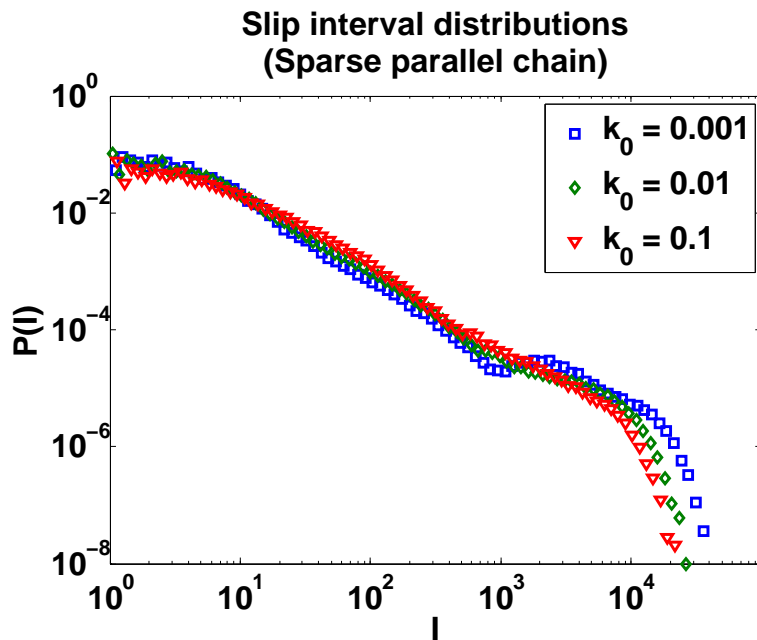


Figure 70: The interval distribution shows similar curved behaviour as in the perpendicular case.



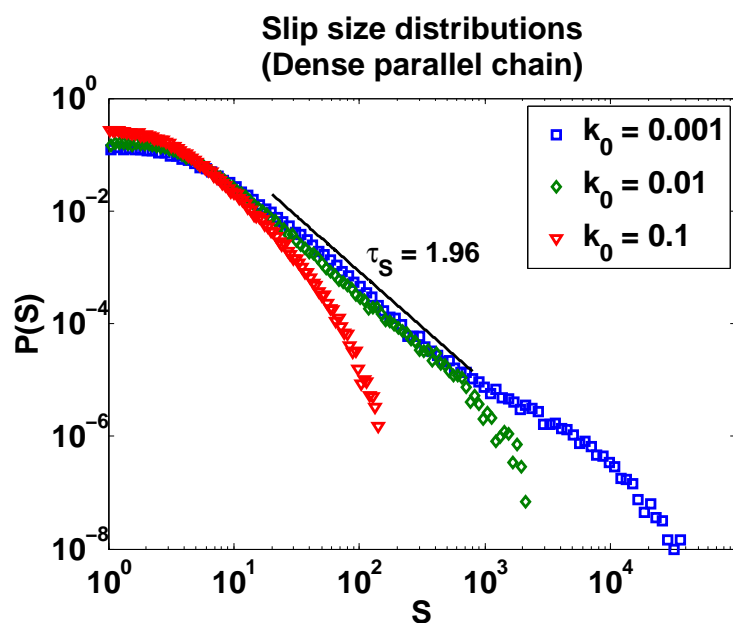


Figure 71: In the dense chain, the bump at large slips is more visible with both effects than with only contact aging, and the exponent  $\tau_S$  is smaller.

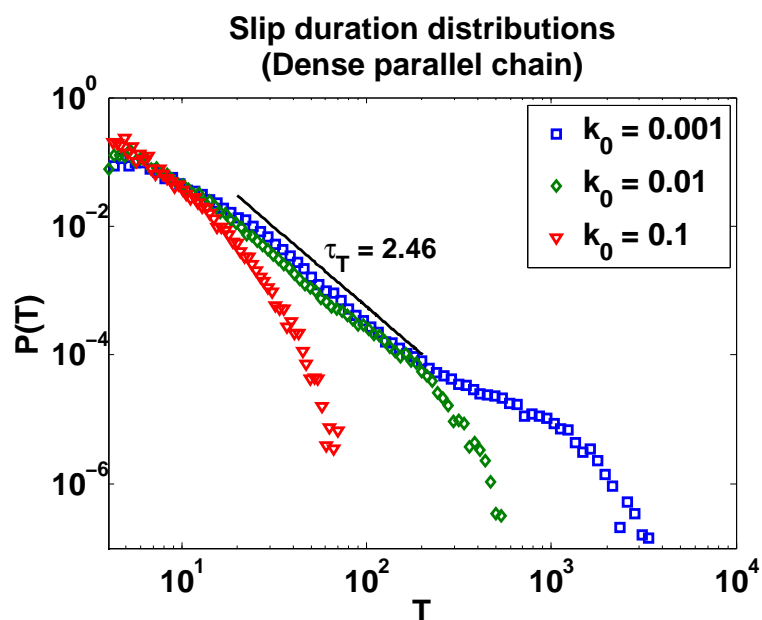


Figure 72: The avalanche duration distribution of the dense chain becomes curved at the shorter avalanches.

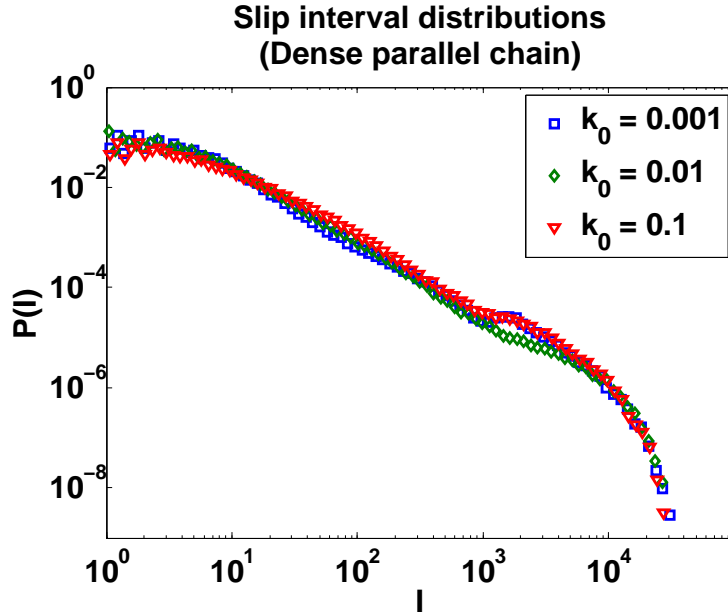


Figure 73: The interval distribution did not experience significant changes when using both contact aging and viscoelasticity when compared to simulations with only viscoelasticity.

The critical exponents of the distributions are collected in Table 6.12. Though the interplay of viscoelasticity and contact aging increased the cut-offs of the distributions and made the interval distribution somewhat  $k_0$  dependent, the overall changes to the statistics were relatively slight when compared to the model with just contact aging (or viscoelasticity, in the case of the interval distribution).

Table 6.12: The critical exponents in the FKT model incorporating both viscoelasticity and contact aging, with  $k_0 = 0.001$ ,  $\eta_u = 50$  and  $\alpha = 0.3$ .

Exponent	Perpendicular chain	Dense chain	Sparse chain
$\tau_S$	$1.58 \pm 0.13$	$1.91 \pm 0.19$	$1.61 \pm 0.11$
$\tau_T$	$1.81 \pm 0.15$	$2.46 \pm 0.21$	$1.88 \pm 0.13$

## Chapter 7

# Conclusions

In this work, the Frenkel-Kontorova-Tomlinson model was used to study the stick-slip motion of a 1-dimensional elastic chain on a disordered substrate and how said motion corresponds to frictional stick-slip motion. The basic FKT model was enhanced with two properties, viscoelasticity and contact aging, that have not been extensively studied as of yet. The central features of stick-slip motion investigated in this thesis were the onset of motion and the avalanche statistics.

Three kinds of chains were investigated: a perpendicularly driven chain, a parallelly driven with multiple wells between individual particles (sparse chain), and parallelly driven dense with few to no wells between individual particles (dense chain). Due to the comparatively large parameter space and time constraints, the effects of varying every parameter could not be studied. Hence a couple of primary control parameters were selected and altered in the simulations, while the rest were simply kept constant.

Out of the three types of chains, the perpendicular chain and the sparse parallel chain behaved similarly in most simulations, whereas the parallel dense chain acted in a completely different way. The main reason for this is the accumulation of multiple particles in same well and forming "traffic jams", which strongly affect the dynamics. In fact, the single kink movements in the dense parallel chain are hardly avalanche-like, which explains the differences to the perpendicular chain and sparse parallel chain in both the onset of motion and the avalanche statistics. However, when the kink propagation is stifled and multi-particle traffic jams made less probable by a stiffer driving spring, the dense chain too starts showing statistics characterized by a power law and an exponential cut-off.

The qualitative similarities to dry frictional motion in the basic FKT model were limited to stick-slip and velocity strengthening. Perpendicular and sparse parallel chains showed both, whereas the motion of the dense par-

allel chain resembled stick-slip only in at high  $k_0$ . Quantitatively, the critical exponents of the vanilla FKT model with either perpendicular or sparse parallel chains correspond quite well to experiments where the asperities are emulated with macroscopic objects, for example glass beads [56]. However, experiments concerning actual frictional stick-slip motion tend to have higher exponents [23, 57, 58]. In this regard, the basic FKT model does not provide comparable results. Another difference is that in macroscopic stick-slip motion, the friction force typically displays a sawtooth-curve, whereas in the simulations the force evolution was quite smooth. However, this happens due to the elasticity of the chain; having a rigid chain, the sawtooth-curve appears. Similarly, in the onset of motion the rigid chain displayed a wave-like propagation of the slip, which could be considered to correspond to the propagation of contact rupture measured in Ref. [32]. This effect was lessened in a more pliant chain, in which the slips could occur relatively independently. The small precursory slips were observed in the perpendicular and parallel chains, rigid or pliant. However, the steady-state of the rigid chains consisted mostly of system-wide slips, whereas the more pliant chains experienced slips with a wide range of widths.

These results would seem to indicate that in conventional laboratory dry friction experiments, elasticity does not play a large part and the sliding surfaces could be considered rigid. Considering that neither the rigid chain or the elastic chain produce critical exponents that are comparable to dry friction experiments, the elasticity does not seem to be a deciding factor from a realism viewpoint. Though it's likely that at the atomic level elastic deformations in the surfaces take place, few to none experiments have been made at such a small scale, as observing the motion becomes problematic.

When including viscoelastic effects in the model, the depinning dynamics of the chain changed into few avalanches caused by driving followed by aftershocks in between. The distributions of the avalanches differed from the basic model: the critical exponents  $\tau_S$  and  $\tau_T$  were roughly 0.2 – 0.3 higher in the perpendicular and sparse parallel chains, and the avalanche intervals became power law distributed with exponents  $\tau_I \approx 1.3 – 1.7$  (depending on the viscoelasticity of the dashpots) in all three types of chains. The increase in size and duration exponents have two possible explanations: either the aftershocks have a distribution of their own, or the system is taken further away from the critical force due to the relaxation avalanches, leading to the oscillation in the cut-offs of the distribution and hence higher exponents when integrating the distribution (avalanche oscillator). Qualitatively, the increase in the critical exponents is similar to other simulations dealing with viscoelasticity [5, 55], but quantitatively the increase of exponents in this thesis is somewhat smaller.

Though the critical exponents of the avalanche size and duration distributions were closer to those of dry friction experiments, the presence of aftershocks is a phenomenon which has not been documented in microscopic or macroscopic friction experiments, excluding earthquakes. It's possible that in laboratory experiments, the systems are stiff enough to effectively prevent aftershocks (or the aftershocks are so small that they are not in measurement range), and the viscoelasticity is only displayed as contact aging due to the surfaces relaxing against each other, strengthening contacts. Thus the effects of viscoelasticity shown in this thesis may be better applicable to earthquakes than smaller scale dry friction. Velocity weakening in the friction force was observed in Ref. [5], however in this work the effect was absent. It's possible that the parameter regime where the velocity weakening would be observed was simply not found in this thesis.

Contact aging also showed an increase in the critical exponents, with high values for the contact aging coefficient boosting the size and duration exponents about the same magnitudes as the viscoelastic effects. The increase can be attributed to the avalanche oscillator phenomenon, since the contact aging and driving are competing in the same timescale. The cut-off is also increased substantially for the perpendicular chain and the sparse parallel chain for low values of  $k_0$ . The increase in cut-off can be caused by the contact aging inducing system-wide slips when  $\alpha$  was high. In the dense chain, a new kind of "traffic jam avalanche" appeared, and the cut-off of the distribution seemed to become linear like in the viscoelastic case. With contact aging, however, the cut-off isn't linear to the end, as the larger slips have a slight bump in probability. During the onset of motion, contact aging reduces the amount of precursory slips while increasing their size in the perpendicular and sparse parallel chains. The model also starts showing velocity weakening in addition to the velocity strengthening of the basic FKT model. In this regard, the behaviour is closer to that found in dry friction [48].

Using both effects together heightened the effects of contact aging due to the slow relaxation of the dashpots, and the critical exponents were possibly a bit higher in the perpendicular and sparse parallel chain. It's possible that the oscillations in the avalanche distributions are larger in this case, leading to larger exponents. Otherwise, no significant changes were observed. In the dense parallel chain, the larger slips become more noticeable in the distribution, possibly due to the increase in avalanches originating from traffic jams. In the onset of motion, precursory avalanches were more prominent with both effects on when compared to only contact aging.

Overall, viscoelasticity and contact aging bring about qualitative and quantitative changes in the FKT model and the model with these extensions appears to give results closer to those found in dry friction experiments.

However, the model and the results are still far from realistic depiction of frictional stick-slip motion, especially in the avalanche distribution critical exponents. It would seem that a more fundamental change is required should one wish to quantitatively model friction with the FKT model. Some results, mainly the aftershocks in the viscoelastic model, can also be more easily connected to earthquake dynamics than dry friction.

## 7.1 Future prospects

Though many interesting aspects from the Frenkel-Kontorova-Tomlinson model with added viscoelasticity and contact aging were found, there's still lot of room for improvement.

A fundamental deviation from reality is that the simulations were one-dimensional. Thus a simple but likely effective improvement would be to extend the simulation to two or even three dimensions. Another way to enhance the simulation would be to model the substrate similarly as the chain, i.e. as particles attached to each other with springs, or possibly viscoelastic elements. It would probably make for a more realistic surface than the rigid potential surface. Adding some form of wear mechanism to the substrate could also give interesting results, though one would have to define what exactly wear would mean in this case, and the implementation could prove difficult.

One thing left unclear was whether it is possible to have chaotic motion in the parallel chain without the nearly system-sized slips. If the substrate potential is sinusoidal, literature indicates the logical conclusion that the movement always becomes regular at some point, but for a disordered substrate the question remains open. This might be a simple problem of utilizing the right parameters, but despite many attempts, such parameters were not found during this work.

In this thesis, the effects of viscoelasticity and contact aging, rather than their physical causes, were studied. An interesting endeavor would be to create a model where the possible causes for viscoelasticity and contact aging would be simulated, making these effects arise from the system itself.

# Bibliography

- [1] S. Hashmi, G. Batalha, C. Van Tyne, and B. Yilbas. *Comprehensive Materials Processing*. 2014.
- [2] L. Gratton and S. Defrancesco. A simple measurement of the sliding friction coefficient. *Physics Education*, 41(3):232, 2006.
- [3] O. Ben-David and J. Fineberg. Static friction coefficient is not a material constant. *Phys. Rev. Lett.*, 106:254301, Jun 2011.
- [4] Z. Deng, A. Smolyanitsky, Q. Li, X. Feng, and R. Cannara. Adhesion-dependent negative friction coefficient on chemically modified graphite at the nanoscale. *Nat Mater*, 11(12):1032–1037, Dec 2012.
- [5] F. Landes. *Viscoelastic Interfaces Driven in Disordered Media and Applications to Friction. Disordered Systems and Neural Networks*. PhD thesis, Institut d’Optique Graduate School, 2014.
- [6] M. Chaudhury. Adhesion and friction of self-assembled organic monolayers. *Current Opinion in Colloid & Interface Science*, 2(1):65 – 69, 1997.
- [7] H. Yoshizawa, Y. Chen, and J. Israelachvili. Fundamental mechanisms of interfacial friction. 1. relation between adhesion and friction. *The Journal of Physical Chemistry*, 97(16):4128–4140, 1993.
- [8] H. Gao and H. Yao. Shape insensitive optimal adhesion of nanoscale fibrillar structures. *Proceedings of the National Academy of Sciences of the United States of America*, 101(21):7851–7856, 2004.
- [9] J. Crassous, L. Bocquet, S. Ciliberto, and C. Laroche. Humidity effect on static aging of dry friction. *EPL (Europhysics Letters)*, 47(5):562, 1999.

- [10] H. Matsukawa and T. Saito. Friction, stick-slip motion and earthquake. In Pratip Bhattacharyya and BikasK. Chakrabarti, editors, *Modelling Critical and Catastrophic Phenomena in Geoscience*, volume 705 of *Lecture Notes in Physics*, pages 169–189. Springer Berlin Heidelberg, 2006.
- [11] G. Durin and S. Zapperi. The Barkhausen effect. *eprint arXiv:cond-mat/0404512*, Apr 2004.
- [12] Y. Toivola, B.P. Somerday, R. Shediak, and M.P. Ivill. Stick-slip fracture of polymer/metal interfaces. In *Symposia DD - Polymer Interfaces and Thin Films*, volume 710 of *MRS Proceedings*, 2001.
- [13] B. Persson. *Sliding friction: physical principles and applications*, volume 1. Springer, 2000.
- [14] A. Vanossi, N. Manini, M. Urbakh, S. Zapperi, and E. Tosatti. *Colloquium* : Modeling friction: From nanoscale to mesoscale. *Rev. Mod. Phys.*, 85:529–552, Apr 2013.
- [15] Introduction to tribology - friction. <http://depts.washington.edu/nanolab/ChemE554/Summaries%20ChemE%20554/Introduction%20Tribology.htm>. Accessed: 2015-01-23.
- [16] B. Bhushan, editor. *Modern Tribology Handbook*. CRC Press, 2001.
- [17] R. Budakian and S. Putterman. Time scales for cold welding and the origins of stick-slip friction. *Phys. Rev. B*, 65:235429, Jun 2002.
- [18] S. Aubry, A. Bishop, and T. Schneider. Solitons and condensed matter physics. *Springer, New York*, 264, 1978.
- [19] R. Zhang, Z. Ning, Y. Zhang, Q. Zheng, Q. Chen, H. Xie, Q. Zhang, W. Qian, and F. Wei. Superlubricity in centimetres-long double-walled carbon nanotubes under ambient conditions. *Nat Nano*, 8(12):912–916, Dec 2013.
- [20] M. Ma, A. Benassi, A. Vanossi, and M. Urbakh. Critical length limiting super-low friction. *ArXiv e-prints*, Jan 2015.
- [21] W. F. Brace and J. D. Byerlee. Stick-Slip as a Mechanism for Earthquakes. *Science*, 153:990–992, 1966.
- [22] S. Ciliberto and C. Laroche. Experimental evidence of self organized criticality in the stick-slip dynamics of two rough elastic surfaces. *Journal de Physique I*, 4:223–235, Feb 1994.



- [23] F. Zypman, J. Ferrante, M. Jansen, K. Scanlon, and P. Abel. Evidence of self-organized criticality in dry sliding friction. *Journal of Physics: Condensed Matter*, 15(12):L191, 2003.
- [24] G. Ananthakrishna and J. Kumar. Correlation between stick-slip frictional sliding and charge transfer. *Phys. Rev. B*, 82:075414, Aug 2010.
- [25] T. Zhang, H. Wang, and Y. Hu. Atomic stick-slip friction between commensurate self-assembled monolayers. *Tribology Letters*, 14(2):69–76, 2003.
- [26] C. Voisin, F. Renard, and J.-R. Grasso. Long term friction: From stick-slip to stable sliding. 34:13301, Jul 2007.
- [27] P. Bak, C. Tang, and K. Wiesenfeld. Self-organized criticality: An explanation of the  $1/f$  noise. *Phys. Rev. Lett.*, 59:381–384, Jul 1987.
- [28] D. Lee, X. Banquy, and J. Israelachvili. Stick-slip friction and wear of articular joints. *Proceedings of the National Academy of Sciences*, 110(7):E567–E574, 2013.
- [29] M. Feldmann, D. Dietzel, H. Fuchs, and A. Schirmeisen. Influence of contact aging on nanoparticle friction kinetics. *Phys. Rev. Lett.*, 112:155503, Apr 2014.
- [30] S. Nielsen, J. Taddeucci, and S. Vinciguerra. Experimental observation of stick-slip instability fronts. *Geophysical Journal International*, 180(2):697–702, 2010.
- [31] S. Rubinstein, G. Cohen, and J. Fineberg. Detachment fronts and the onset of dynamic friction. *Nature*, 430(7003):1005–1009, Aug 2004.
- [32] S. M. Rubinstein, G. Cohen, and J. Fineberg. Visualizing stick-slip: experimental observations of processes governing the nucleation of frictional sliding. *Journal of Physics D: Applied Physics*, 42:214016, 2009.
- [33] J. Dieterich and B. Kilgore. Direct observation of frictional contacts: New insights for state-dependent properties. *Pure Appl. Geophys*, pages 283–302, 1994.
- [34] Q. Li, Y. Dong, D. Perez, A. Martini, and R. Carpick. Speed dependence of atomic stick-slip friction in optimally matched experiments and molecular dynamics simulations. *Phys. Rev. Lett.*, 106:126101, Mar 2011.

- [35] A. Socoliuc, R. Bennewitz, E. Gnecco, and E. Meyer. Transition from stick-slip to continuous sliding in atomic friction: Entering a new regime of ultralow friction. *Phys. Rev. Lett.*, 92:134301, Apr 2004.
- [36] O. Braun and Y. Kivshar. *The Frenkel-Kontorova model: concepts, methods, and applications*. Springer, 2004.
- [37] A. Vanossi and O. Braun. Driven dynamics of simplified tribological models. *Journal of Physics: Condensed Matter*, 19(30):305017, 2007.
- [38] D. Cule and T. Hwa. Tribology of sliding elastic media. *Phys. Rev. Lett.*, 77:278–281, Jul 1996.
- [39] F. Lacombe, S. Zapperi, and H. Herrmann. Force fluctuation in a driven elastic chain. *Phys. Rev. B*, 63:104104, Feb 2001.
- [40] M. Weiss and F. Elmer. Dry friction in the frenkel-kontorova-tomlinson model: dynamical properties. *Zeitschrift für Physik B Condensed Matter*, 104(1):55–69, 1997.
- [41] G. Kuenning. Mersenne twist prng.
- [42] Tino Kluge. c++ cubic spline interpolation.
- [43] M. Weiss and F. Elmer. Dry friction in the frenkel-kontorova-tomlinson model: Static properties. *Phys. Rev. B*, 53:7539–7549, Mar 1996.
- [44] R. Lakes. *Viscoelastic Materials*. Cambridge University Press, 2009. Cambridge Books Online.
- [45] G. Haugstad, J. Hammerschmidt, and W. Gladfelter. Viscoelasticity in nanoscale friction on thin polymer films, 2000 2000.
- [46] E. Jagla, F. Landes, and A. Rosso. Viscoelastic effects in avalanche dynamics: A key to earthquake statistics. *Phys. Rev. Lett.*, 112:174301, Apr 2014.
- [47] A. Taloni, A. Benassi, S. Sandfeld, and S. Zapperi. Scalar model for frictional precursors dynamics. *Sci. Rep.*, 5:–, Feb 2015.
- [48] Y. Bar-Sinai, R. Spatschek, E. A. Brener, and E. Bouchbinder. On the velocity-strengthening behavior of dry friction. *Journal of Geophysical Research (Solid Earth)*, 119:1738–1748, Mar 2014.

- [49] L. Amaral, A. Barabasi, H. Makse, and H. Stanley. Scaling properties of driven interfaces in disordered media. *Phys. Rev. E*, 52:4087–4104, Oct 1995.
- [50] A. Rosso, A. Hartmann, and W. Krauth. Depinning of elastic manifolds. *Phys. Rev. E*, 67:021602, Feb 2003.
- [51] H. Leschhorn, T. Nattermann, S. Stepanow, and L.-H. Tang. Driven interface depinning in a disordered medium. *Annalen der Physik*, 509:1–34, 1997.
- [52] M. Paczuski, S. Maslov, and P. Bak. Avalanche dynamics in evolution, growth, and depinning models. *Phys. Rev. E*, 53:414–443, Jan 1996.
- [53] S. Buldyrev, J. Ferrante, and F. Zypman. Dry friction avalanches: Experiment and theory. *Phys. Rev. E*, 74:066110, Dec 2006.
- [54] O. M. Braun, A. R. Bishop, and J. Röder. Hysteresis in the underdamped driven frenkel-kontorova model. *Phys. Rev. Lett.*, 79:3692–3695, Nov 1997.
- [55] S. Papanikolaou, D. Dimiduk, W. Choi, J. Sethna, M. Uchic, C. Woodward, and S. Zapperi. Quasi-periodic events in crystal plasticity and the self-organized avalanche oscillator. *Nature*, 490(7421):517–521, Oct 2012.
- [56] M. Bretz, R. Zaretzki, S. Field, N. Mitarai, and F. Nori. Broad distribution of stick-slip events in slowly sheared granular media: Table-top production of a gutenbergrichter-like distribution. *EPL (Europhysics Letters)*, 74(6):1116, 2006.
- [57] F. Dalton and D. Corcoran. Self-organized criticality in a sheared granular stick-slip system. *Phys. Rev. E*, 63:061312, May 2001.
- [58] J. Feder, H. Nordhagen, and W. A. Watters. Dynamic scaling in stick-slip friction. *eprint arXiv:nlin/0504034*, Apr 2005.

## Appendix A

# Driving and slip characterization

As introduced in Chapter 3, the slips can be determined in two ways: looking at the change in the derivative of the friction force (from positive to negative indicates the beginning of a slip, and from negative to positive correspondingly indicates a stop), or with a velocity threshold (a particle crossing the threshold indicates the start of a slip, and all particles dropping below the threshold indicates the stop). If the driving is paused while slipping with a low relaxation threshold, the results obtained with either slip characterization method are essentially the same. Discrepancies between the methods show up when the chain is driven continuously, or when the relaxation threshold is large. The behaviour is similar in parallelly and perpendicularly driven chains and doesn't change qualitatively with the inclusion of viscoelasticity and contact aging, and thus only the perpendicular case without the extension is documented here.

In practice, the force derivative method keeps track of the change in the total friction force between steps. Thus the slips are indicated by the average velocity of the chain growing larger than the driving velocity:

$$\begin{aligned}\Delta F &= F(t + \Delta t) - F(t) \\ &= k_0 \sum_{i=0}^N \left( [V \cdot (t + \Delta t) - x_i(t + \Delta t) + x_{i0}] - [Vt - x_i(t) + x_{i0}] \right) \\ &= k_0 \sum_{i=0}^N \left( V\Delta t - x_i(t + \Delta t) + x_i(t) \right) \\ &= k_0 \sum_{i=0}^N (V\Delta t - v_i\Delta t) = k_0\Delta t \left( NV - \sum_{i=0}^N v_i \right).\end{aligned}$$

Since a particle that does not slip has  $v_i \approx 0$ , we can sum only over the slipping particles:

$$\begin{aligned}\Delta F &= k_0 \Delta t (NV - \sum_{i \in \{I_s\}} v_i) = k_0 \Delta t (NV - N_s \bar{v}_s) \\ &= k_0 \Delta t N (V - \frac{N_s}{N} \bar{v}_s),\end{aligned}$$

where  $N_s$  is the amount of slipping particles, and  $\bar{v}_s$  is their average velocity. Since  $k_0$ ,  $\Delta t$  and  $N$  are all positive, the term  $V - \frac{N_s}{N} \bar{v}_s$  determines whether the change is positive or negative and thus whether the system is slipping or pinned.

Determining slips this way, their "visibility" depends on the system size and the driving velocity. If only a small amount of particles slip and the driving is not paused while slipping, the decrease in friction force is somewhat mitigated by the increase of driving force of the other particles. This can lead to an increase in the amount of small slips relative to large ones. Using very low driving speeds or pausing the driving when slipping helps with this problem. However, low speeds extend the simulation time, and when pausing is used, the relaxation velocity threshold has an effect on the statistics. Fig. 74 shows how the size distribution behaves with a couple of different velocities and relaxation velocity thresholds. Pausing the driving while the system slips with a low threshold seems to give the longest straight power law portion in the distribution, but the exponents  $\tau_S \approx 0.85 - 0.95$  are a tad lower than those found in literature. Further lowering either driving velocity or relaxation velocity threshold had little effect on the distribution.

An additional problem with the slip characterization based on the friction force derivative is that when examining viscoelastic effects in the model, the viscoelastic relaxation may cause some particles to move backwards, increasing the friction force and hence skewing the avalanche distributions.

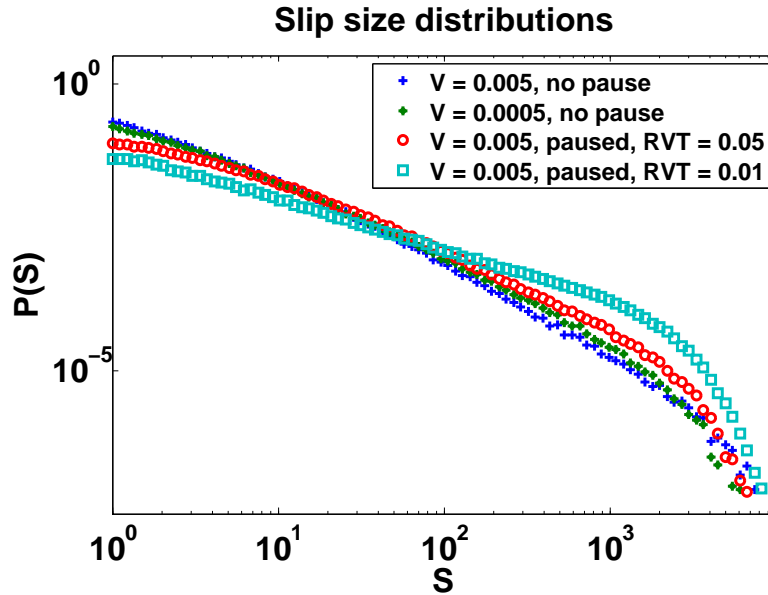


Figure 74: The slip size distributions of 1000 particles, with slips characterized via the force derivative. RVT stands for relaxation velocity threshold. When the driving is not paused while slipping, the avalanche size exponent  $\tau_S$  can get be high as 1.3 (blue + signs), whereas low relaxation threshold can yield size exponents as low as 0.85 (cyan squares).

When using the velocity threshold characterization of avalanches, the velocity of an individual particle has more impact than in the force derivative method, and thus slips with fewer particles are more easily detected than in the force derivative method. However, the value of the relaxation velocity threshold greatly affects results, especially when the driving is not paused when the system slips: with a high threshold, very few slips are registered, and they have a tendency to be small. This happens mostly because the particles experiencing a slip quickly fall below the threshold if the threshold is large. By contrast, with a very low relaxation threshold, the chain never slows down enough for any slips to be registered, or multiple slips can be registered as one (as was shown in Chapter 4, Fig. 12). Pausing the driving in this case would also intuitively seem preferable, since it reduces the amount of concurrent slips happening. Still, the change in the avalanche critical exponents raises some doubts about the method's validity.

## Appendix B

### Finite-size effects

All the distributions in this thesis were acquired from simulations where the systems were large compared to the correlation length, and only parts of the system slipped at a time. Another interesting aspect of simulations with finite chains is to see how the behaviour changes when the correlation length becomes equal to or exceeds the system length, necessitating system-wide slips. This was achieved by making the system smaller by decreasing the amount of particles and having a small driving spring stiffness, mainly  $k_0 = 0.001$ . The values used for the simulations are collected in Table B.1. The effects were tested with chain lengths of 10, 50 and 100 particles. For the parallelly driven chain, the systems were tested for both sparse and dense chains.

Since the systems consisted of relatively few particles and the idea was to make most or all of them slip at once, the probability of simultaneous avalanches was small, and therefore it was not necessary to stop the driving when an avalanche occurred. To be sure, a lower driving velocity was used.

Table B.1: The control parameter values for the simulations concerning finite-size effects.

Control parameter	Value
Number of particles $N$	10, 50, 100
Driving velocity $V$	0.0005
Driving spring constant $k_0$	0.1 - 0.001
Particle equilibrium distance $d$	1, 20
Pause driving while slipping	false
Slip characterization method	force derivative

### B.0.1 Parallel driving

When the amount of particles taking part in a slip is large relative to the number of particles in the chain and the particles slip for long distances, greater portions of the chain explore new potential surface and the chain does not necessarily slip into the same configuration shifted by the equilibrium distance, as was typically the case with simulations of the parallel chain without finite-size effects. Due to the long distance traveled and new potential explored, the motion becomes nonperiodic and chaotic even in the steady state. Due to most of the particles slipping at once, the friction force acts more like in macroscopic friction experiments, with sawtooth-like fluctuations (Fig. 75). The precursory avalanches are more noticeable in the dense chain.

The avalanche statistics of the chain are also considerably different when compared to simulations with longer and more pliant chains. When the equilibrium distance is large (sparse chain) the slips up to the chain length seem to be power law distributed, with somewhat lower exponents ( $\tau_S \approx 0.82$ ), and there's a sharp increase in probability at the chain length. By contrast, with a small equilibrium distance and having fewer particles and thus overall short chain, the slips that are larger than the total length of the chain appear to be power law distributed, and the critical exponent of the size distribution is similar to the ones found for longer perpendicular and parallel chains. Interestingly, there's a smaller "cut-off" at the system size, after which the power law part starts. The other cut-off at the end of the distribution seems a bit less steep, possibly even a power law.



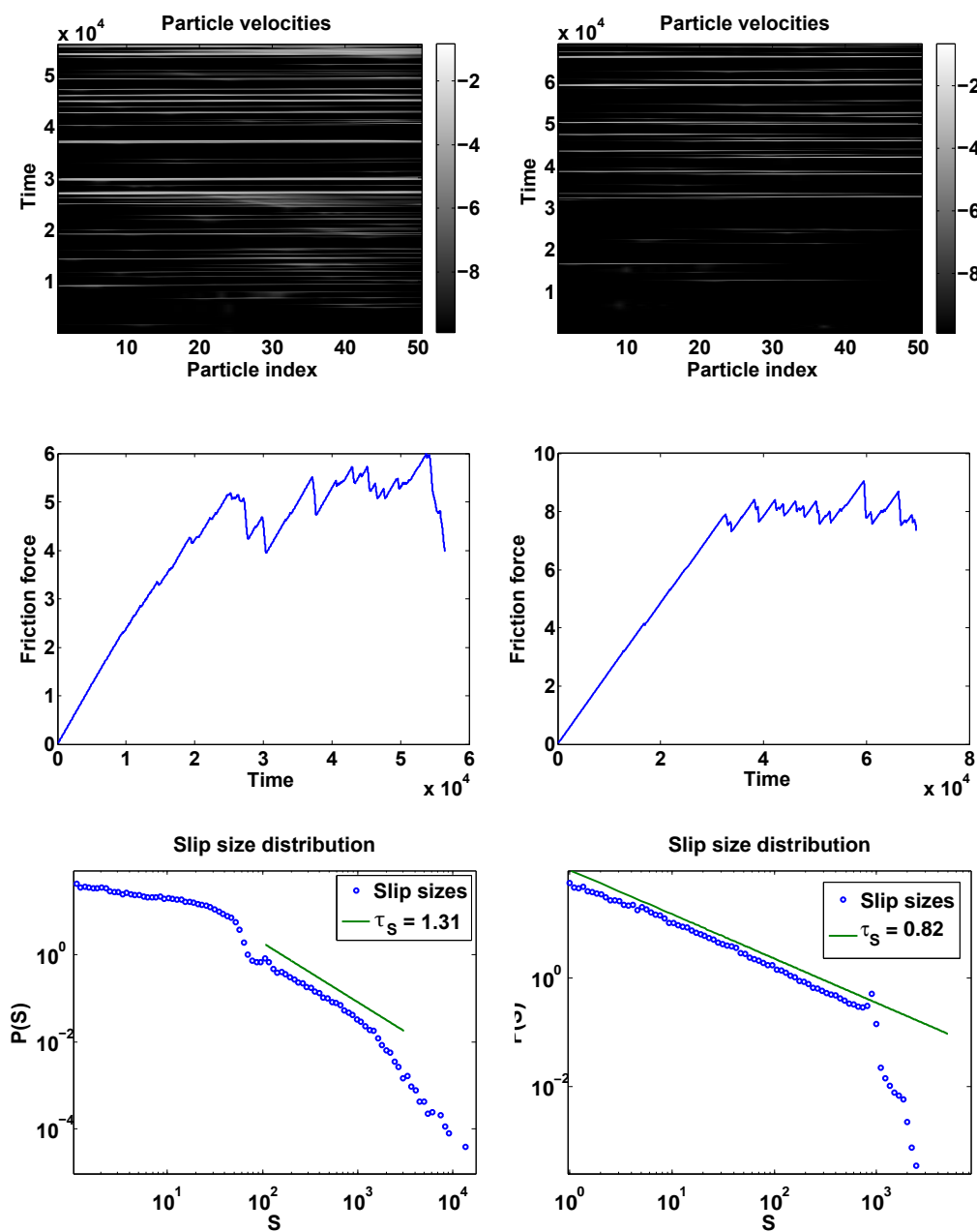


Figure 75: The onset of motion velocities (top) and friction force drops (middle) show system-wide slips occurring in parallelly driven 50-particle dense (left) and sparse (right) chains with driving spring stiffness of  $k_0 = 0.001$ . Both size distributions (bottom) seem to exhibit a power law.

The avalanche distributions with short parallel driving showed in general interesting, though somewhat logical, behaviour: with 10 particles and equilibrium distance 1, there's a bump in the size distribution at the multiples of 10 (Fig. 76), indicating that each particle jumps 1,2,3 etc. units of distance forward, i.e. approximately to the location occupied by its 1st, 2nd, 3rd neighbor, respectively. The effect diminishes quite fast, however; at 40, the bump is barely noticeable.

The behaviour can be explained by considering the length of the chain and boundary effects: the chain is relaxed at a local potential minimum, and when it is driven to an avalanche, it relocates to the next local minimum. When the equilibrium distance is small, the nearest a local minimum is likely a similar configuration the chain is in at the start of the slip, shifted by one or more equilibrium distances forward, depending on how far the driving slab has moved before a slip is initiated. For a single particle, this means that the locations of the neighboring particles tend to be attractive places for relocation.

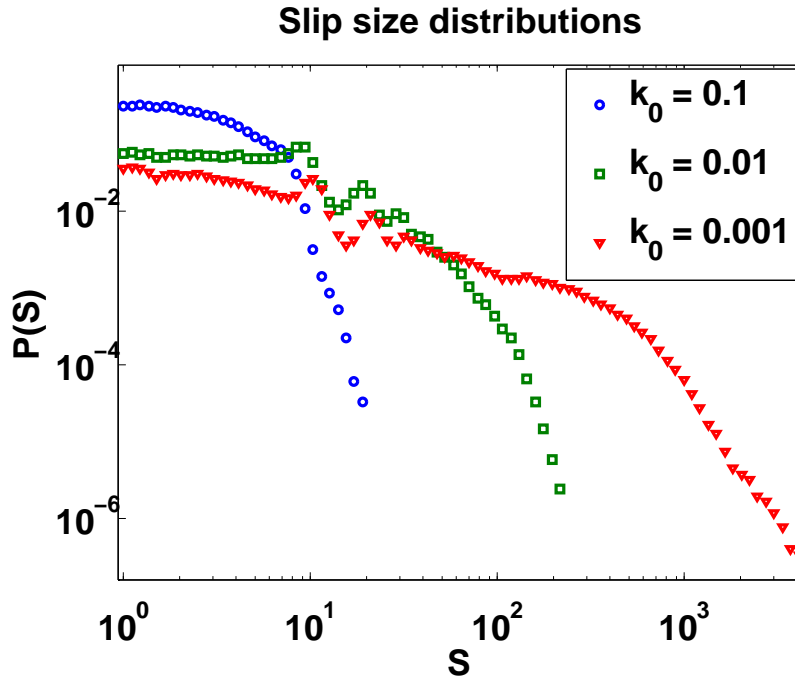


Figure 76: The slip sizes for parallelly driven chain of 10 particles with equilibrium distance 1 (total length 10). Having a driving spring stiffness of 0.1 has cut-off value smaller than the system, so the discrete bump does not appear.

At the boundary, however, the particles experience new potential. The more the chain slips, the more particles explore the unfamiliar potential, possibly resulting in an overall different configuration. Thus the particles don't necessarily move to the locations previously occupied by their neighbors, "blurring out" the slip sizes at higher multiples of the chain length.

With particle equilibrium distance  $d = 20$ , the total length of the system is 200. Taking the length into account, the system behaves similarly to the one with smaller equilibrium distance: there's a bump in the system-length slips (i.e. 200, 400 etc.), though large value for  $k_0$  induces a cut-off smaller than the system size, so the bumps might not be visible. Interesting notion is that even though there are only 10 particles, there are only very slight bumps at 10, 20, 30 etc. in the longer system (Fig. 77).

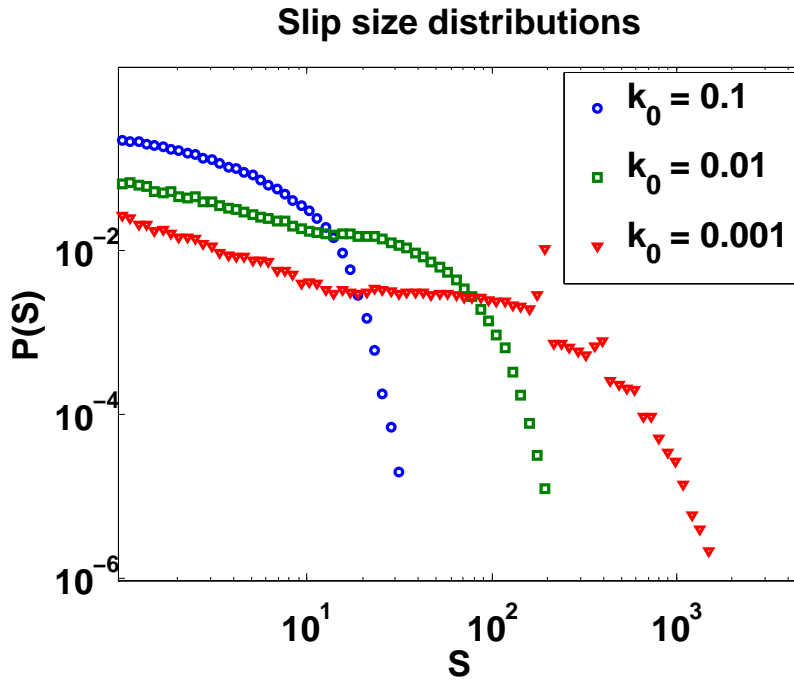


Figure 77: The slip sizes for parallelly driven chain of 10 particles with equilibrium distances 20 (total length 200).

The reason for this is probably the fact that larger distance between particles means more potential wells and thus more potential minima before arriving to the location of the neighboring particle. Since the wells are randomly distributed in space, the slip sizes do not display any preference, provided that the slips are relatively small. However, if the particles end up in a particularly deep potential minimum, the driving slab can advance far before

initiating a new avalanche. Once the avalanche finally occurs, the particles must slip far in order to relax the driving springs. In this case, the particles are likely to cross over small local minima and end up in another deep potential minimum, which again is typically the similar configuration from which the slip started (excluding boundary particles). This explains the probability spikes that appear at 200, 400 etc.

Curiously, 50 particles with equilibrium distance 1 do not display a similar bump in the size distribution at the total chain length. Instead, there's a rather large drop in the probability, but a slight bump at 100 as seen in Fig. 78. Similarly, a chain of 100 particles and  $d = 1$  has a probability drop instead of increase at 100 (Fig. 79). Both 50- and 100-particle chains show a little bit of power law reminiscent behaviour after the drop in the  $d = 1$  case.

In the case of  $d = 20$ , the 50-particle and 100-particle chains have similar avalanche distributions: power law distributed sizes up to the total chain length, a probability spike at roughly the total length (though in the 100-particle chain, the cut-off obscures the bump at 2000), then decline and finally cut-off.

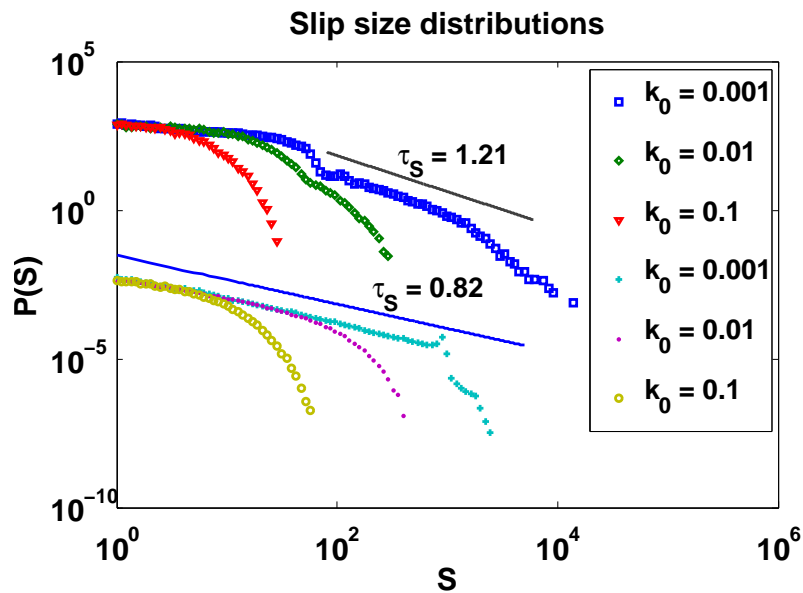


Figure 78: The slip size distributions for a parallelly driven, 50 particle chain with equilibrium distances 1 (top three distributions) and 20 (bottom 3 distributions). With a long but sparse chain, there seems to be a power law distribution of slip sizes up to the chain length. The distributions are scaled so that they do not overlap.

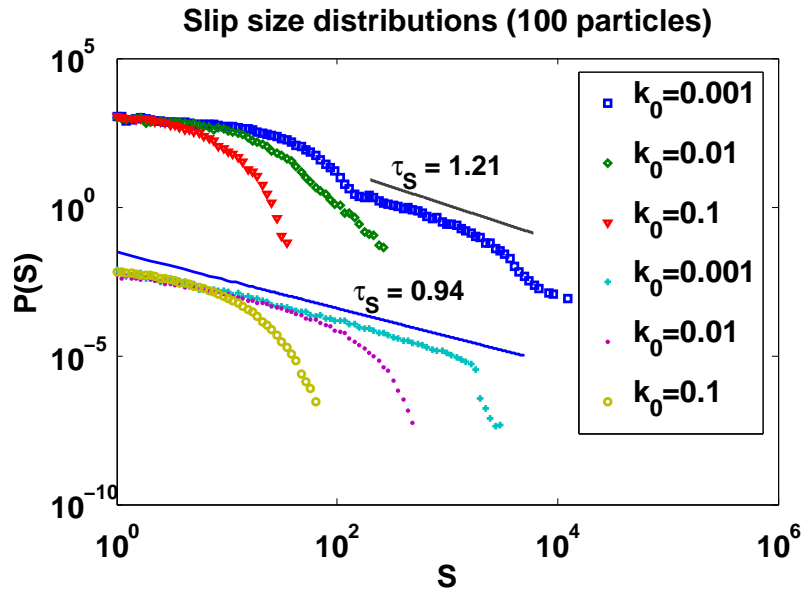


Figure 79: The slip size distributions for a parallelly driven, 100 particle chain with equilibrium distances  $d = 1$  (top three distributions) and  $d = 20$  (bottom 3 distributions). The behaviour is very similar to the 50-particle chain, though the exponent  $\tau_S$  is larger in the  $d = 20$  case.

The rigidity of the chain (strength of the interparticle interaction) influences the collective movement. If the interparticle interactions are relatively strong (short chain or large  $k_1$ ), the chain has a tendency to move in rigid jumps. This can be seen when increasing the interparticle spring stiffness to  $k_1 = 5$  in the particle chain of 50 particles: the slips start showing an increased probability at 50 and its multiples (Fig. 80 left), similarly to the 10-particle chain did with the multiples of 10. With weaker interparticle interactions, the probability for chain-wide slips decreases, since parts of the system can slip individually, though there's still possibility for slips larger than the system size (Fig. 80 right).

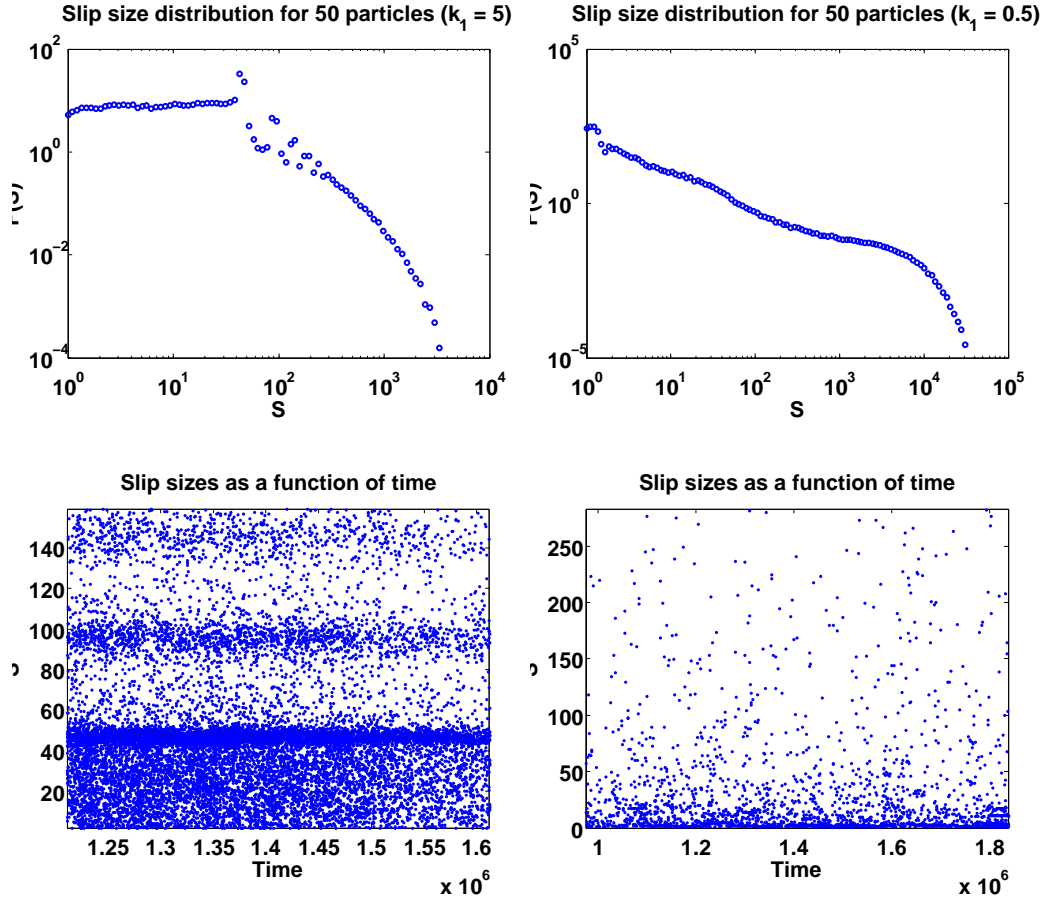


Figure 80: When the interparticle interaction is strong (left), the particles of the parallel chain like to make discrete jumps, causing peaks in the distribution at the multiples of the chain length. The effect is more easily seen from the time-size slip profile of the chain (bottom left).

To study the possible power law in the slips larger than the system, a simulation was run with 100 particles, equilibrium distance 1 and a driving spring stiffnesses  $k_0 = 0.001$  and  $k_0 = 0.0001$ . The obtained distributions are presented in Fig. 81, and the results would indeed seem to indicate a power law distribution. The exponent is comparable to the critical exponent of the previous simulations, though the cut-off is only barely visible.

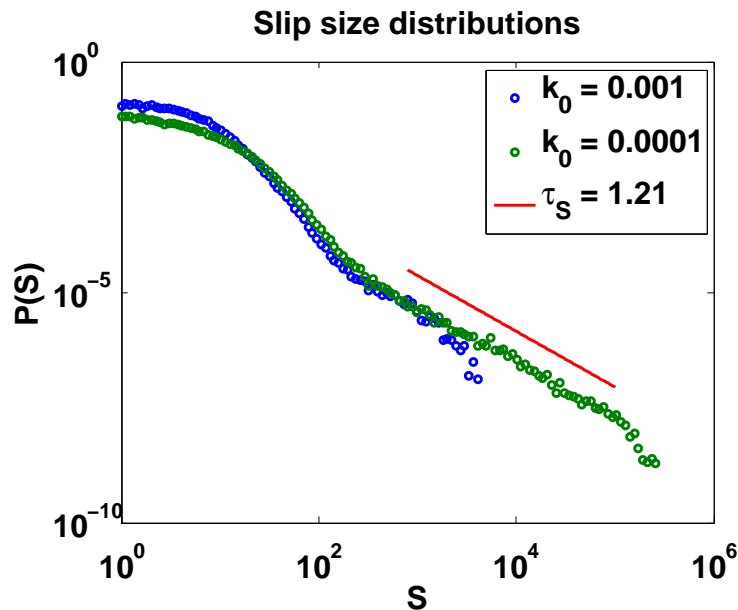


Figure 81: The slips that are larger than the system size have a power law distribution with exponent  $\tau_S = 1.21$  in the parallelly driven chain.

## B.0.2 Perpendicular driving

In the perpendicular driving case, having a small system and large correlation length had surprisingly little effect. Only with 10 particles there's some noticeable drop in the probability of system-wide avalanches similar to the parallel driving case, but the larger slips didn't seem to have a well defined power law distribution (Fig. 82). 50 particles displayed a slight bump in the distribution in the larger slips, but otherwise there were no changes (Fig. 83). It was noticed that power laws similar to the ones obtained from simulations with 1000 particles could be obtained with just 100 particles, though the distributions are a bit more curved (Fig. 84). This would seem to imply that the correlation length is the same order of magnitude as the chain length in these simulations when  $k_0 = 0.001$ , and indeed it was noticed with the larger chain that the correlation length was roughly 200-300.

The perpendicular chain is different when compared to parallelly driven chain likely because each particle in the perpendicular chain has its own unique potential surface. Since each particle constantly explores new potential, there are no preferred slipping locations like there were in the parallel chain, and hence no probability spikes either. When the chain is made more rigid by increasing the strength of the interparticle interactions, the likelihood of small slips decreases. With 10 particles, the drop is visible already

with  $k_1 = 1$ . Similar effect can be achieved with larger chains by increasing  $k_1$ , as demonstrated in Fig. 85.

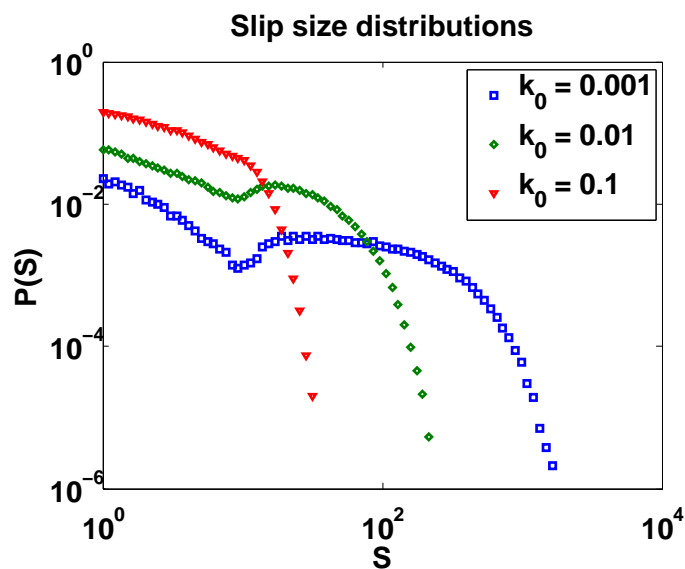


Figure 82: A perpendicular chain of 10 particles displays a probability drop at system-wide slips.

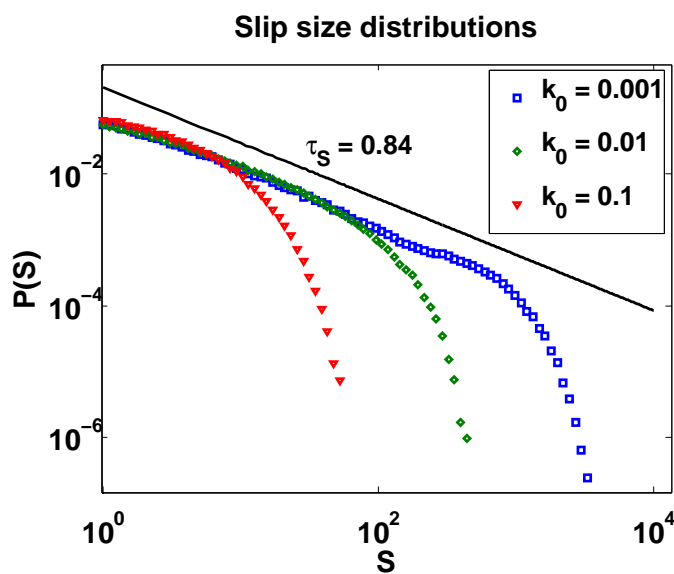


Figure 83: A 50-particle long chain has a quite nice linear part, though the distributions are curved slightly and the critical exponent is small. There's a slight bump in the distribution for larger slips.



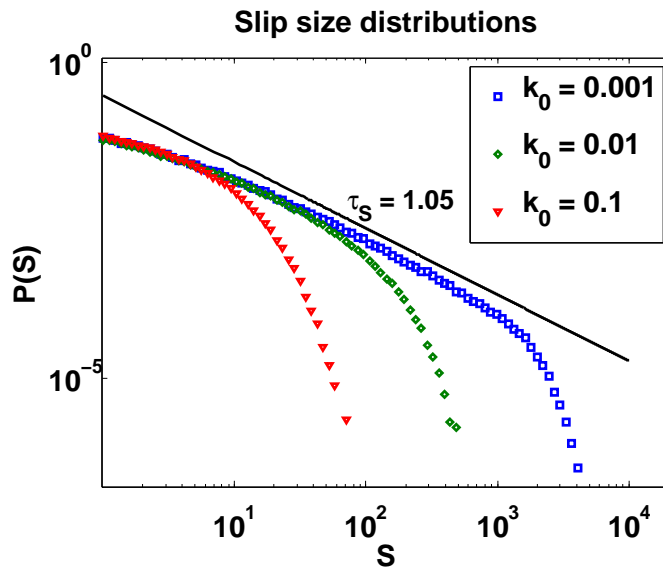


Figure 84: The avalanche size exponent of a 100-particle chain is close to the exponent obtained with significantly larger number of particles, though the linear part is questionable since the distribution is quite curved. Especially with  $k_0 = 0.1$  and  $k_0 = 0.01$  the exponent  $\tau_S$  is closer to  $0.7 - 0.8$ .

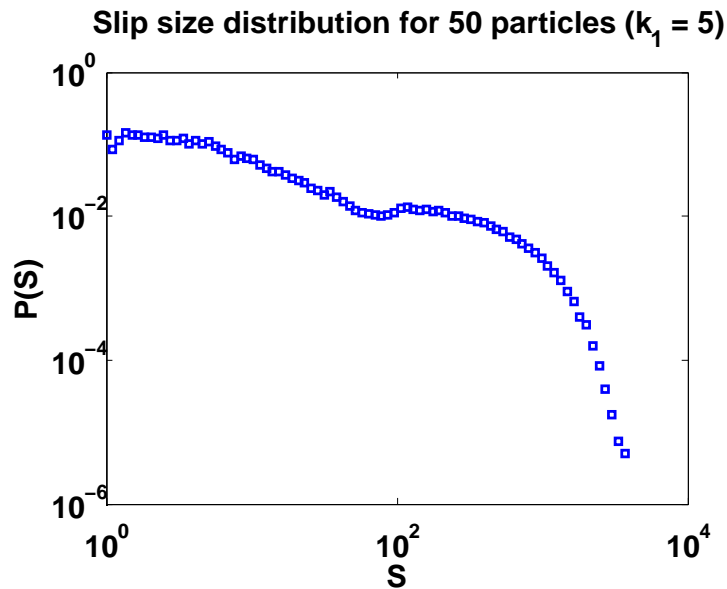


Figure 85: A perpendicular chain of 50 particles displays a drop in slip sizes at 50 when the nearest neighbor interaction is strong enough.